EXPERIMENTAL INVESTIGATION INTO WIRE ARC ADDITIVE MANUFACTURING OF ALUMINIUM 5356 ALLOY PART AND IT'S POST PROCESSING BY LASER NITRIDING

M.Tech Thesis

By

SAYAN DOLOI

Roll No.: 2202103002

DEPARTMENT OF MECHANICAL ENGINEERING

INDIAN INSTITUTE OF TECHNOLOGY INDORE

May 2024

EXPERIMENTAL INVESTIGATION INTO WIRE ARC ADDITIVE MANUFACTURING OF ALUMINIUM 5356 ALLOY PART AND IT'S POST PROCESSING BY LASER NITRIDING

A THESIS

Submitted in partial fulfilment of the requirements for the award of the degree
of
Master of Technology

by

SAYAN DOLOI
Roll No.: 2202103002

DISCIPLINE OF MECHANICAL ENGINEERING

INDIAN INSTITUTE OF TECHNOLOGY INDORE

May 2024

Indian Institute of Technology Indore

CANDIDATE'S DECLARATION

I hereby certify that the work being presented in the thesis titled "**EXPERIMENTAL INVESTIGATION INTO WIRE ARC ADDITIVE MANUFACTURING OF ALUMINIUM 5356 ALLOY PART AND IT'S POST PROCESSING BY LASER NITRIDING"** in the partial fulfilments of the requirements for the award of the degree of **M.TECH** and submitted in the **Discipline of Mechanical Engineering, Indian Institute of Technology, Indore** is an authentic record of my own work performed during the time period of July, 2022 to May, 2024 under the supervision of Dr. I.A Palani, Professor, Department of Mechanical Engineering, Indian Institute of Technology, Indore and Dr. Jayaprakash Murugesan, Associate Professor, Department of Metallurgical Engineering and Materials Science, Indian Institute of Technology, Indore.

The matter presented in the thesis has not been submitted by me for the award of any other degree of this or any other institute.

Sayan Doloi.

Signature of the student

(Sayan Doloi) 4/6/24

This is to certify that the above statement made by the candidate is correct to the best of our knowledge.

Signature of the Supervisors of M.Tech thesis :

	M-Jayaprakash 04/06/2024
Signature of the Supervisor of M.Tech. thesis #1 **(Prof. I. A. Palani)**	Signature of the Supervisor of M.Tech. thesis #2 **(Prof. Jayaprakash Murugesan)**

Sayan Doloi has successfully given his M.Tech Oral Examination held on 03.06.2024.

Signatures of Supervisors of M.Tech. thesis :

	M-Jayaprakash 04/06/2024
Prof. I. A. Palani	**Prof. Jayaprakash Murugesan**

DATE : 04.06.2024

4/6/24

Signature of Convener, DPGC

ACKNOWLEDGEMENTS

First of all, I want to convey my sincere gratitude to my supervisors, Dr. I.A Palani, Professor, Department of Mechanical Engineering, Indian Institute of Technology, Indore and Dr. Jayaprakash Murugesan, Associate Professor, Department of Metallurgical Engineering and Materials Science, Indian Institute of Technology, Indore for providing me with the opportunity to work on this M.Tech Thesis work under their esteemed supervision.

I sincerely thank our Director Sir, Prof. Suhas S. Joshi for his encouragement during M.Tech. classes and thesis work. I also wholeheartedly thank our HOD Sir and coarse co-ordinator of M. Tech program for their valuable supports in every stage of my thesis work. I also thank all the faculty members, specially DPGC convener and PSPC members for their fruitful technical interactions during the progress of my M. Tech. thesis work.

I am deeply indebted to all the research scholars of our laboratory specially Dr. Anshu Sahu and Mr. Arpit Kumar Singh whose guidance and mentorship have been pivotal in my learning journey. Their insightful feedback and unwavering support have been instrumental in helping me throughout this M. Tech Thesis work. Further, I would like to extend my gratitude to other group members and staff members of other laboratories for the supportive environment and valuable suggestions.

I would like to express my heartfelt gratitude to my friends, Souptik Pandit and Partha Pratim Das, for their unwavering support and insightful discussions throughout this journey.

Finally, I am eternally grateful to my family for their continuous encouragement, and moral support.

Sayan Doloi

DEDICATED TO MY BELOVED PARENTS

Abstract

Aluminium alloys find wide-ranging applications in the different industries due to their lightweight nature, high specific strength, excellent corrosion resistance, good damping capacity, high machinability, and good strength-to-weight ratio. Wire-arc additive manufacturing (WAAM) is well-suited process for application in a variety of sectors since it can produce big, reasonably complicated parts at minimal investment, operating expenses and high deposition speed and efficiency. Different process parameters like stand off distance, feed, voltage, and cooling time play a vital role in controlling the quality of WAAM deposited parts. However, the additively manufactured component requires different post processing techniques to enhance the mechanical and tribological properties. The present study deals with the parametric optimization of process variables of WAAM for fabricating parts of aluminium 5356 alloy based on mathematical modelling using experimental data as per Box Behnken design of experiments. Moreover, the single and multi- objective optimization of the responses were also performed using desirability function analysis to obtain an optimal set of process variables. On the optimal parametric setting, aluminium alloy walls were deposited and different mechanical testing like tensile testing and micro-hardness testing are performed on it. The additively manufactured samples at optimal parametric setting are treated with selective area nitriding to reduce the coefficient of friction, wear volume and also to enhance the micro-hardness. The impact of laser nitriding process parameters such as laser intensity, scanning speed, and N_2 gas flow, on the surface hardness, contact angle and tribological properties of wire-arc additively manufactured Al alloy part has been investigated. The laser nitriding significantly improved the surface hardness and reduced the coefficient of friction and wear volume. The laser interaction resulted in a change of the surface from hydrophilic to hydrophobic which helps to reduce the bio-fouling and maintaining the smooth operation of the marine components.

TABLE OF CONTENTS

LIST OF FIGURES

LIST OF TABLES

Chapter 1

Introduction

1.1 Introduction to Additive Manufacturing

Additive manufacturing has transformed manufacturing by providing a more flexible, cost-efficient, and streamlined alternative to traditional subtractive method [1]. Rather than starting with a solid block of material and cutting away excess, additive manufacturing constructs objects layer by layer from digital 3D models. This process offers greater design freedom and complexity, reducing material waste and enabling the use of a wide variety of materials, including metals, composites, plastics, ceramics, and biomaterials [2]. In industrial sectors, additive manufacturing is utilized for rapid prototyping, tooling and fixture production, and low-volume manufacturing, accelerating product development and innovation across different industries like aerospace, automotive, healthcare, and consumer goods. As technology develops, additive manufacturing is improving production, encouraging creativity in design and production processes, and influencing the future of manufacturing and supply chains.

1.1.1 Types of Additive manufacturing

Because AM process is so broad, it can be categorised in a wide range of situations. The broad categorization of AM processes from various angles is shown in Fig. 1.1. Seven primary categories of additive manufacturing (AM) processes can be used to classify the more than fifty different additive manufacturing technologies, according to ASTM F2792-12a [3], [4]. Three categories can be applied to these processes: (i) AM based on binder, such as material extrusion (ME) and binder jetting (BJ); (ii) AM based on high energy heat source, such as sheet lamination, powder bed fusion (PBF), and direct energy deposition (DED); and (iii) AM based on liquid, such as material jetting and vat photopolymerization.

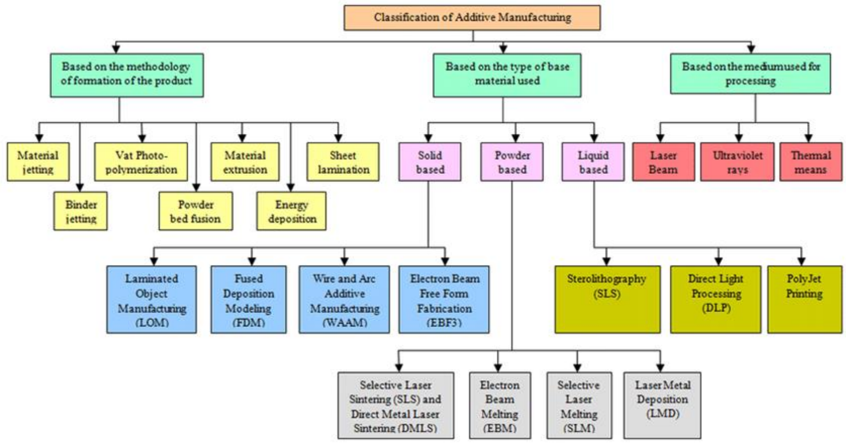

Fig. 1.1: Classification of Additive Manufacturing Processes [4]

Vat polymerization involves immersing a reservoir of photopolymer resin, from which the desired object is manufactured in layer-by-layer fashion. Material jetting functions similarly to conventional inkjet printer but in three dimensions. In material jetting, the material is propelled onto a build platform using either a continuous method or Drop on Demand method. In binder jetting, a powdered substance and a binding agent, typically in liquid form are utilized. The powdered material and the binding agent are deposited in alternating layers by a print head that moves horizontally along the machine's x and y axes. Fused deposition modeling (FDM), a widely-used material extrusion technique trademarked by Stratasys, operates by feeding material through a nozzle, heating it, and depositing it layer by layer fashion. After every new layer is applied, a platform moves vertically and the nozzle moves horizontally. Direct Metal Laser Sintering (DMLS), Electron Beam Melting (EBM), Selective Heat Sintering (SHS), Selective Laser Melting (SLM), and Selective Laser Sintering (SLS) are among the printing techniques that are included in Powder Bed Fusion. Sheet lamination techniques such as Ultrasonic Additive Manufacturing (UAM) and Laminated Object Manufacturing (LOM) employ metal sheets or ribbons bonded together via ultrasonic welding. Directed Energy Deposition (DED) comprises multiple terms including 'Laser Engineered Net Shaping,' 'Directed Light Fabrication,' 'Direct Metal

Deposition,' and '3D Laser Cladding.' It's a printing process commonly used for repairing or adding material to existing components. However apart from these conventional additive manufacturing techniques there can be different hybrid additive manufacturing techniques combining two or more additive manufacturing processes as well as combining additive manufacturing process with conventional machining [5].

1.1.2 Wire Arc Additive Manufacturing (WAAM)

WAAM has emerged as a prominent Directed Energy Deposition (DED) technology, originating from traditional arc welding methods. In WAAM, an electric arc melts wire, which is then deposited onto a molten metal pool, gradually solidifying to form the desired part. This process is advantageous for creating large structures economically and is well-suited for repair work. WAAM encompasses three primary categories based on arc-based welding technology: Gas Tungsten Arc Welding (GTAW), Plasma Arc Welding (PAW), and Gas Metal Arc Welding (GMAW) as shown in the Fig. 1.2 (A-C). GTAW-based WAAM utilizes a non-consumable tungsten electrode to generate heat, melting a filler wire to achieve the desired part geometry [6]. PAW, employing a similar electrode, offers enhanced efficiency due to a constricted plasma arc. GMAW, widely used in WAAM, features a consumable wire electrode melting material onto the substrate, boasting superior deposition rates.

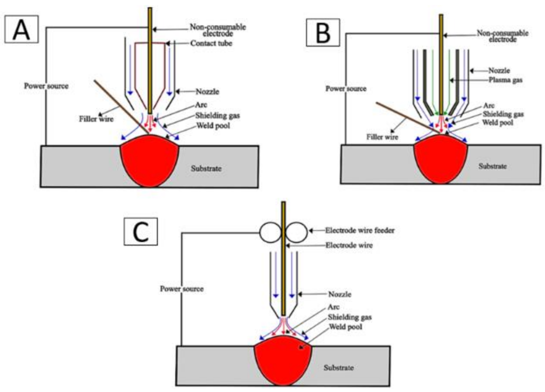

Fig. 1.2: Different Types of WAAM (A) GTAW, (B) PAW, (C) GMAW [6]

GMAW further divides into Metal Inert Gas (MIG) and Metal Active Gas (MAG), each suitable for specific metal types, with MIG primarily serving non-ferrous metals and MAG ideal for ferrous metals. GMAW operates with four metal transfer modes, each with distinct characteristics regarding welding current and electrode type. The introduction of the Cold Metal Transfer (CMT) welding process marked a significant advancement in WAAM, offering reduced heat input and spatter. CMT, based on the short-circuit transfer mode, features various modes with unique attributes. WAAM excels in manufacturing large-scale metal parts and is particularly suited for repair and maintenance operations. However, it has limitations such as residual stress, distortion, and poor surface finish. Optimization of process parameters, including feed rate and shielding gas pressure, can eliminate these issues. In the present study, detailed parametric optimization using the Box Behnken design aims to enhance output responses and reduce WAAM defects.

1.2 Different Post Processing Techniques of Additively Manufactured Parts

Additive manufacturing (AM) surfaces often lack the necessary smoothness and structural integrity for high-demand mechanical assemblies due to the layer-by-layer deposition process, resulting in rough surfaces and potential weaknesses. These flaws can compromise fatigue resistance, necessitating post-processing to enhance surface quality. Research indicates that machining significantly enhances mechanical properties like fatigue and tensile strength. Additionally, non-traditional methods such as water jet machining offer surface improvement and the unique capability to create textured surfaces, allowing for tailored properties like reduced residual stresses or enhanced hydrodynamic performance through specific tool path patterns. [5]

Laser technology finds application in various post processing methods such as laser nitriding, laser shock peening, and laser polishing. Laser polishing as shown in the Fig. 1.3, is particularly promising for refining the surface roughness of additive manufacturing (AM) components [7]. In this technique, the laser rapidly heats the material's surface, causing morphology apexes to reach melting temperature [7]. The liquid material redistributes due to gravity and surface tension, resulting in a smoother surface upon solidification as shown in the Fig. 1.4 [8]. This automated process alters surface morphology by remelting without affecting bulk properties, targeting topographical peaks created during the AM process, such as unmelted powder grains and layer overlaps. While laser polishing may induce residual stresses, secondary stress relief processes can mitigate this effect, leading to improved fatigue strength [9]. Laser shock peening (LSP) as shown in the Fig. 1.5 stands out as an advanced technique for enhancing both the mechanical and microstructural properties of additively manufactured parts [10]. A significant drawback of laser-based additive manufacturing is the presence of tensile residual stress in surface and subsurface regions. Researchers have explored laser shock peening as a post-processing technique to counteract tensile residual stress and convert it into beneficial compressive residual stress Studies on LSP applied to laser additively manufactured Ti6Al4V parts have demonstrated the creation of CRS up to 200 MPa, leading to not only a reduction in TRS but also notable microstructural refinement and increased fatigue strength [11].

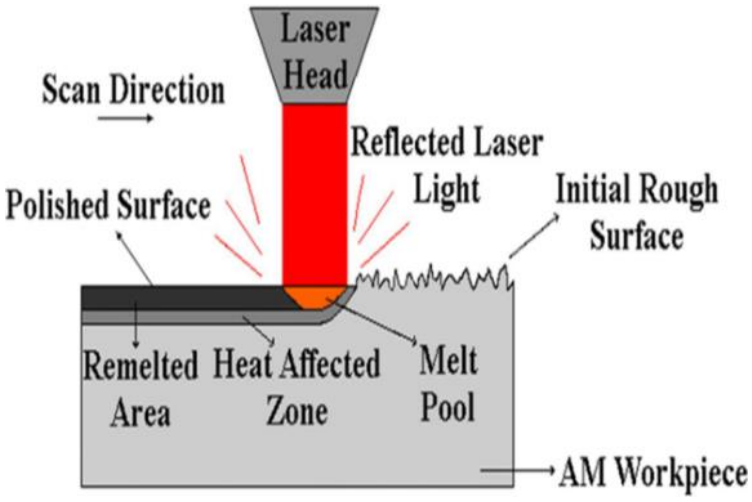

Fig. 1.3: Schematic of Laser Polishing [7]

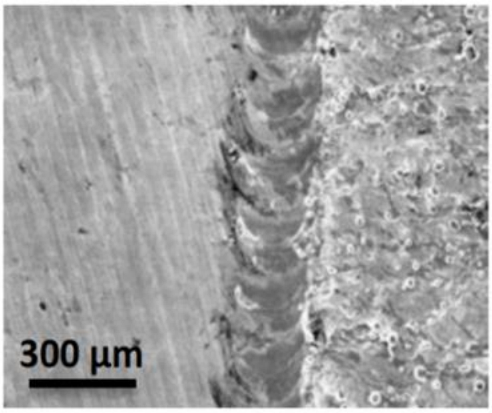

Fig. 1.4: SEM image of the material surface before (right) and after (left) laser polishing [8]

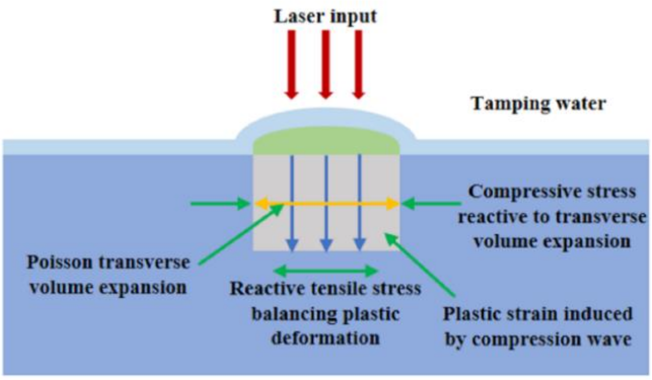

Fig. 1.5: Schematic of Laser Schock Peening [10]

Laser shock peening involves the plastic compression of material perpendicular to the surface, inducing lateral expansions and accumulating local compressive stresses in thick or constrained parts. This process alters strain and shape in thinner parts. Similar effects are achieved through other surface treatments like deep cold rolling and ultrasonic peening. Utilized extensively to enhance the fatigue life of automobile and marine components. Laser peening technology has also been employed to refine surface properties of maraging steels and shape thick sections of aircraft fenders for precise aerodynamic modelling. In laser shock peening, short intense laser pulses generate plasma, leading to pressure pulses and local plastic deformations. Accurate modelling of residual compressive stress, strain, microstructure, and component modification can be achieved, tailored to specific materials and geometries [12]. Apart from this nitriding is an emerging surface modification technique which enhances the tribological properties of the additively manufactured surface like hardness and wear resistance. The prospect of the nitriding is discussed below.

1.3 Conventional Nitriding Techniques and it's Types

Nitriding, as a post-processing technique, involves the diffusion of nitrogen into the surface of a material to enhance its mechanical and surface properties. This process is commonly used to enhance the hardness, wear resistance, and fatigue life of metal components [13]. Nitriding is typically carried out at elevated temperatures in a nitrogen-rich environment, allowing nitrogen atoms to penetrate the surface of the material and form nitrides. In additive manufacturing, nitriding can be applied as a post-processing step to further enhance the performance of additively manufactured parts. By introducing nitrogen into the surface layer of the part, nitriding can help alleviate the residual stresses and improve the surface hardness, leading to enhanced mechanical properties and durability. Nitriding being a surface hardening technique established in the early 19th century, remains pivotal in different industrial sectors such as automotive, aerospace, bearings, and turbine power generation systems. Metallurgically, nitriding is a thermochemical process where nitrogen diffuses into aluminium matrices, forming a thin, hard AlN phase on the substrate surface [14]. The Aluminium-Nitrogen binary phase diagram, depicted in Fig. 1.6, illustrates the limited solubility of nitrogen in aluminium (2 at%), leading to the formation of a secondary AlN phase when nitrogen exceeds this threshold. Temperatures ranging from 250^0c to 2550ºC facilitate this process, with aluminium vaporization occurring above this range [15].

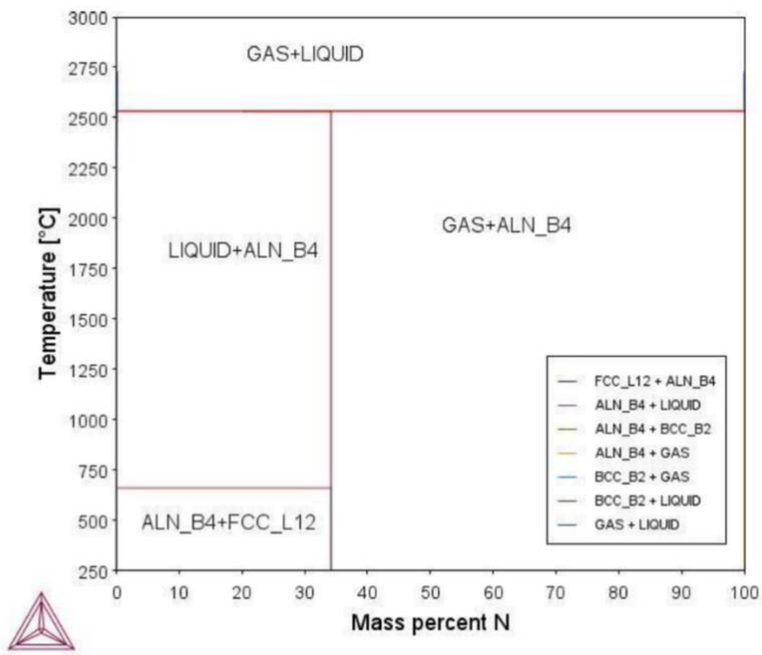

Fig. 1.6: Aluminium Nitrogen Binary Phase Diagram [15]

There can be different nitriding processes which are discussed below:

1.3.1 Salt Bath nitriding

Salt bath nitriding is a surface hardening technique utilized to enhance wear and corrosion resistance, particularly in industries such as automotive, aerospace, and tooling, where durability is of utter importance. It boasts advantages like consistent and precise nitriding, minimal part distortion, and the ability to treat intricate shapes and sizes. However, addressing environmental concerns, notably the disposal of salt bath solutions, is crucial when implementing this process. The procedure typically involves three stages: degreasing, preheating, and nitriding. Degreasing removes surface contaminants, while preheating prevents moisture accumulation. Nitriding occurs in a molten salt bath at temperatures ranging from 550 ^{0}C to 650 °C for several hours [16]. Nitrogen-containing salts like sodium cyanide, along with a reducing agent, decompose at elevated temperatures, allowing nitrogen atoms to potassium cyanide diffuse into the substrate, forming a thin nitride layer. Despite its widespread adoption, salt bath nitriding presents limitations for real-world applications. Cyanide release from carbon and nitrogen sources during heat treatment poses health risks. The toxic nature of the salts used in this process can act as a potent poison, hindering oxygen absorption in human tissues.

1.3.2 Plasma Nitriding

Plasma nitriding, also known as glow discharge nitriding, is a surface hardening technique employed to enhance the wear resistance, hardness, and fatigue strength of metal parts. This process involves placing components within a vacuum chamber where an electrical discharge generates a plasma atmosphere. Within this plasma, comprised of ionized gas species, nitrogen diffuses into the material's surface. During plasma nitriding, nitrogen ions bombard the metal surface, facilitating the diffusion of nitrogen atoms into the lattice structure [17]. This results in the creation of a nitrided layer with improved mechanical properties. Plasma nitriding offers advantages such as precise control over process parameters and uniform treatment across complex geometries. Moreover, its eco-friendliness is notable due to the absence of harmful chemicals. This technique is widely used across industries like automotive, aerospace, tooling, and manufacturing to enhance surface properties for better durability and performance. However, implementing plasma nitriding requires costly equipment and may lead to unwanted tempering of the substrate material due to high current densities required for abnormal glow discharge. Additionally, distortion and deterioration of surface finish may result from continuing to maintain high substrate voltage and gas pressures. Even though the processing temperature is lowered, the resulting compound layer thickness is usually thin and irregular.

1.4 Laser Nitriding

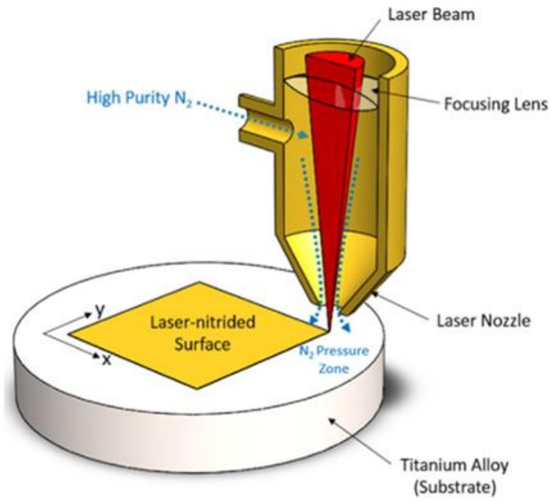

Fig. 1.7: Schematic of Laser Nitriding [18]

Laser nitriding as shown in the Fig. 1.7, is an advanced method for modifying surface properties, aimed at improving the mechanical and tribological properties like hardness, wear resistance, and corrosion resistance of metal components. In this technique, a high-energy laser beam is focused onto the material's surface, generating localized heating. Nitrogen gas is then introduced into this heated region, reacting with the metal to create a nitrided layer. During laser nitriding, the intense heat rapidly heats and melts the metal's surface layer, allowing nitrogen atoms to diffuse into the molten material which results in the formation of nitrides, which enhance the material's surface characteristics significantly [18]. The challenges of conventional laser nitriding can be solved by the laser nitriding process. Precise temperature control during laser treatment promotes uniform compound layer thickness, a task difficult to achieve in plasma nitriding. Compared to salt bath nitriding, laser nitriding eliminates the need for harmful chemical substances, making it a more environmentally and human-friendly process.

1.5 Literature Review

This section presents a detailed literature review on advancements in WAAM of aluminium alloys, including post-processing by laser nitriding and its effects on mechanical and tribological properties.

1.5.1 Current Status on WAAM of Al alloys

The most cutting-edge technique for metal additive manufacturing is WAAM. Three primary parts of WAAM system are the computer control base, wire feeding mechanism, and welding torch/power supply. To enable controlled metal deposition and create the necessary objects, the wire feed and arc generation are managed by the computer control system. The WAAM process has a higher metal wire deposition rate (15 gr/min to 130 gr/min) than the traditional additive manufacturing method. WAAM technology reduces material cost by 7 % to 69%. There is a 40 % to 60 % reduction in fabrication time and a 15 % to 20 % reduction in post-machining time [19]. Three steps make up the entire WAAM process: post-processing, metal deposition, and process planning. Process planning entails creating a 3D CAD model, slicing the model to create a collection of 2D geometries, creating a tool path for each of these 2D geometries, determining the parameters for each layer's deposition, and selecting welding parameters such as feed rate, voltage, and travel speed. Ultimately, the product can be deposited using the tool path and input parameters provided by the WAAM process. A group of techniques known as "post processing" are used to enhance the mechanical and metallurgical qualities. WAAM has appealing features that make it suitable for widespread application across a number of industrial areas. Larger constructions may be produced quickly thanks to the excellent deposition rate and nearly limitless build envelope that come with the package. Small and medium-sized businesses can use AM to shorten the supply chain from production to operation because WAAM has low investment costs [20]. The aerospace and aeronautic industries have been identified by several studies as possible WAAM markets. In these industries, losing weight is crucial to reducing fuel usage. This can be achieved by better designs that increase strength and fatigue resistance but are not possible with milling. Once again, topological optimisation might result in structures that are lighter and slimmer [21]. However, only by addressing the particular materials processing problems can WAAM parts be produced in good quality. The accomplishment of performance metrics pertaining to geometric, physical, and material qualities is the focus of the WAAM materials processing problems. A significant problem in materials processing is the pace of deposition and solidification since it encourages the formation of a microstructure with big columnar grains. According to Cunningham et al., the major performance metrics for a particular area and its quality are determined by the WAAM solidification characteristic, which is composed of the thermal gradient and nucleation rate within the weld pool [22]. In order to understand the arc behavior , Shukla et al. researched the Arc Behavior in WAAM process using process variables like welding current, voltage, and temperature cycles at the base plate [23]. They also used the synchronised high speed arc photographs with each deposited layer. The welding arc intensity was found to progressively grow from first layer to fifth layer, and to roughly stay the same from fifth layer to tenth layer, for a given set of process variables. As a result, bead width expanded progressively from the first to the fourth layer and then roughly stayed the same from the fifth to the tenth layer. Using a 20 mm thick AA6082-T6 plate, Horgar et al. employed traditional gas metal arc welding deposition as a support material for their wire arc additive manufacturing process of AA5183 aluminium alloy. Measurements revealed a relatively high hardness of roughly 75 kg/mm2 in the horizontal plane and between 70 kg/mm2 and 75 kg/mm2 in the vertical plane [24]. Aluminium alloys manufactured through WAAM exhibit mechanical and tribological properties that can match or surpass those of their wrought counterparts. WAAM is particularly well-suited for aluminium alloys due to their high reflectivity, making them challenging to fabricate using laser-based additive manufacturing methods, additionally, WAAM offers a cost advantage, making it an attractive option for producing aluminium components. However, WAAM parts often suffer from defects like porosity formation, residual stresses, delamination, and cracking, limiting their industrial applicability and the range of available alloys. These challenges originate from process stability issues, such as path planning and parameter setup, as well as alloy chemistry. The formation of porosity in the structure can result from the vaporisation of metallic elements during WAAM, especially those with high vapour pressure such as Mg, Zn, and Li. Reports suggest up to 20% magnesium loss in 5000-alloy WAAM, depending on heat input. On the other hand, correlated porosity formation has not received as much attention as the effect of elemental losses on mechanical properties [25]. Porosity defect is a significant issue for WAAM of Al components, according to Gu et al. it was caused by solidification micro voids and hydrogen micro-pores found in deposited alloys [26]. The most prevalent flaw in WAAM of aluminium is hydrogen porosity, which is caused by supersaturated hydrogen precipitating during solidification. The solubility of hydrogen varies in the liquid and solid states of aluminium, which facilitates the formation of porosity [26]. Pores have a substantial impact on the mechanical characteristics of WAAM aluminium parts, resulting in a noticeable reduction in strength and ductility. The main cause of porosity in WAAM aluminium alloys is thought to be hydrogen, which comes from impurities like grease and moisture on the wire surface. At high temperatures, these impurities transform into atomic hydrogen, which is then absorbed by the melt pool to form pores. Studies have shown that adjusting arc pulse frequency and introducing workpiece vibration can reduce porosity in WAAM aluminium alloys [26]. Fusion-based additive manufacturing methods induce residual stresses in materials due to rapid heating and uneven cooling. These stresses, typically tensile, lower the fatigue resistance of components and may cause distortion if they exceed the yield strength or if constraints are removed. Residual stresses are partly dependent on alloy composition, as they have been shown to be linearly related to material hardness in aluminium alloys. In fusion-based joining methods, such as WAAM, solidification cracking is a prominent mechanism, occurring in the liquid melt pool. A number of theories and models have been developed to forecast the susceptibility of aluminium alloys to solidification cracks, taking into account variables such as the fraction of time the alloy is susceptible to cracking [20]. Liberini et al. carried out the optimal process variables selection for wire arc additive manufacturing of structural steels ER70S-6 [27]. The feed rate and the heat input during the weld bead deposition have been changed in order to observe how the temperature reached by the samples can affect the mechanical properties of the final product. The microstructural changes were observed on the variation of process variables within the intended range [27]. Khaled et al. discussed filler wire compositions for Al-Mg-Si alloys, highlighting the role of silicon and magnesium in enhancing strength [28]. Ouyang et al. conducted WAAM trials on 5356-Al, establishing geometric relationships and process parameters [29]. In order to ascertain the inter-layer temperature during WAAM of 5A06-Al, Geng et al. tested geometric constraints and developed a model [30]. WAAM's feasibility in fabricating various aluminium alloy parts has been demonstrated, elucidating defect sensitivity, microstructures, and mechanical properties. The emphasis has shifted to defect control and hybrid manufacturing development for improved mechanical properties in extensively tested alloys such as Al-Cu and Al-Mg. For other alloys, validation of feasibility with different compositions remains a key research area. Compared to laser-based techniques, WAAM offers advantages in depositing high-strength aluminium alloys without cracks. This is because solidification cracks are largely prevented by the lower cooling rates. Notably, after suitable heat treatment, deposited high-strength aluminium alloys exhibit mechanical properties comparable to traditionally fabricated counterparts. Using a DC pulsed GMAW process and 5356 aluminium consumable wire, Derekar et al. examined the impact of cooling time on the porosity and mechanical properties of WAAM parts. Micro-CT was used to examine the distribution of pores in tensile test specimens [31]. Tawfik et. al studied the wall width of the GMAW deposited Al alloy decreases with increase in arc current and increases with increase in travel speed [32]. A detailed review of the past work by different researchers suggest that there a close control over the different process parameters can reduce the defects and willed to develop alluminium alloys of thin sections of superior quality. However, there is a lack of a detailed parametric investigation of the influences of the process parameters of WAAM of thin wall 5356 Al alloy with superior mechanical and tribological properties.

1.5.2 Current Status of Tribological Studies on Additively Manufactured Parts and the Impact of Laser Nitriding on it

When mechanical assemblies are exposed to vibration, they may undergo slight relative motion between their contacting surfaces, resulting in fretting fatigue and wear. Fretting wear arises from repetitive, short-amplitude sliding movements occurring at material interfaces, leading to significant damage such as material disintegration and surface fatigue. This wear type occurs when machine components experience slight movements, either unintentionally in stationary parts or by design in components allowing limited motion. This relative movement, termed "slip amplitude," typically ranges as small as 0.25 microns. It's a combination of adhesive and abrasive wear, where the oscillatory motion induces fatigue wear, compounded by the adhesion of surface asperities. The mechanism of fretting wear begins with pressure and sliding, initiating material adhesion, often referred to as "micro-welding," leading to the transfer of material from one surface to another. Over time, the transferred material oxidizes, forming oxidized wear debris. Due to material adhesion of different foreign material from the counter body and its oxidization there may be generation of the tribofilm [33]. As the powder of wear debris accumulates, it creates more clearance between mating surfaces, intensifying relative movement and consequently increasing the rate of powder generation. Corrosive fretting wear occurs when fretting wear combines with chemical corrosion. Exposure to a corrosive environment speeds up material degradation at the contact interface, resulting in higher wear rates and potential material loss. Corrosion often manifests in fretting conditions, termed fretting corrosion. When material ruptures and debris forms, the fresh surface is exposed to air, making it susceptible to oxidation, depending on the material's inertness. In steel, iron oxide forms and acts as an abrasive due to its hardness. As particles cannot escape the contact, they trigger abrasive wear and subsequent oxidation, perpetuating the process. This can lead to increased wear compared to abrasive or adhesive wear modes alone. Oxidative fretting wear happens when contact surfaces degrade oxidatively from exposure to oxygen or other oxidizing substances. This can result in formation of oxide debris, which can worsen wear by boosting friction and encouraging material erosion. Understanding the specific mechanisms and conditions that lead to fretting wear is crucial for designing materials and lubrication strategies to mitigate its effects and prolong the service life of mechanical components.

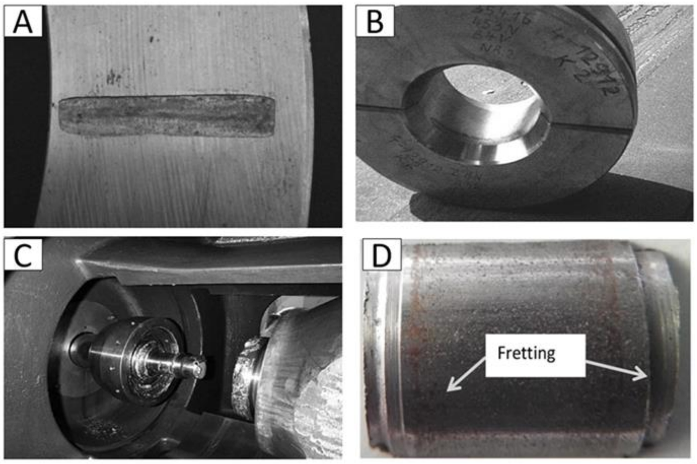

Fig. 1.8: Fretting wear of (A) A centrifugal compressor thrust-bearing support plate with indications of fretting wear, (B) Compressor split ring, (C) Compressor piston rod that failed due to a fatigue fracture, (D) surface of wheelset axle [33]

Aluminium (Al) alloys are extensively utilized across various industries, including automotive, marine, aerospace, and aviation, owing to their moderate strength, lightweight, wear resistance, corrosion resistance, and chemical resistance facilitated by the passivating oxide layer. As particles cannot escape the contact, they trigger abrasive wear and subsequent oxidation,

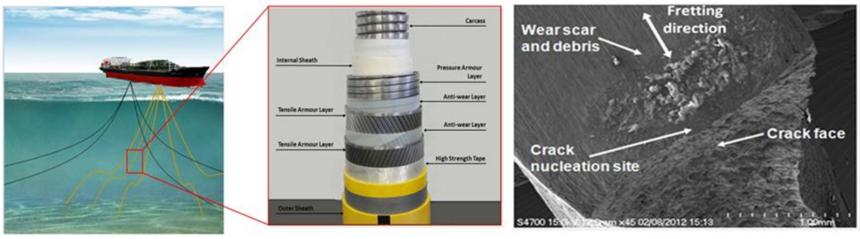

Fig. 1.9: Fretting of Flexible Marine Risers [34]

perpetuating the process. This can lead to increased wear compared to abrasive or adhesive wear modes alone. Oxidative fretting wear happens when contact surfaces degrade oxidatively from exposure to oxygen or other oxidizing substances. This can result in formation of oxide debris, which can worsen wear by boosting friction and encouraging material erosion. Understanding the specific mechanisms and conditions that lead to fretting wear is crucial for designing materials and lubrication strategies to mitigate its effects and prolong the service life of mechanical components. In automotive engines, bolted joints predominantly clamp parts together, and during service, engine vibration can lead to fretting wear, causing accumulation of wear debris and transfer of materials between surfaces, resulting in surface damage and cracking. In marine components like propulsion systems (propeller shafts, bearings, and thrust washers), piping systems (flanges, pipe supports, and connections in piping systems), deck equipment (hinges, latches, and fasteners), mooring and anchoring systems (shackles, chains, and anchors), thrusters and rudders etc. are often subjected to cyclic mechanical loading induced by wave action, vessel vibrations, and operational stresses. These cyclic loads lead to repeated micro-slip motions at the contact interfaces of mating surfaces. The marine environment is highly corrosive due to the presence of saltwater, which can accelerate corrosion processes. The fretting wear in different automobile components as shown in the Fig. 1.8 and in different marine components as shown in the Fig. 1.9 is a serious problem in the industry which has to be adressed at the earliest [33], [34]. Eliminating the failures due to fretting wear requires a clearer understanding of the mechanisms involved. Numerous studies have been conducted on fretting wear and fretting fatigue, with various methods developed to predict fretting fatigue strength. Szolwinski et al. investigated 2024 Al alloy fretting fatigue and proposed a wear prediction model [35]. However, wear exhibits complex effects on fretting fatigue which can degrade strength through surface damage but may also erode initiated cracks, potentially enhancing strength [33], [35]. Zerbest et al. proposed strength prediction methods based on fracture mechanics for Al alloys. The wear response of components sliding against a counter body depends on material parameters such as porosity and second-phase particles, alongside factors like load, test duration, temperature, and humidity [36]. Enhancing the quality of resistant metals could mitigate these issues. Laser nitriding studies on A356 Al alloy by Kulkarni et al. showed increased hardness and fretting wear resistance [37]. Fretting wear can lead to loss of fit, noise, vibration, and fracture, with different fretting regimes observed in galvanized steel [33]. Enhancing fretting wear resistance is crucial for ensuring long-term component serviceability. A great amount of research has been done on nitriding techniques to improve the tribological characteristics of aluminium alloys [18], [37]. Various methods like salt bath, plasma, and gas nitriding have been developed [13], [16], [17]. Salt bath nitriding, while effective, involves hazardous chemicals with negative environmental impacts [16]. Due to the formation of an AlN compound layer, plasma-assisted nitriding significantly increased the wear resistance of aluminium alloy; however, this layer's thickness was only 5 μm, and problems such microcracks and delamination were noted. [17]. It's concluded that achieving a well-adhered and hard AlN layer depends on precise nitriding process parameters, time and temperature. Due to the high current densities required for abnormal glow discharge maintenance, conventional plasma-assisted nitriding suffers from substrate over-tempering. At high substrate voltage and gas pressures, there is also a risk of distortion and surface degradation. Using laser nitriding (LN), which involves irradiating the substrate surface in a nitrogen atmosphere to cause localised melting and the formation of the nitride compound layer, can help overcome these difficulties. The direct application of XeCl excimer laser with a wavelength of 308 nm for laser nitriding (LN) of Al alloy demonstrated optimized parameters [38] which included a frequency of 50 Hz, laser fluence of 1060 mJ/mm^2, and 500 pulses, resulting in a uniform nitride layer and it was also noted that increasing the overlapping percentage gradually reduced surface roughness, leading to a lower fretting coefficient. Zeng et al. conducted experimental investigations on LN of commercially pure Ti and Ti alloys, finding that laser surface melting with Ar containing low nitrogen gas purging yielded crack-free microstructures [39]. Surface properties like wear, hardness, and optical qualities can all be changed with the help of effective laser treatments. These techniques are, however, well-established for use in contained processing environments. Additionally, performing nitriding at specific sites on large and intricate components presents a critical and daunting challenge. To address these obstacles, the flexibility of employing a laser beam for nitriding in an open-air setting, supplemented by N_2 gas purging at specific locations on sizable and complex engine components, emerges as the most feasible and noteworthy solution. Experimental research on laser processing of Ti-6Al-4V by Raghuvir et al. revealed the important role that laser process variables like output power and scanning speed play in improving wear properties and hardness [40]. It was observed that deeper hardening was achieved at lower scan speeds when the laser power was increased, but this also increased surface cracking. According to wear test results, materials that were laser-treated showed a change in mechanism from abrasive to adhesive, which produced a wear resistance that was about twice as high as that of the base material. Laser nitriding is one of the most well-known laser-based surface modification techniques for enhancing the tribological properties of aluminium alloys [18], [37], [38]. Selective laser nitriding techniques effectively address the inherent drawbacks of conventional nitriding techniques, including poor adhesion of the coating to the substrate, reduced fatigue life, rapid delamination of the nitride layer, and undesired substrate heating. Studies on the laser nitriding of aluminium alloys have shown that the quality, surface texture, and uniformity of the resulting nitride layer are directly influenced by the percentage of overlapping [18], [37], [38]. Despite significant attention towards laser nitriding for engineering applications, several factors limit its practical industrial use. Large and complex components like defence torpedoes and car engine blocks are difficult to fabricate homogeneous nitride layers on because the traditional laser nitriding method usually requires a vacuum chamber [18], [41]. Although conventional methods for nitriding large-area components include chemical and plasma nitriding, localised nitriding is still a difficult task. One effective method for locally enhancing the surface properties of large and complex automotive and aerospace components is selective laser nitriding. The effects of open atmosphere laser nitriding on fretting wear performance, however, have not yet been studied, nor have studies into the viability of open atmosphere pulsed laser-assisted nitriding on additively manufactured aluminium alloys been reported.

1.6 Motivation of the Present Study

The present literature shows that WAAM of aluminium many research groups are working and good amount of work has been reported, however, a detailed parametric investigation of WAAM of thin wall 5356 Al alloy is yet untouched. There is a literature gap of influences of the process parameters of WAAM on thin wall fabrication of 5356 Al alloy. A detailed investigation into the tribological aspects of additively manufactured Al alloys is also lacking. So, this present study focusses on the experimental investigation into the different process parameters and its effect on the output responses based on the Box Behnken design of experiments. Also, a detailed study on the mechanical and tribological properties of the thin wall additively manufactured 5356 Al component manufactured at the optimal parameter as suggested by the model, is performed. Literature survey shows that in different conventional nitriding techniques like salt bath nitriding and plasma nitriding, a good amount of work has been reported by different research groups. However, these techniques pose challenges for materials sensitive to heat, like aluminium alloys, as prolonged exposure to elevated temperatures can induce undesired microstructural changes and result in adverse mechanical properties. Consequently, there is a need for alternative approaches to address these issues. In recent decades, laser-assisted nitriding has garnered attention from researchers due to its distinct process advantages. Among various laser induced surface modification techniques, laser nitriding has emerged as a prominent method for enhancing the tribological characteristics of aluminium alloys. By adopting selective laser nitriding, drawbacks associated with conventional nitriding techniques, such as poor coating adhesion, reduced fatigue life, rapid nitride layer delamination, and unwanted substrate heating, can be mitigated. Nevertheless, several factors currently limit the practical industrial application of laser nitriding. Large and complex components like car engine blocks, ship propellers and impellar blades are difficult to achieve a homogenous nitride layer on because the generic laser nitriding process usually requires a vacuum chamber. Furthermore, localised nitriding is still a difficult task, but the selective laser nitriding technique offers a productive way to enhance these components' surfaces [41]. To date, investigations into the feasibility of performing open atmosphere pulsed laser-assisted nitriding on aluminium alloys, as well as the study of open atmosphere laser nitriding's impact on fretting wear performance, are lacking. Also, the effects of laser nitriding on the contact angle are missing. To address these challenges, in this present study, a detailed parametric investigation into the pulsed laser nitriding in an open atmosphere is performed using Nd: YAG laser. The changes in tribological, mechanical and surface properties by the laser nitriding are also studied.

1.7 Research Objectives

The current thesis work aims to perform the parametric optimization of the WAAM of the aluminium alloys and to investigate the mechanical and tribological properties of additively manufactured 5356 Al-alloys for different marine and automobile applications. Laser nitriding is also explored as the post processing technique to enhance to the mechanical and tribological properties. The primary objectives of the thesis are as follows:

i) To carry out the parametric optimization of the Wire Arc additive manufacturing of the parts of the 5356 aluminium alloys based on Box Behnken design

ii) To analyse the mechanical properties like tensile strength, micro-hardness and tribological properties like fretting co-efficient of friction and fretting wear volume of the additively manufactured part of the 5356 aluminium alloys at optimal parameter's settings.

iii) To carry out the parametric optimization of laser nitriding process for enhancing surface properties of additively manufactured part of 5356 Al Alloy based on Box Behnken design.

iv) To analyse the mechanical and tribological properties and contact angle of the laser nitrided surface of additively manufactured part.

This work comprehensively provides adequate insights into the Wire Arc additive manufacturing and it's post processing by open atmosphere laser nitriding process. The experimental results obtained through investigations into fretting wear under different loads and contact angle measurement can be useful for different marine applications.

1.8 Outline of the Thesis

There are five chapters in the thesis, a synopsis of which is provided below.

- Chapter 1: Introduction to Additive Manufacturing and it's post processing by Laser Nitriding
- Chapter 2: Details of Experimental setup used for WAAM of Al alloys and Laser Nitriding of the additively manufactured component
- Chapter 3: Development of Parts of Aluminium Alloy 5356 using wire arc additive manufacturing using Box Behnken design plan of experiments and it's mechanical and tribological studies
- Chapter 4: Laser Nitriding of Wire Arc Additively Manufactured Part of Aluminium Alloy for Enhancing the Mechanical and Tribological Properties
- Chapter 5: Conclusions and future scopes

Chapter 2

Materials and Methods

2.1 Material Specification

Aluminium 5356 alloy was used for deposition having 5% of magnesium as its primary alloying element that improves the corrosion resistance, particularly advantageous in marine applications, while also incorporating 0.05% manganese to enhance its strength. The 5356 aluminium alloy, which belongs to the wrought aluminium-magnesium family, is mostly utilised as a filler for welding. Among the most often used aluminium filler alloys, it has a comparatively high strength. The composition of 5356 Al alloy is displayed in Table 2.1 and its properties is shown in Table 2.2. The alloy provides good weldability and corrosion resistance and finds wide applications in locomotive carriages, chemical pressure vessels, ships, aerospace and aviation industry etc.

Table 2.1: Composition of the 5356 Al alloy

Composition	Mg	Si	Fe	Cu	Mn	Cr	Ti	Al
5336	4.5-5.5	< 0.25	< 0.40	< 0.1	0.05-0.20	0.05-0.20	0.06-0.20	Rest

Table 2.2: 5356 Al alloy properties at 25 °C.

Characteristics	Units	Values
Density	kg/m3	2640
Specific heat capacity	J/kgK	900
Thermal conductivity	W/mK	121.8
Coefficient of thermal expansion	C-1	22.5
Modulus of elasticity	GPa	70
Poisson’s ratio		0.33
Yeild strength	MPa	130

2.2 Wire Arc Additive Manufacturing Setup Details

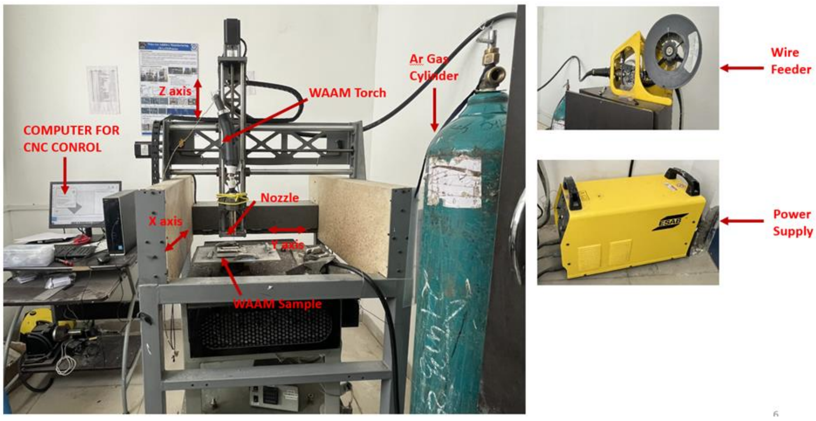

Fig. 2.1: Pictorial view of the WAAM setup

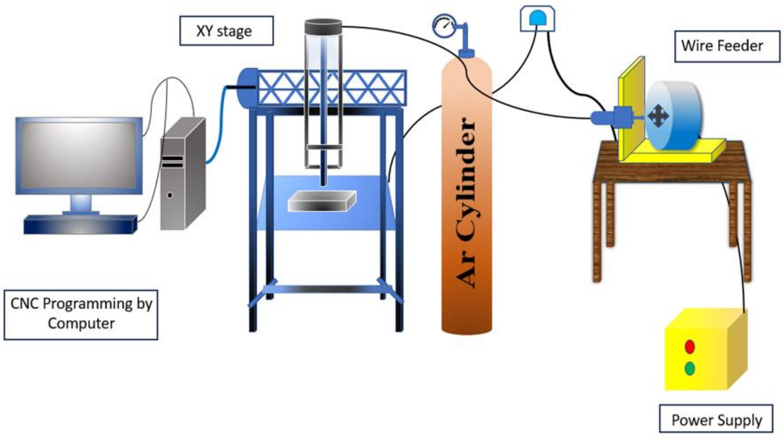

Fig. 2.2: Schematic view of the WAAM setup

Fig. 2.1 and Fig. 2.2 illustrate the pictorial and schematic view of WAAM set up respectively which was used for experimental purpose. Gas Metal Arc Welding (GMAW) based WAAM machine (Make and model by ESAB Inverter MIG 400) is used for WAAM of Al alloy part. The G-codes are used for XYZ movement, Repitier host device software is used to send G-codes to the drivers to drive the DC motors for the movement of the XYZ axis. An argon gas (99.9%) was used for shielding of WAAM deposited samples as a shielding gas according to ISO 14175/I. 5356 al alloy wire of 1mm diameter is constantly feed into metal plate from wire feeder to perform the desired operation. Aluminium alloy plate of the same material with dimension 10 cm x 10 cm x 1 cm was used as a substrate. Prior to the deposition process, the substrate's working face was polished using sandpaper, and any unwanted impurities and oxides were removed from the surface using acetone. To fix the process parameters and their levels, pilot experiments were carried out. Based on the pilot experiments, Box Behnken design was used to perform the experiments with Feed (4 m/min to 6 m/min), Voltage (13 V to 15 V) and cooling time (5 sec to 25 sec) as the process parameters in order to optimize the output responses like Wall Width and Micro-Hardness. All the further mechanical test, tribological tests and laser nitriding are carried on the optimal deposited sample.

2.3 Laser Nitriding Setup Details

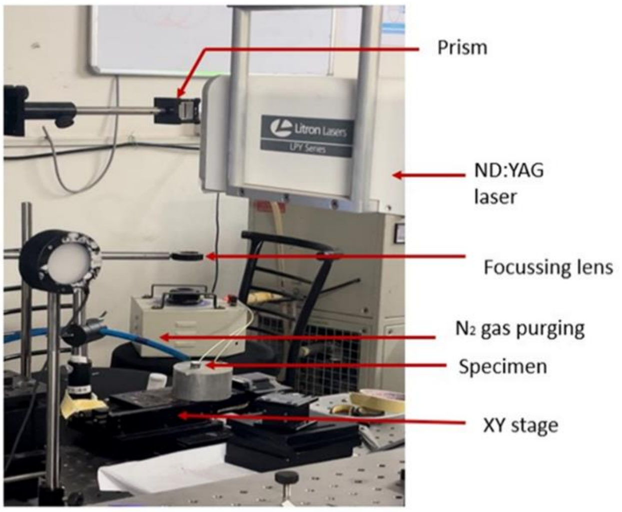

Fig. 2.3: Pictorial view of the Laser Nitriding setup

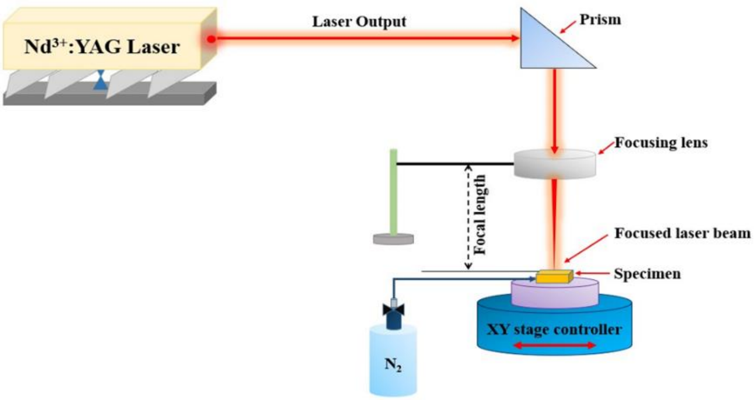

Fig. 2.4: Schematic view of the Laser Nitriding setup

The laser nitriding was carried out by pulsed Nd3+: YAG laser (Litron laser model no. LPY764G-10) as shown in Fig. 2.3 and Fig. 2.4 using the fundamental 1064 nm wavelength, with the laser beam generated in a Q-Switch mode with a pulse duration of 9 nanoseconds and operating at a repetition rate of 10 Hz. To create the N_2 gas, a source of liquid nitrogen was used. A novel approach to the nitriding process was investigated, which included heating liquid nitrogen with an externally applied voltage to turn it into a gas. The liquid nitrogen's expansion ratio of roughly 1:700, which suggests that vaporising the nitrogen could produce a larger concentration of nitrogen gas molecules for the nitriding process, served as the impetus for this. A 3 mm internal diameter flow pipe was used to introduce the gas, and a constant 1 cm gap was kept between the specimen's surface and the gas flow pipe's outlet. Box Behnken design was used to perform the experiments with N_2 gas flow rate (6 l/min to 24 l/min), laser fluence (60 J/cm^2 to 180 J/cm^2) and overlapping percentage (80 % to 90 %) as the process parameters in order to optimize the Micro-Hardness as the output response. All the further mechanical test, tribological tests are carried on the optimal laser nitrided sample.

2.4 Mechanical Testing

Different mechanical testing like Micro-Hardness test and Micro Tensile test are performed on the WAAM deposited sample and laser nitrided sample and it's effects are studied.

2.4.1 Micro Tensile Test

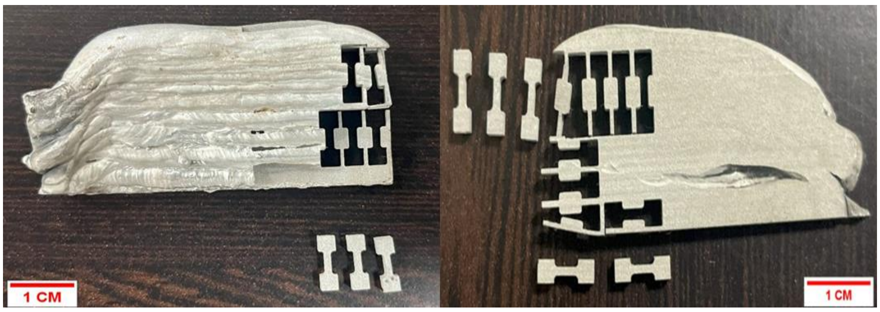

Fig. 2.5: Tensile Test Sample

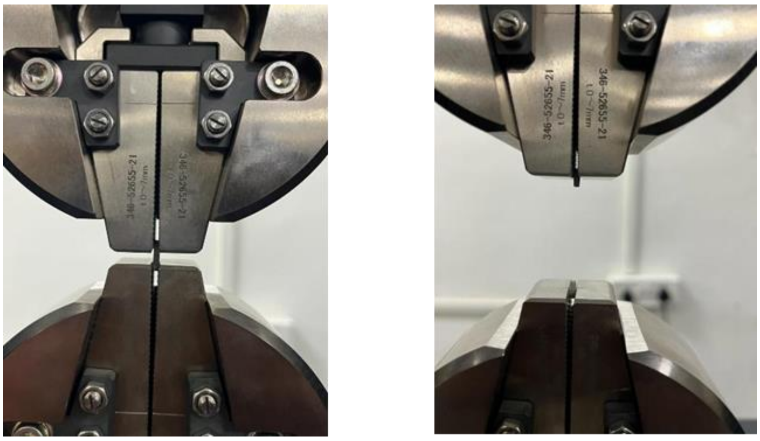

Fig. 2.6 Micro-Tensile Test of WAAM manufactured Al alloy

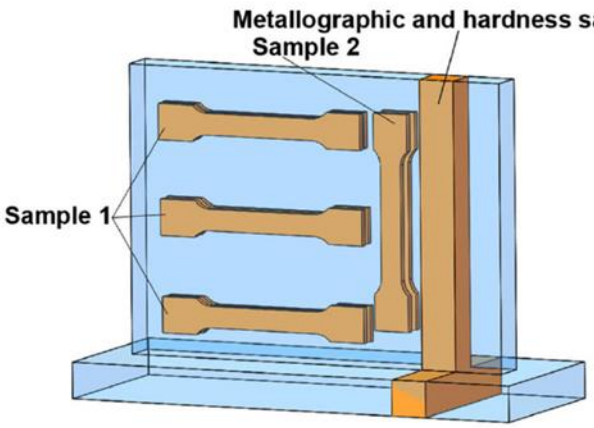

Fig. 2.7: Schematic diagram of the additively manufactured part representing the positions of the micro tensile, metallographic and micro-hardness test samples

The tensile test samples were made by sectioning the WAAM deposited al wall by wire cut EDM as shown in the Fig. 2.5. As seen in Fig. 2.7, the samples were made in two directions: parallel to the substrate and perpendicular to the substrate. A universal tensile tester machine (Tinius Olsen, Model: H50KL) was used to perform the tensile test at room temperature and a loading rate of 1.5 mm/min, as illustrated in Fig. 2.6.

2.4.2 Micro-Hardness measurement

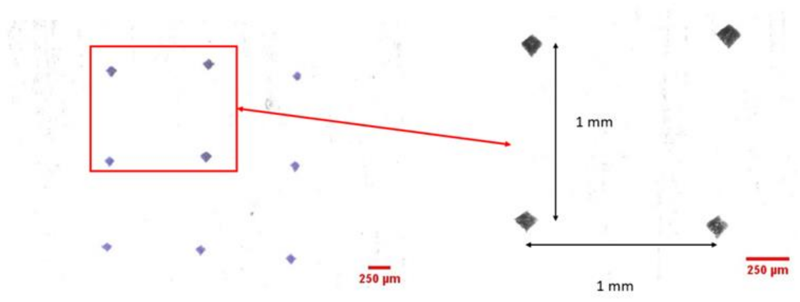

Fig. 2.8: Vickers Micro-Hardness Test Indentation Images

Micro-hardness testing was performed using Micro Vickers VH-1MDX (Economet VH-1MDX) with 200 g load and 15 s dwell time at the middle section of each sample at 5 different locations and the average of these values was reported. Apart from that the micro-indentation for micro hardness measurement of the WAAM deposited sample under optimal parametric setting, is observed along the deposition with 1 mm interval as shown in the Fig. 2.8. To find out how laser nitriding affected the micro-hardness, a micro-hardness test was also run across the surface of the laser nitrided sample.

2.5 Tribological Testing

The tribological properties of the WAAM deposited sample and laser nitrided sample are studied and compared using fretting wear test, contact angle measurement and corrosion test.

2.5.1 Fretting Wear Test

The wear tests were conducted at room temperature using the pin on flat type arrangement by fretting wear test setup (Make and Model by DUCOM) as shown in the Fig. 2.9 with a cast iron pin as the counter body. The experiments were performed at four different loads (2 N, 4 N, 6 N, 8 N) and the other parameters such as the frequency of 20 Hz, the oscillating amplitude of 300 microns and the time 15 mins were kept constant. It should be mentioned that each test was run three times, with the average values being reported, to guarantee the repeatability of the experimental data. The data acquisition system provided the variations in the instantaneous coefficient of friction (COF). Following the completion of every test, the specimens were thoroughly cleaned in an ultrasonic bath with ethanol, and the wear scar diameter was determined using the SEM image.

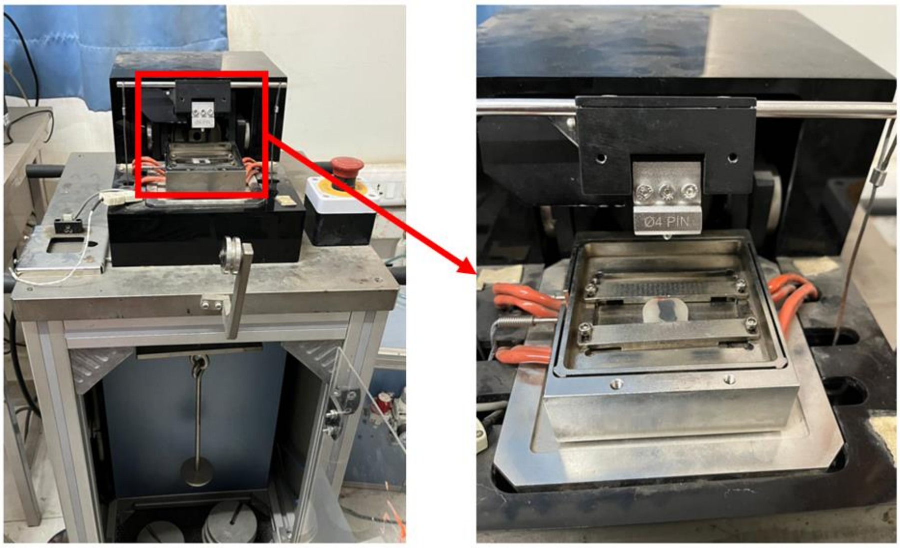

Fig. 2.9: Fretting Wear Setup

The wear track profile was obtained with the help of a 2D contact profilometer (Model SJ-410, Mitutoyo). The wear volume and wear morphology were obtained with the help of optical profilometer (Make and Model by Profilm 3D, Filmetrics).

2.5.2 Contact Angle Measurement

A contact angle goniometer (Make and Model by Holmarc) as shown in the Fig. 2.10 was used for the measurement of the contact angle of untreated WAAM sample and laser nitrided sample using distilled water and salt water.

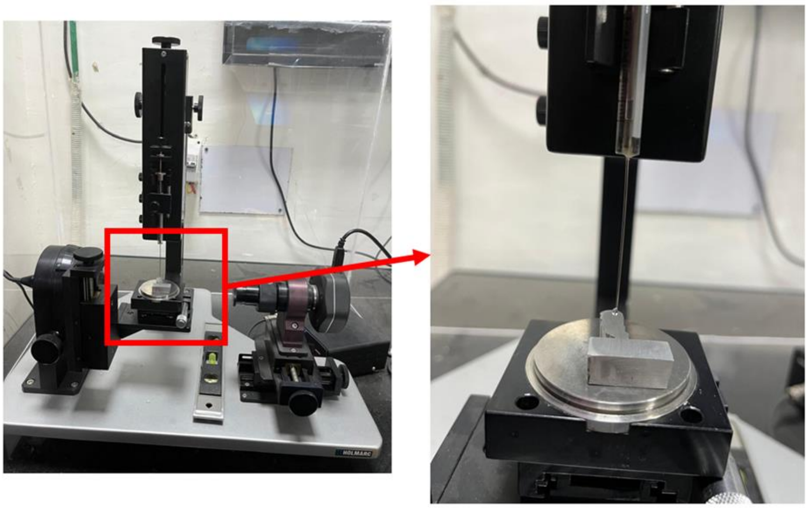

Fig. 2.10: Contact Angle Measurement Instrument

2.6 Microstructural Analysis

Sections of the WAAM deposited sample were used to create the specimens for microstructure analysis, as illustrated in Fig. 2.7. The specimens were polished to 2000 grit paper and then polished with 1 μm and 0.25 μm paste of diamonds. Keller's reagent was used to chemically etch the samples for 25 seconds, and an inverted optical microscope was used to view the microstructure. Table 2.3 below displays the composition of the Keller's reagent.

Table 2.3: Keller's reagent composition

Ingredients	Distilled water	Nitric Acid (HNO_3)	Hydrochloric Acid (HCL)	Hydrofluoric Acid (HF)
Volume (ml)	190	5	3	2

2.7 Characterization Techniques of Materials

The WAAM deposited sample and laser nitrided sample is studied using various characterization techniques for material confirmation. The morphological characterization is performed using Field Emission Scanning Electron Microscopy (FE-SEM) and physical characterization of material is preformed using Energy Dispersive Spectroscopy (EDS) and X-Ray diffraction.

2.7.1 Field Emission Scanning Electron Microscopy (FESEM):

To study the morphology and its variations over the different energy variations, FE-SEM is used. It is a high-resolution technique where electron beam emitted by field emission source strikes the surface of the sample placed under it. It is then raster scanned to obtain the microstructure and surface morphology at varying magnifications. The inner arrangement of setup is such that the ejected electron beam passes through an arrangement of magnetic lenses and metal apertures in a vacuum tube for focusing as a thin monochromatic beam. when incident electron beam interacts with sample, it generates output beams in the form of backscattered electrons, secondary electrons, Auger electrons and characteristic X-rays with different detectors collecting each type of electron and hence produces images of the sample specimen. the elastic interaction between sample and electron beam excelling out of source leads to back scattered electrons creations. However, there are electrons which do not interact with nucleus of the specimen are reflected back or backscattered from the sample. it is observed that backscattered electron depends on the atomic weight of element. Due to stronger deflection from bigger nucleus, the element with higher atomic mass generates higher number of backscattered electrons. It gives a better information of composition and topography of the sample.

Figure 2.11: Field Emission Scanning electron microscope (FE-SEM)

The inelastic interaction between sample and electron beam generates secondary electrons. due to loss of inelastic interaction, the energy is less than backscattered electrons. The secondary electron detector is positioned at an angle to the axis of incident beam to improve the efficiency of detector. Secondary electrons help to study the surface morphology of sample. In this study, a Field-emission scanning electron microscope (FE-SEM, JEOL JSM-7400F) as shown in the Fig. 2.11. is employed to study the morphology of WAAM deposited sample and the laser nitride sample

2.7.2 Energy Dispersive Spectroscopy (EDS)

Energy Dispersive Spectroscopy (EDS) is an analytical technique utilized alongside scanning electron microscopy (SEM) to determine the elemental composition of materials. By bombarding a sample with a focused electron beam in the SEM, EDS detects characteristic x-rays emitted from the sample's atoms. When the high-energy electrons displace inner-shell electrons, subsequent electron transitions emit x-rays with energies specific to the elements present. These emitted x-rays are captured by an energy-dispersive detector, which records their energies. The resulting energy spectrum reflects the elemental composition of the sample. Through spectral analysis, peaks in the spectrum are correlated with known elemental standards to identify the elements within the sample. EDS is invaluable in fields like materials science, geology, forensics, and biology, offering insights into a sample's chemical makeup, distribution, and morphology at the microscopic level. Its non-destructive nature and high sensitivity make it a versatile tool for a wide range of applications, from identifying trace elements in geological samples to characterizing the elemental composition of biological tissues. EDS facilitates detailed analysis, aiding researchers in understanding the properties and behavior of diverse materials. In this study, the compositional analysis of WAAM deposited sample and laser nitride sample was carried out using Energy Dispersive Spectroscopy (EDS) which was coupled with the FE-SEM as shown in Fig. 2.11.

2.7.3 X-Ray Diffraction

X-Ray diffraction technique is a non-destructive often used to identify and analyze the crystal structure, degree of crystallinity and availability of impurity phases if any**.** It works on the principle that when a high-energy beam falls over a target material, energy absorption happens, and electrons jumps from inner to outer shell thus in an unstable state condition. Due to natural tendency of electrons to reach back to initial stable state, the electrons come back to its original state thus releasing X-rays. The electrons moving from M shell to K shell generates $K\beta$ x-rays and the ones moving from L shell to K shell generates $K\alpha$ x-rays. The basic principle of analysis of XRD is based on Bragg's law as shown in the Fig. 2.12 which states that "When a collimated beam of x-rays strikes a crystal, the atoms act as diffraction centers and the diffracted beams combine to give diffraction patterns.".

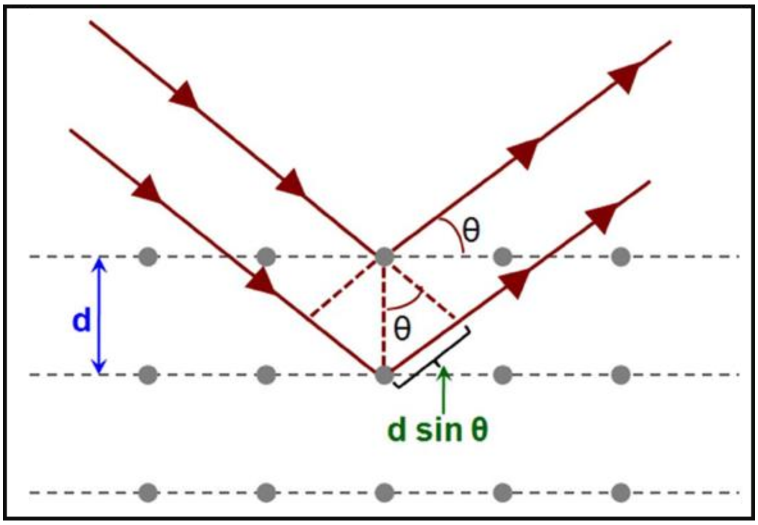

Fig 2.12: Bragg's Law in a 2-D crystal

For n^{th} order diffraction, using the X-rays of wavelength λ, the Bragg'sequation is:

$$n\lambda = 2d \sin\theta \qquad (2.1)$$

The phases were studied using Grazing Incidence X-Ray Diffraction (GI-XRD) by Cu-Kα radiation at an incident angle of 3◦.

2.7.4 3D scanner

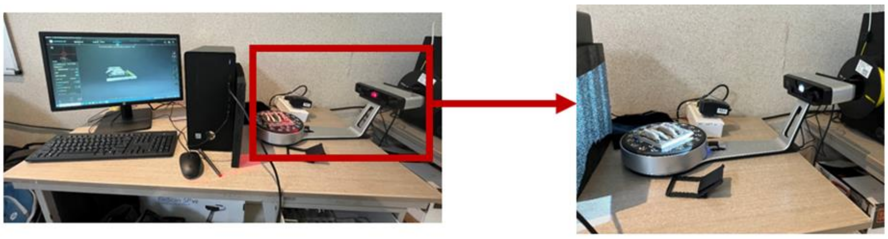

Fig. 2.13: 3D scanning of WAAM deposited sample

The EinScan-SP V2 is a cutting-edge desktop 3D scanner designed by Shining 3D, renowned for its precision and user-friendly operation. Utilizing Structured Light Scanning (SLS) technology, this scanner ensures high-quality scans with exceptional accuracy. It offers both Fixed Scan modes: with and without a turntable, providing versatility to accommodate various scanning needs. With an impressive scan accuracy of up to 0.05 mm (0.002 in), the EinScan-SP V2 delivers detailed and precise 3D models of objects. Despite its remarkable precision, it maintains a fast-scanning speed, capturing a single scan in just 4 seconds and completing an automatic scan mode in only 1 minute. This scanner supports texture scanning and exports files in commonly used formats like STL, OBJ, and PLY. Its intuitive software simplifies the scanning process and offers comprehensive editing and processing capabilities. In this study, a EinScan-SP V2 SPECS Desktop 3D Scanner is employed to study the overall geometry of WAAM deposited sample as shown in the Fig. 2.13.

2.7.5 Contact Profilometer

2D contact profilometry is a technique used to measure the surface profile and topography of a material or object in two dimensions. This method involves physical contact between a stylus or probe and the surface being measured. In the present study 2D contact profilometry as shown in the Fig. 2.14 is used to measure the wear track profile.

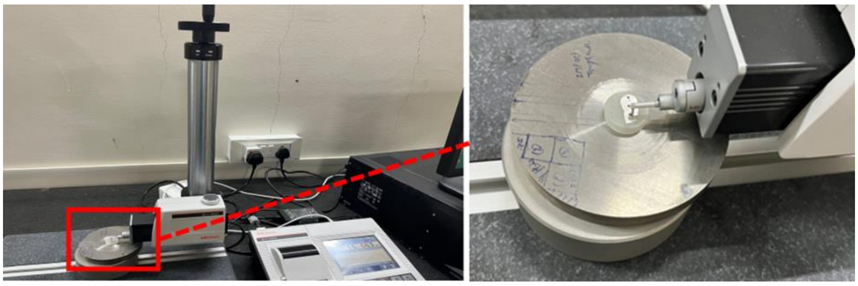

Fig. 2.14: 2D Contact Profilometry

2.7.6 Optical Surface Profilometer

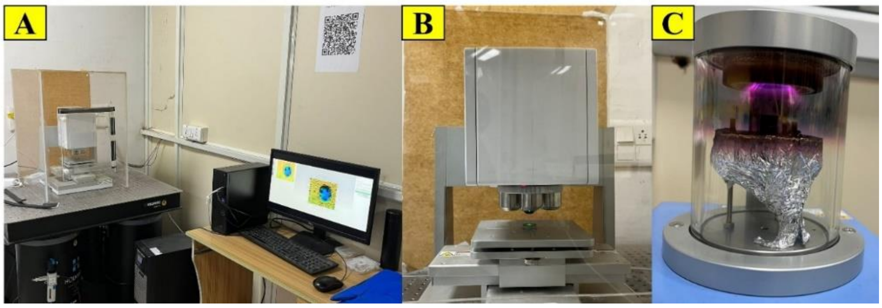

Fig. 2.15: (A, B) Optical Surface Profilometry, (C) Gold coated sample preparation

Optical surface profilometry is a non-contact measurement technique used to characterize the surface topography of materials. It involves using light to measure the height variations on a surface, allowing for the creation of detailed 3D maps of surface features. In this present study, the wear volume and wear morphology were obtained with the help of optical profilometer (Make and Model by Profilm 3D, Filmetrics). The fretting wear samples were gold coated as shown in the Fig. 2.15 (C) to enhance the quality and accuracy of the imaging.

Chapter 3

Experimental Investigation into Wire Arc Additive Manufacturing (WAAM) of Aluminium Alloy

In this chapter the parametric optimization of the WAAM process parameters and its effect on the output responses like Micro-Hardness and wall width of the deposited Al alloy wall has been incuded. The mechanical and tribological performance of the WAAM deposited Al part at the optimal parametric condition have also been discussed.

3.1 Pilot experiments to fix the process parameter

Pilot experiments were performed to know the significant influences of the process parameters of WAAM on the quality of the produced part. Based on the pilot experiments, the process parameters were selected for the Behnken design of experiments model for the parametric optimization of the WAAM deposited aluminium part.

3.1.1 Influence of standoff distance on WAAM of aluminium alloy

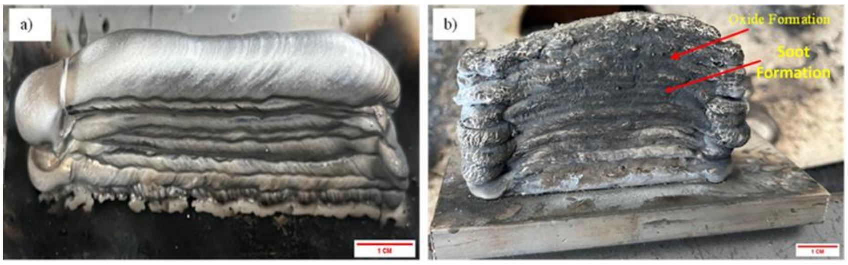

Fig. 3.1: Photographic view of deposited aluminium alloys with change of standoff distance (a)15 mm (b) 20 mm

It was observed that increase of SOD (standoff distance) from 15 mm to 20 mm resulted in the increase of oxidation and provides uneven at the surface of the workpiece as shown in Fig. 3.1. Higher distance provides greater exposure for the oxidation at the surface of workpiece which makes the surface quality poor. Apart from that, the argon at higher standoff distance provides inefficient shielding of WAAM of aluminium alloys. Da Silva et al. [42] investigated the presence of soot (also known as smut) on the top surface of the last deposited layer. Soot as a black residue that appears on the aluminium surface as shown in the Fig.3.1 (b) during welding, particularly when using 5xxx series filler alloys in gas metal arc welding. Because the deposition process's operational feature is its ability to prevent undesired oxidation, the amount of black soot trapped on the surface can serve as an evaluation criterion. According to Anderson, soot consists of finely divided metal oxides and, while unattractive, is not harmful. Vinicius et. al [43] further explained that this material was primarily composed of magnesium oxide (MgO). If removed immediately, soot can be easily wiped off, but if left for a few hours, it may require brushing. Although cleaning of surface is common in welding operations, it is not desirable in WAAM due to the need for continuous deposition of multiple layers without cleaning in between for productivity reasons. The soot left between passes can affect arc stability in welding operations [43]. Therefore, it is crucial to assess whether the presence of soot impacts the effectiveness of thin walls produced by WAAM. In the present study it was observed that the presence of soot was drastically reduced by reducing the SOD as shown in the Fig. 3.1 (a). Analysis revealed that standoff distance lower than 15 mm should be preferred for carrying out operation of WAAM aluminium alloys. However very low SOD will increase the chances of damage to the nozzle, so a constant SOD of 14 mm was kept throughout the further experiments.

3.1.2 Influence of argon gas flow rate on WAAM of aluminium alloys

Argon gas flow rate has a significant impact on shielding of the WAAM deposited Al part in order to avoid any unwanted contamination and oxidation. Due to highly reactive nature of Al alloy, the chances of oxide formation are immense in an open-air deposition. Oxide formation reduces wettability, leading to molten aluminium’s agglomeration and decreased flowability. Da Silva et al. pointed out that in WAAM of thin walls, heat builds up beneath the deposition layer [42]. As a result, with the same deposition parameters, the molten pool in thin parts can become larger and more elongated, potentially extending beyond the area protected by the shielding gas provided by conventional torch nozzles. This exposure can lead to hydrogen absorption from the atmosphere where the pool is not fully shielded. A WAAM deposition process's metal transfer regularity is an operational characteristic since it has a strong correlation with arc stability and spattering. Furthermore, it is widely acknowledged that the shielding gas controls metal transfer. It is observed that the flow of argon gas should be controlled in order to get a uniform deposition without discontinuity and spatter. As demonstrated in Fig. 3.2 (a, b, and c), spatter deposition resulted from an increase in the Argon gas flow rate beyond 18 l/min. This is mainly due to the instability of the molten pool due to the increased pressure of the Argon gas flow. However, a low gas flow rate and higher SOD led to entrapped black soot over the lateral surface of the walls, which is commonly known as soot as shown in the Fig. 3.1 (b). Therefore, in the present study Ar gas flow rate is kept constant at 18 l/min throughout the experiments. However, the Ar gas flow rate doesn't show any significant impact on the track width.

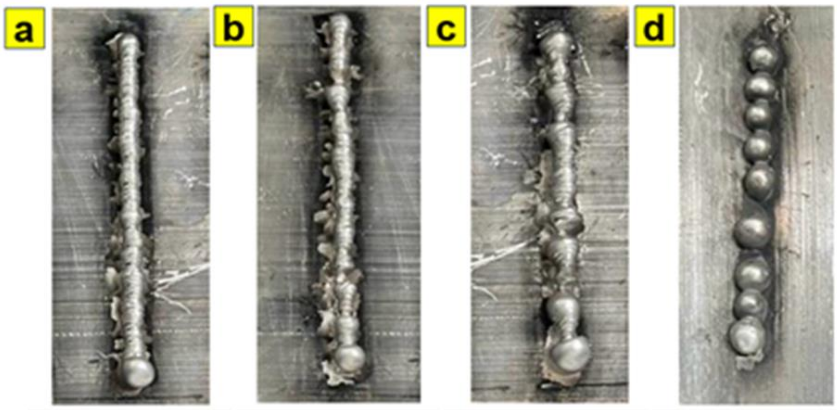

Fig. 3.2: Photographic view of deposited aluminium alloys with change of Argon gas flow rate (a)18 l/min (b) 19 l/min (c) 20 l/min (b) 21 l/min

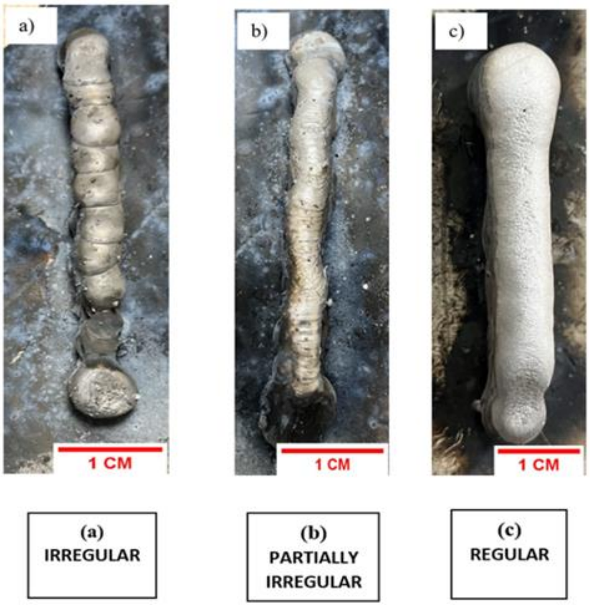

Fig. 3.3: Photographic view of deposited aluminium alloys with change of feed rate (a) 3 m/min (b) 4 m/min, and (c) 5 m/min

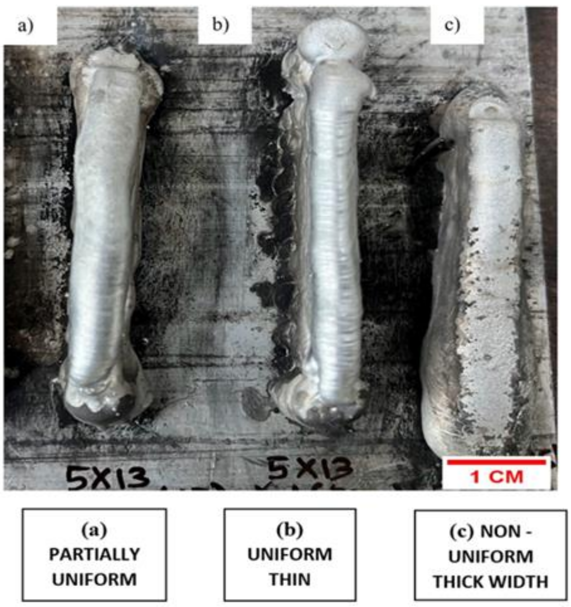

Fig. 3.4: Photographic view of deposited aluminium alloys with change of cooling time (a) 20 Seconds, (b) 15 Seconds, (c) 0 Seconds

3.1.3 Influence of feed rate on WAAM of aluminium alloys

Fig. 3.3 shows the photographic view of deposited aluminium alloys with change the of feed rate when other process variables such as standoff distance, voltage, and cooling time were held constant at 14 mm, 14 V, and 15 seconds respectively. It was found that with the increase of feed rate from 3 m/min to 5 m/min, the deposited aluminium alloy structure changes from a segmented, irregular, and narrow structure to a better uniform and regular structure with a considerable increase in width. This is because higher feed provides more deposition of aluminium alloys which provides uniformity over the surface. With the increase in feed, there was an increase in track width due to increase in the material volume of deposition. However, a minimum wire feed is required to avoid the discontinuous track deposition as shown in Fig. 3.3.

3.1.4 Influence of cooling time on WAAM of aluminium alloys

Ding et al. observed that during the deposition process with constant parameters (such as welding current, arc voltage, travel speed, and wire feed speed), variations in the width and height of the layers can be observed [44]. This phenomenon is primarily due to the thermal saturation of the previously deposited layers. When a new layer is deposited onto a preheated layer, the spreading and formation conditions of the material change. This state can be explained by the temperature of the previous layer, also known as the sublayer temperature, which is influenced by the cooling time [45]. To investigate this effect during the experiment, the time between deposition passes (layers) was varied. As a result, the previous layer cools to different temperatures in different experimental samples, while within each individual sample, each layer cools for the same duration. Fig. 3.4 shows the photographic view of deposited aluminium alloys to study the influence of cooling time on the uniformity of deposited layer when other process variables such as standoff distance, voltage, and feed rate were held constant at 15 mm, 14 V, and 5m/min respectively. It was observed that with the increase of cooling time from 0 seconds to 15 seconds, uniformity in the deposited aluminium material was observed which then decreases on further increase of cooling time to 20 seconds. Every material has its cooling time requirement for the achievement of uniformity throughout the surface. Depending on the process variables employed, it was observed that better uniformity of deposited layer of aluminium alloys was achieved at cooling rate of 15 seconds. Thus, it was held constant and further studies were employed by varying the power voltage as discussed in subsequent section.

3.1.5 Influence of voltage on WAAM of aluminium alloys

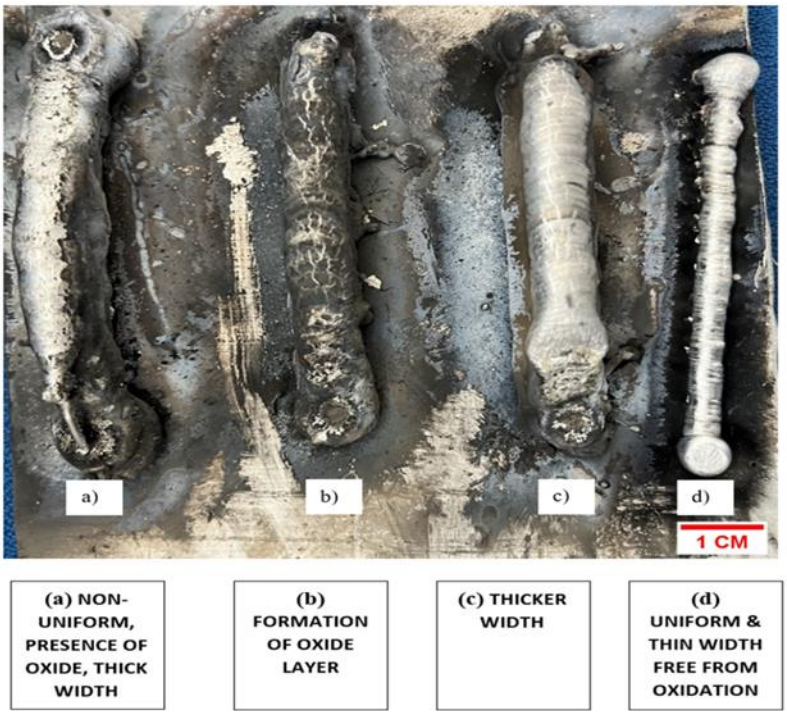

Fig. 3.5: Photographic view of deposited aluminium alloys with change of voltage (a) 18 V, (b) 17 V, (c) 15 V, (d) 14 V

Fig. 3.5 shows the photographic views to study the influence of applied voltage on the deposited aluminium alloys when other process variable such as SOD, cooling time, and feed rate were held constant at 14 mm, 15 seconds, and 5 m/min respectively. It was observed with the increase of power voltage from 14 V to 18 V, surface oxidation increases with corresponding increase in width and heat affected zone around the periphery of deposited aluminium alloys. It is due to high power which causes spattering while deposition of material on workpiece plate. With increase in voltage, there is a deposition of more molten material which results due to the spreading of the melted droplets and due to spreading of the arc there is no effective shielding of the deposited sample which is resulting into oxidation as shown in the Fig. 3.5 (b). Based on overall studies using one factor at a time, it was observed that feed rate of 5 m/min, power voltage of 14 V, cooling time of 15 Seconds, and standoff distance of 14 mm provide better results. The results thus obtained were further utilized into mathematical modelling for the optimization of responses using Box Behnken design of experiments as shown in Table 3.1 and Table 3.2.

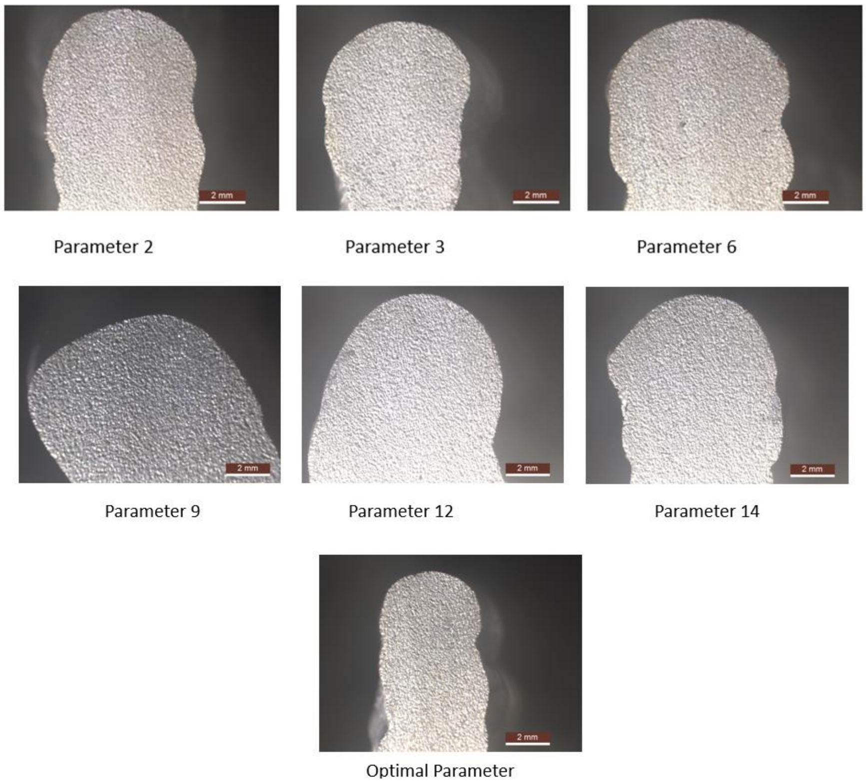

Fig. 3.6: Optical Images of the cross-section of the deposited wall at different parameters

Table 3.1: Process variables and their levels

Process Variables	Units	Levels		
Feed Rate	m/min	4	5	6
Voltage	V	13	14	15
Cooling Time	sec	5	15	25

Table 3.2: Experimental design and value of responses based on Box Behnken method

Sl.No.	Feed rate (m/min)	Voltage (V)	Cooling time (sec)	Wall Width(mm)	Micro hardness (HV)
1	4	13	15	5.97	65.78
2	6	13	15	6.65	67.9
3	4	15	15	6.35	66.69
4	6	15	15	6.49	67.2
5	4	14	5	9.54	65.71
6	6	14	5	7.7	67.2
7	4	14	25	5.66	67.65
8	6	14	25	8.4	68.2
9	5	13	5	9.79	65.95
10	5	15	5	8.35	67.8
11	5	13	25	6.63	68.84
12	5	15	25	8.25	67.905
13	5	14	15	7.52	65.74

3.2 Development of Mathematical Modelling of the Responses based on Box Behnken Design

The experiments thus carried based on the design of Box Behnken method also provide the relation between process variables and the responses undertaken which were shown below:

$$\boldsymbol{Wall\ Width\ (mm)} = 7.52 + 0.215x + 0.05y - 0.805z - 0.7925x^2 - 0.3625y^2 + 1.0975z^2 - 0.135xy + 1.145xz + 0.765yz$$ **Eq. (3.1)**

$$\boldsymbol{Micro\ hardness\ (HV)} = 65.7067 + 0.5838x + 0.1406y + 0.7419z + 0.376x^2 + 0.8098\,y^2 + 1.1073z^2 - 0.4025xy - 0.2350\,xz - 0.6962\,yz$$ **Eq. (3.2)**

where,

$x = feed\ rate\ (\frac{m}{min})\ ;\ y = voltage\ (V)\ ;\ z = cooling\ time\ (sec)$

The above empirical relations thus obtained using MINITAB software were further checked based on F-ratio and p value for the accuracy of the developed mathematical models for wall width and micro hardness. The ANOVA results of wall width and micro hardness are shown in Table 3.3 and 3.4.

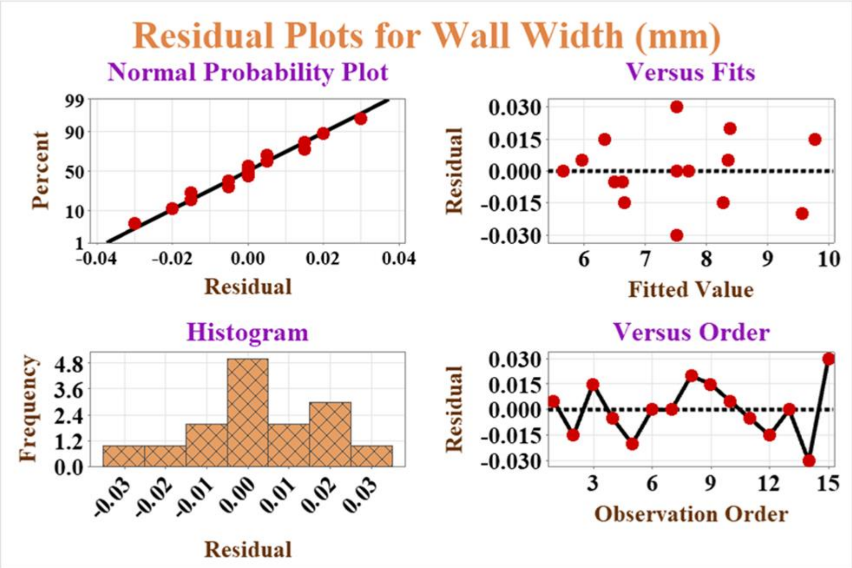

Fig. 3.7 Residual Plots for Wall width

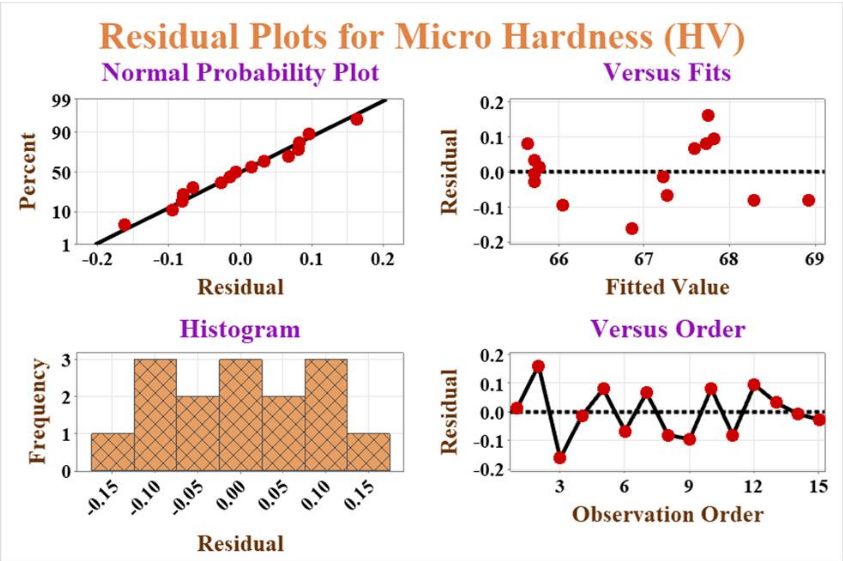

Fig. 3.8 Residual Plots for Micro Hardness

Table 3.3: Analysis of Variance of wall width

Source	DF	Adj SS	Adj MS	F-Value	P-Value
Model	9	21.0869	2.34299	3254.15	0.000
Linear	3	5.5740	1.85800	2580.56	0.000
Square	3	7.8550	2.61833	3636.57	0.000
2-Way Interaction	3	7.6579	2.55263	3545.32	0.000
Error	5	0.0036	0.00072		
Lack-of-Fit	3	0.0018	0.00060	0.67	0.646
Pure Error	2	0.0018	0.00090		
Total	14	21.0905			

As per Table 3.3, it is seen that p-value for Linear, Square and 2 Way interaction of the process variables of regression model are lower than 0.05 which means that these are significant. The Lack of Fit computed F value for wall width was found to be 0.67 and its p value is 0.646 which is higher than 0.05. Thus, the lack of fit is insignificant and the model is significant. The calculated value of R-Sq = 99.98%, R-Sq (adj) =99.95 %, and R- Sq (pred) = 99.84 % which is sufficiently high. As a result, the created models fit the observed data well.

Table 3.4 Analysis of Variance of Micro-Hardness

Source	DF	Adj SS	Adj MS	F-Value	P-Value
Model	9	16.7861	1.86513	86.44	0.000
Linear	3	7.2873	2.42911	112.58	0.000
Square	3	6.6908	2.23027	103.36	0.000
2-Way Interaction	3	2.8080	0.93599	43.38	0.001
Error	5	0.1079	0.02158		
Lack-of-Fit	3	0.1060	0.03534	1.86	0.16
Pure Error	2	0.0019	0.00093		
Total	14	16.8940			

As per Table 3.4, it is seen that p-value for Linear, Square and 2 Way interaction of the process variables of regression model are lower than 0.05 which means that these are significant. The Lack of Fit computed F value for wall width was found to be 1.86 and its p value is 0.16 which is higher than 0.05. Thus, the effect of lack of fit is negligible and can be considered insignificant. The fitting of the data in the model is significant. The calculated value of R-Sq = 99.36%, R-Sq (adj) =98.21 %, and R- sq (pred) = 89.93 % which is sufficiently high. As a result, the created models fit the observed data well. Fig. 3.7 & Fig. 3.8 show the residual plots for wall width and microhardness respectively. The discrepancies between the response values predicted by the model and the observed response values at each factorial value combination are known as residuals. These help to determine the validity of the model for the currently selected response. Since all of the points on the residual probability plot fall on the line with little scatter, the residuals may follow a normal distribution, indicating that the data is well-fit for the model. The residuals are plotted against the fitted, or predicted, values of the chosen response in the Residual vs. Fitted plot. A normal probability plot of the residuals is a useful tool for demonstrating the validity and robustness of the ANOVA test. If all the required assumptions are met by the normal probability plot of residuals, the ANOVA test results are deemed effective and appropriate for the regression models that have been developed [46]. Consequently, it is crucial to use the normal probability plot to validate the results. The normal probability plot for wall width, where all residuals align in a straight line, is displayed in Figure 3.7. The fact that there is no residual clustering and the errors are normally distributed suggests that the regression models for wall width that have been developed are fit. Figure 3.8, which displays the normal probability plot for Micro-Hardness, makes a similar observation. As a result, it can be said that every design variable used in this study has a big impact. In the Residuals vs. Fit plot, the number of points with positive residuals above the dotted line equals the number of points with negative residuals below the dotted line, indicating a good fit of the model and equality in variance between the data. The plot of the residual histogram indicates that the distribution of the data is normal. The residuals are plotted against the order of runs that were used in the design in the Residual vs. Order plots. Since there is no discernible pattern and the points are dispersed randomly throughout the plot, the experiment's test sequence is ineffective and the data points are unrelated to one another [46].

3.3 Parametric influences of voltage, cooling time and feed rate on wall width

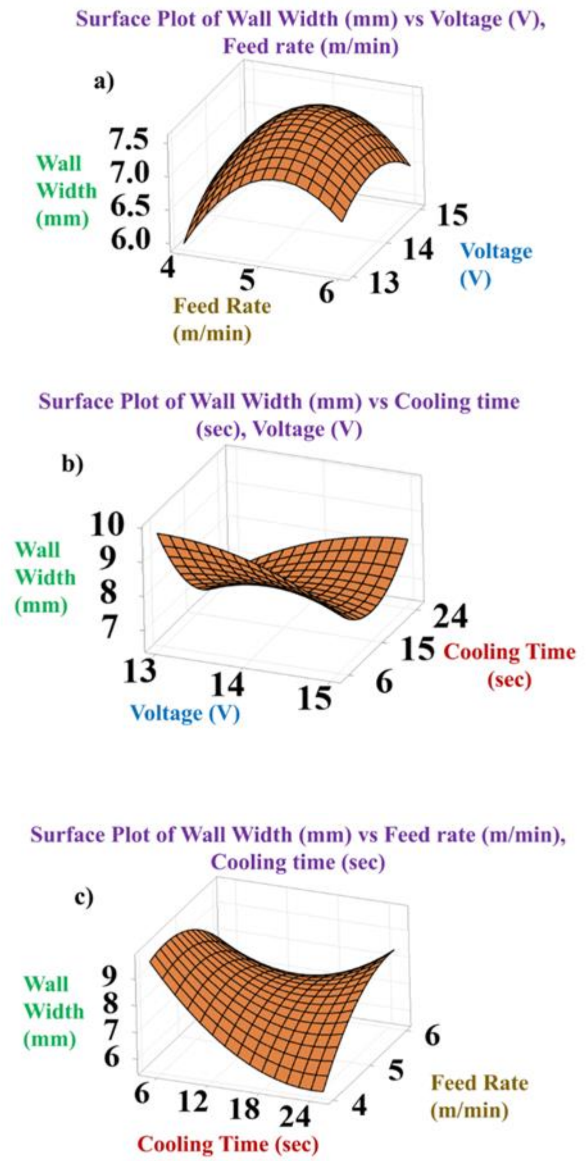

Fig. 3.9: Surface plots of wall width with respect to (a) voltage and feed rate, (b) cooling time and voltage and (c) feed rate and cooling time

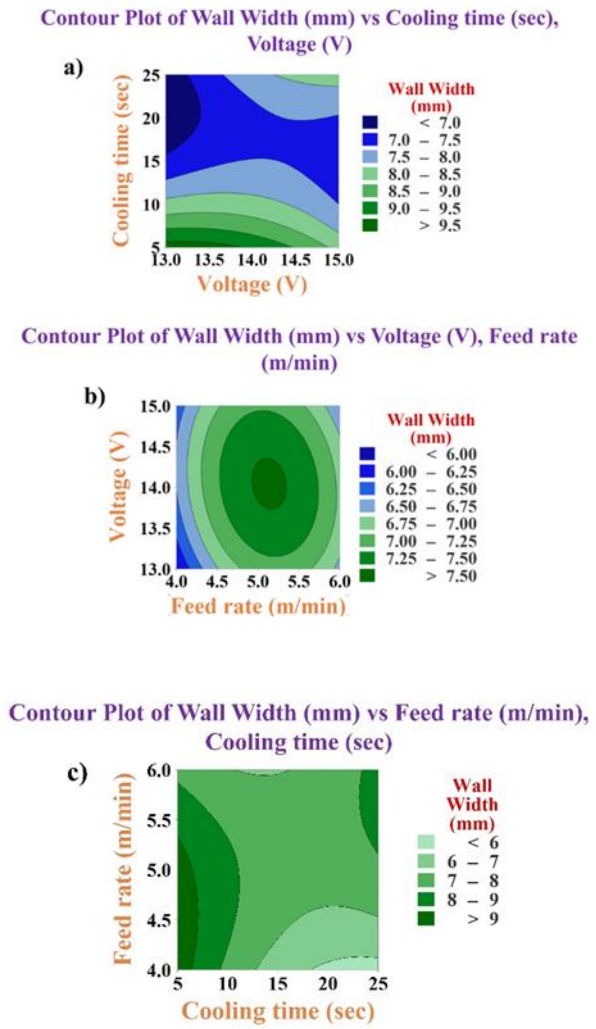

Fig. 3.10: Contour plots of wall width with respect to (a) cooling time and voltage, (b) voltage and feed rate, and (c) feed rate and cooling time

Fig. 3.9 (a) shows the effect of feed rate and power voltage on wall width when cooling time was held constant at 15 sec. It was observed that increase in feed rate and power voltage increases the wall width upto 7.5 mm. The increase in feed rate results in increase in the wire fusion speed because of the continuous arc whereas increase in power voltage increases the heat input to the material. As a result, more material melts and gets deposited at the workpiece surface which helps in increasing wall width. Analysis revealed that feed rate of 5 m/min and power voltage of 15 V yields maximum wall width**.** Fig. 3.9 (b) shows the effect of cooling time and power voltage on wall width when feed rate was held constant at 5 m/min. It was observed that increase in power voltage increases the wall width and reaches a maximum value of 9 mm at a power voltage of 15 V whereas increase in cooling time from 6 sec also resulted in the increase of wall width and achieve a maximum value at a cooling time of 24 sec. This happens due to greater heat energy input and simultaneously oxidation which resulted in the increase of wall width. Attempt was also made to observe the effects of wall width when voltage was held constant at 14 V. Fig. 3.9 (c) shows the effect of cooling time and feed rate on wall width when voltage was held constant at 14 V. It was observed that increase in cooling time resulted in the decrease of wall width and attained a minimum value of 6 mm due to more time exposure for heat to get rid of from material surface whereas increase in feed rate resulted in the increase of wall width. Increase in feed rate produces uniformity with increase in more material deposition at workpiece plate which resulted in the increase of wall width. Apart from that, contour plots were also shown which will be helpful to analyse the region for the achievement of better wall width as shown in Fig. 3.10. Fig. 3.10 (b) shows the contour plot of feed rate and power voltage on wall width when cooling time was held constant at 15 sec. It was observed that in order to have minimum wall width power voltage should be set in the range of 13 V to 13.5 V whereas feed rate lower than 4.5 m/min should be used. Fig. 3.10 (a) shows the contour plot of cooling time and power voltage on wall width when feed rate was held constant at 5 m/min. It was observed that in order to have minimum wall width power voltage should be set in the range of 13 V to 13.5 V whereas cooling time in the range of 20 sec to 25 sec should be used. Fig. 3.10 (c) shows the contour plot of cooling time and feed rate on wall width when voltage was held constant at 14V. It was observed that in order to have minimum wall width, feed rate lower than 4.5 m/min whereas cooling time in the range of 20 sec to 25 sec should be used.

3.4 Parametric influences of voltage, cooling time and feed rate on micro hardness.

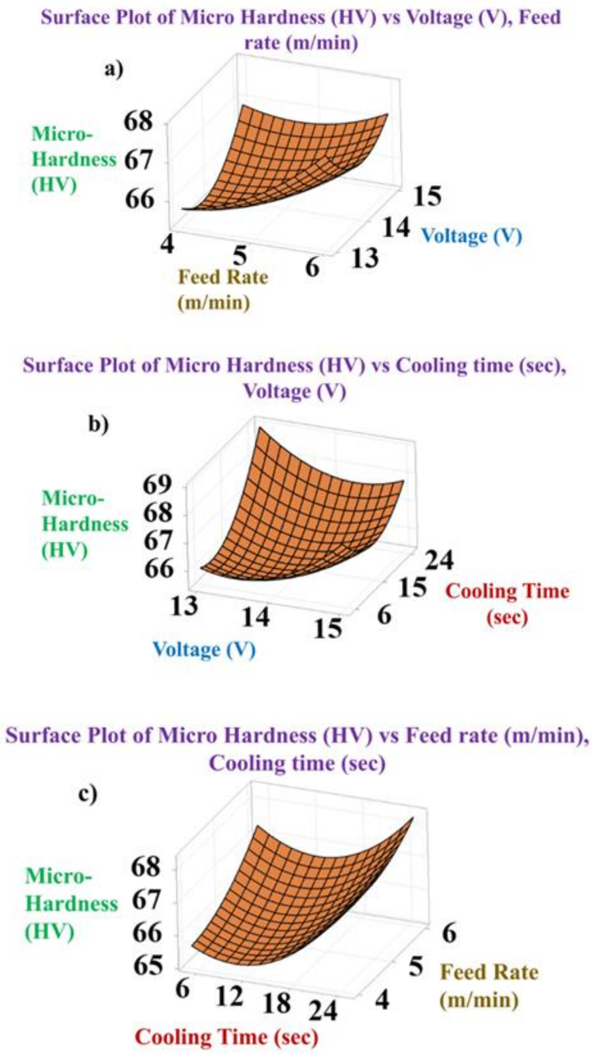

Fig. 3.11: Surface plots of Micro Hardness with respect to (a) voltage and feed rate, (b) cooling time and voltage and (c) feed rate and cooling time

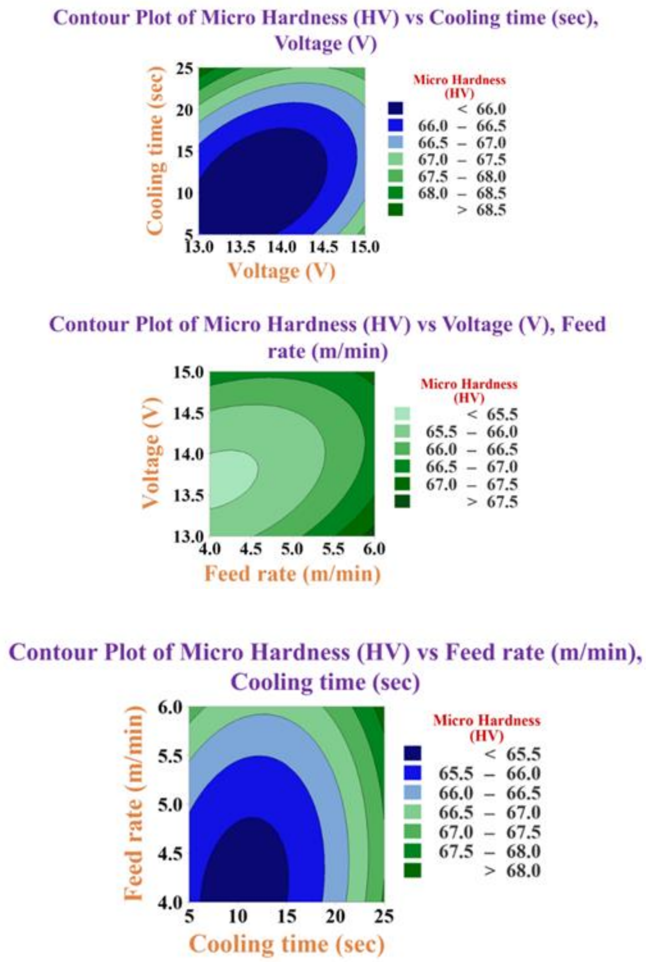

Fig. 3.12: Contour plots of Micro Hardness with respect to (a) voltage and feed rate, (b) feed rate and cooling time, and (c) cooling time and voltage

Fig. 3.11 (a) shows the effect of feed rate and power voltage on micro hardness when cooling time was held constant at 15 sec. It was observed that increase in feed rate and power voltage increases the wall micro hardness upto 67 HV. It is because increase in feed rate results in increase in the wire fusion speed because of the continuous arc whereas increase in power voltage increases the heat input to the material. As a result, more material melts and gets deposited at the workpiece surface which helps in increasing wall micro hardness. Analysis revealed that feed rate of 6 m/min and power voltage of 15 V yields maximum wall micro hardness. Fig. 3.11 (b) shows the effect of cooling time and power voltage on micro hardness when feed rate was held constant at 5 m/min. It was observed that increase in power voltage decreases the wall micro hardness and reaches a minimum value of 66 HV at a power voltage of 14 V whereas increase in cooling time from 6 sec resulted in the increase of wall micro hardness and achieve a maximum value of 69.6 HV at a cooling time of 24 sec. This happens due to greater heat input and simultaneously oxidation which resulted in the increase of wall width. Attempt was also made to observe the effects of wall hardness when voltage was held constant at 14 V. Fig. 3.11 (c) shows the effect of cooling time and feed rate on micro hardness when voltage was held constant at 14V. It was observed that increase in cooling time resulted in the decrease of wall micro hardness to 65 HV whereas further increase resulted in the increase of micro hardness to a maximum value of 68 HV due to the intensive solidification of the material which leads to the increase in hardness whereas increase in feed rate from 4 m/min resulted in the increase of wall micro hardness to 68 HV due to more amount of material deposition at workpiece. Apart from that, contour plots were also shown which will be helpful to analyse the region for the achievement of better wall hardness as shown in Fig. 3.12. Fig. 3.12 (b) shows the effect of feed rate and power voltage on micro hardness when cooling time was held constant at 15 sec. It was observed that in order to have maximum wall hardness power voltage should be set in the range of 13 to 15 V whereas feed rate higher than 5.5 m/min should be used. Fig. 3.12 (a) shows the effect of cooling time and power voltage on micro hardness when feed rate was held constant at 5 m/min. It was observed that in order to have maximum wall hardness power voltage should be set in the range of 13 to 13.5 V whereas cooling time in the range of 20 sec to 25 sec should be used. Fig. 3.12 (c) shows the effect of cooling time and feed rate on micro hardness when voltage was held constant at 14 V. It was observed that in order to have maximum wall hardness, feed rate higher than 5.5 m/min whereas cooling time greater than 23 sec should be used.

3.5 Single and multi-objective optimization based on desirability function analysis

On the basis of the proposed mathematical models, the analysis of every individual response has been done in order to obtain the maximum micro hardness and minimum wall width. The upper limit of desirability function (D) is supposed to have a weight value of 1 for optimum value of the responses. For WAAM of aluminium alloys, the software MINITAB was used to optimize the responses using desirability function analysis. Each column of the optimization graph that is subsequently obtained corresponds to a factor. The graph's rows each represent a response. While all other parameters are fixed, each graph cell illustrates how one response varies as a function of one of the process variables. The experimental design's high and low settings are shown by numbers at the top of each column, while the row coloured in red denotes the present values of the process variables that should be used to achieve the goals. Response goal, desired value, current y factor, and desirability value are provided to the left of each row.

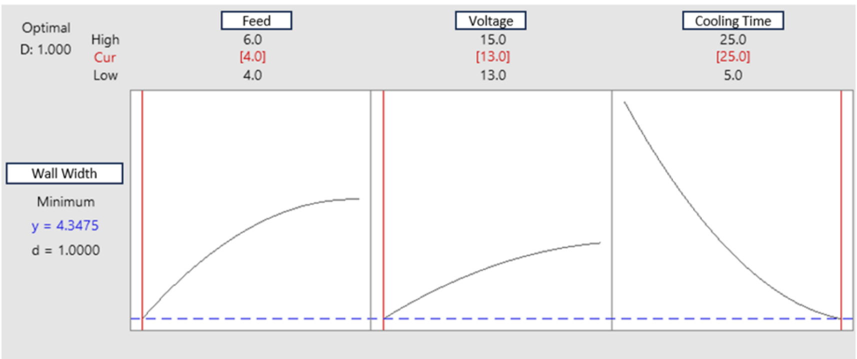

Fig. 3.13: Optimization plot for wall width

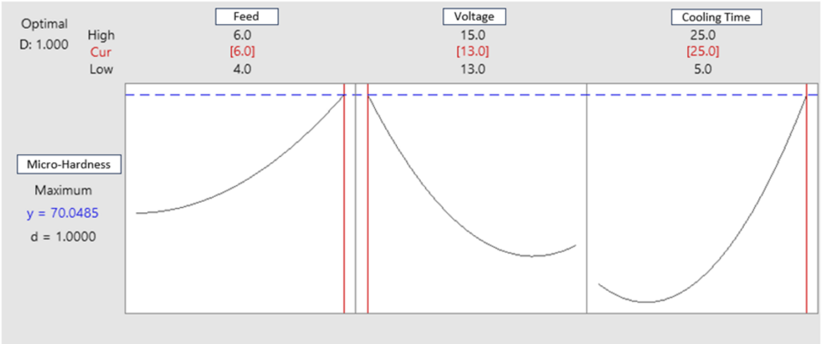

Fig. 3.14: Optimization plot for micro hardness

Fig. 3.13 and Fig. 3.14 show the findings of single-objective optimization of the responses. It was observed from Fig. 3.13 that the optimal process variables settings required for achieving minimum wall width, feed rate of 4 m/min, power voltage of 13 V, and cooling time of 25 sec should be used. From the Fig. 3.14 it was observed that for maximum value of micro hardness, feed rate of 6 m/min, power voltage of 13 V, and cooling time of 25 sec should be used

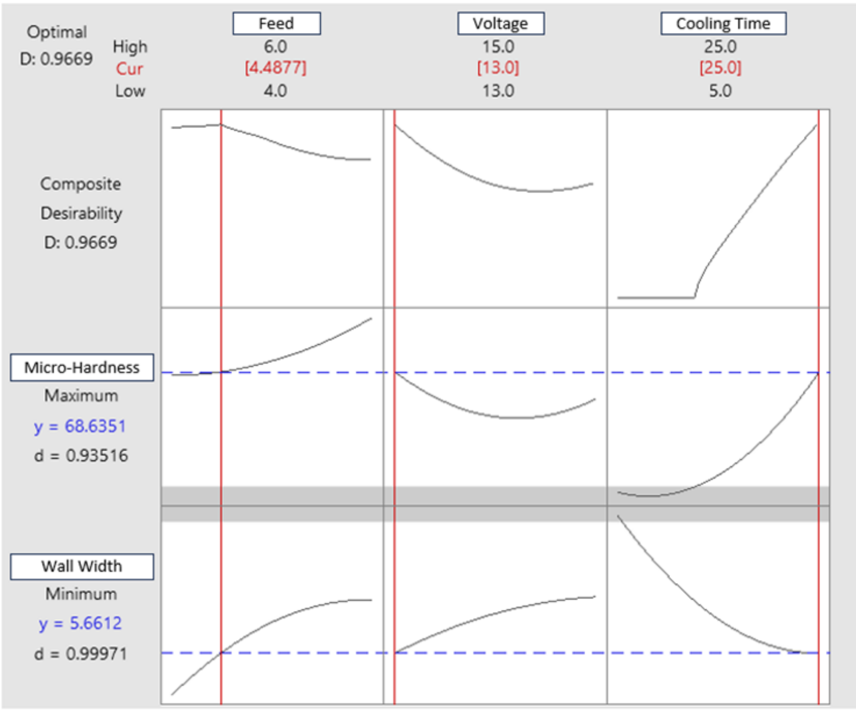

Fig. 3.15: Multi objective optimization of responses

In addition to single objective optimization, efforts were also made to carry forward multi objective optimization of the responses and results is shown in Fig. 3.15. It is observed that the current optimal process parameter settings obtained for wall width and micro hardness is found at feed rate of 4.5 m/min, power voltage of 13 V, and cooling time of 25 sec. Experiments are performed at optimal parametric settings in order to observe the error produced while performing experiment. After carrying out experiment at optimal process variables settings, it was observed that actual value of wall width obtained was 5.82 mm and actual value of micro-hardness was obtained as 71.2 HV. The results were further utilized to predict the error in percentage using equation 3.

$$\text{Error (\%)} = \frac{\text{Predicted Value - Actual Value}}{\text{Predicted Value}} \times 100 \qquad \textbf{Eq. (3.3)}$$

Percentage of prediction error was calculated by Eq. (3.3). Upon analysis, it was observed that the percentage of prediction error of Wall width was 2.805 % and that of micro-hardness was 3.737 % which is less than 5 %. Thus, above designed mathematical modelling is suitable for WAAM of aluminium alloys.

3.6 Microstructural Analysis at Optimal Condition

Various process parameters such as voltage, current, wire feed rate, interpass temperature, flow of shielding gas, among others, can influence the extent of oxidation and other issues [47]. When heated aluminium comes into contact with the oxygen in the ambient air it forms a strong aluminium oxide layer (Al_2O_3) by exothermic reaction [48]. The effects of oxidation change the mechanical properties and thus affects the part quality adversely.

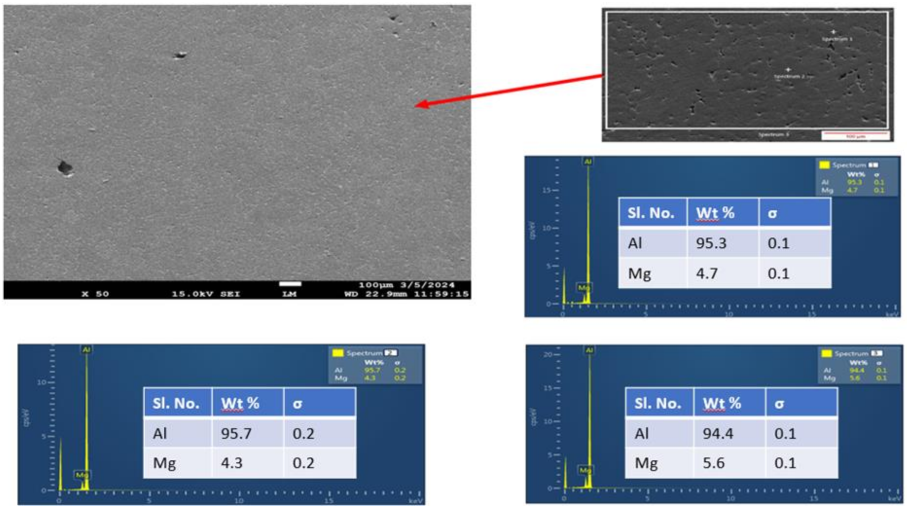

Fig. 3.16: Point EDS (Spectrum 1 & Spectrum 2) and area EDS (Spectrum 3) results of the deposited sample surface at the optimal parameter

The elemental confirmation of the additively manufactured aluminium part is done by performing EDS analysis on the WAAM deposited sample at the optimal parametric setting as shown in the Fig. 3.16 which confirms with the composition of the 5356 al alloy filler material used. It is found that the WAAM deposited sample shows different grain distribution at different regions primarily mainly due to the different heat distribution and multiple heating and cooling cycles [49]. As seen in Fig. 3.17 (c), it is observed that the bottom region's area with good heat dissipation is primarily made up of finer grains.

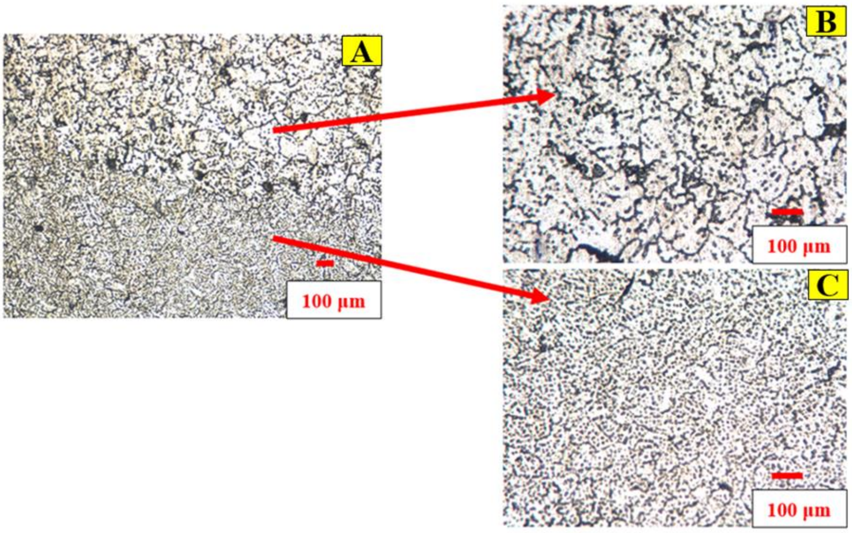

Fig. 3.17: Microstructure of WAAM deposited Al alloy wall at different locations: (a) intermediate region, (b) top region, (c) bottom region

As seen in Fig. 3.17, the middle region's grains are coarser due to low heat dissipation efficiency and constant heat transfer from the top region to the middle region. As seen in Fig. 3.17 (a), the rate of heat dissipation in the top region is further decreased, resulting in higher heat accumulation and coarser grain size than that in the middle region. There is a transition of the finer grains to the courser grains at the intermediate region as shown in the Fig. 3.17 (a). Near the substrate, heat generated during deposition is efficiently dissipated through it [49]. However, as the deposition height rises, the buildup of thickness between layers increases, intensifying heat accumulation. Consequently, this heightened accumulation can cause variations in the material's cooling rate, potentially resulting in the formation of minor voids and cracks [50].

3.7 Micro-Hardness Analysis at Optimal Condition

Fig. 3.18 shows the distribution of the micro hardness measurement of additively manufactured 5356 al alloy at the optimal parameter setting as obtained from optimization analysis. The average hardness obtained is 73.2 HV. The average hardness of the top, middle and bottom region are 72.2 HV, 72.6 HV and 74.8 HV respectively. The average hardness of the substrate is 60.02 HV. The hardness of the WAAM sample is comparatively more than that of the substrate because rapid solidification occurs in the additive manufacturing which results in the formation of the finer grans and hence more hardness. In addition to that, the additive manufacturing processes often induce residual stresses in the manufactured component due to rapid heating and cooling cycles. These residual stresses can cause work hardening, which can increase the hardness of the material [51]. It is noted that the average hardness of the bottom region is maximum followed by the middle and the lowest region as shown in the Fig. 3.18. As the grains in the bottom region are relatively smaller than the top region as shown in the Fig 3.17, the hardness is more in the bottom region. Moreover, as the bottom layer is deposited on the base substrate, it shows better heat dissipation in compare to the middle region which remains hottest as it is squeezed between the top and the bottom regions. Microhardness decreases as deposition height increases because the deposition layer's rate of heat dissipation slows down and the grains grow higher [52].

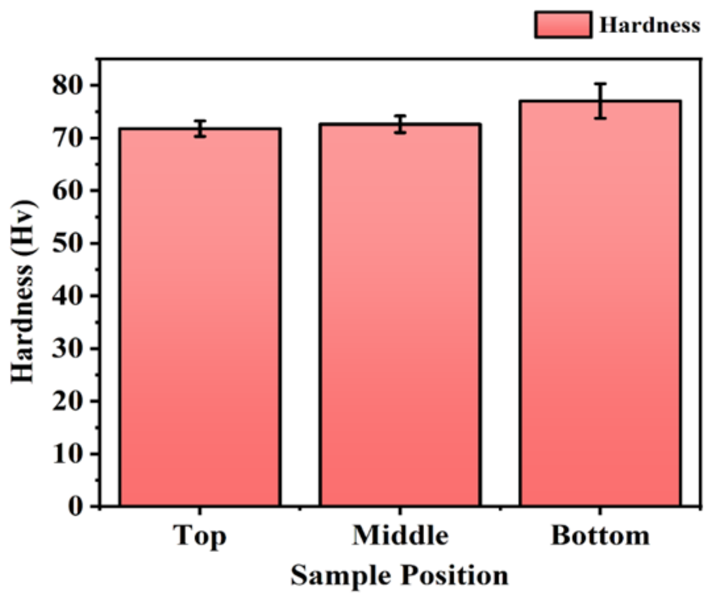

Fig. 3.18: Micro Hardness at different location of the WAAM deposited sample at optimal parameter setting

Table 3.5: Tensile testing result of WAAM of aluminium alloys at optimal parametric settings

Region	UTS (MPa)	YS (MPa)	Elongation (%)
Bottom (transverse)	262.972	129.2813	38.21783
Middle (transverse)	257.0466	125.3263	39.31288
Top (transverse)	252.2059	105.8893	39.57259
Vertical (longitudinal)	251.7197	88.4634	41.59176
Average	257.4082	120.1657	39.67376

3.8 Tensile Testing Analysis at Optimal Condition

The results of the tensile test in the upper transverse region show that the elongation (EL) is approximately 39.57%, the yield stress (YS) is 105.89 MPa, and the ultimate tensile stress (UTS) is 252.21 MPa. In the middle transverse section, the EL is approximately 39.31%, the YS is 125.33 MPa, and the UTS is 257.05 MPa. The YS is 129.28 MPa, the EL is approximately 38.22%, and the UTS is 262.97 MPa in the bottom transverse section.

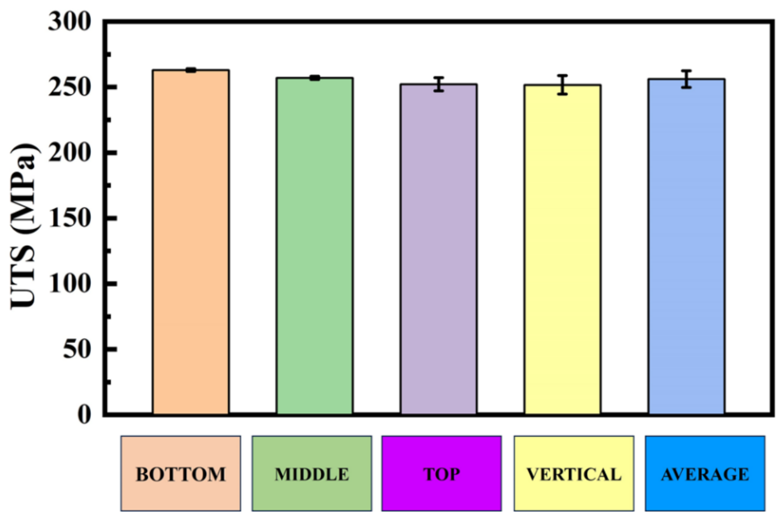

Fig. 3.19: Ultimate Tensile Strength of the sample at different Regions

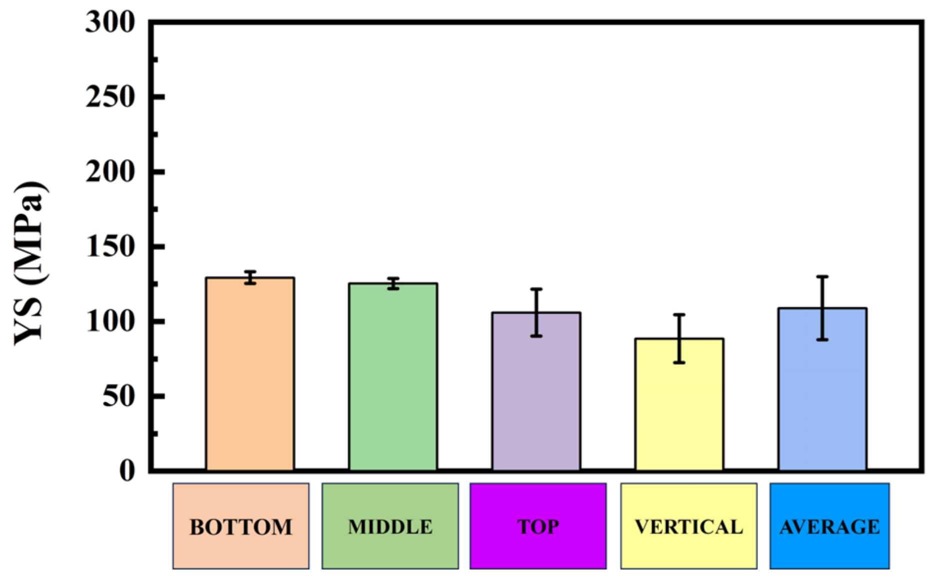

Fig. 3.20: Yield Strength of the sample at different Regions

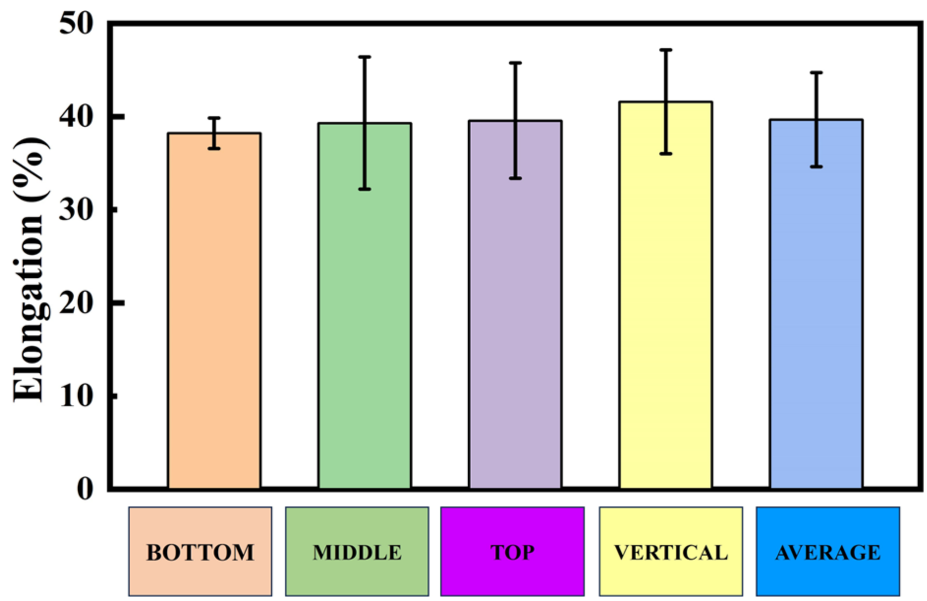

Fig. 3.21: Elongation of the sample at different Regions

As seen in Figs. 3.19 & 3.20, the specimen from the bottom section has a higher UTS and YS than the top and middle parts; however, there is no such drastic change in the sample's elongation at different regions as shown in Fig. 3.21. This is due to the fact that the tensile properties are influenced by the heat dissipation conditions of the top, middle, and bottom layers. The YS is 88.46 MPa, the EL is 41.59%, and the longitudinal UTS is 251.72 MPa. Because of potential pores and cracks between the layers that could negatively affect the tensile properties, the longitudinal tensile samples' strength is lower than that of the transverse samples [53]. Another reason behind the less tensile strength in Longitudinal direction is due to insufficient penetration [52]. The results of the tensile test indicate that the parts manufactured by WAAM with 5356 aluminium magnesium alloy perform better than those made with the alloy as cast. Gao et al. report that the as-cast 5356 aluminium alloy's UTS is 202.4 MPa, YS is 87.2 MPa, and EL is 23.8% [54]. The average UTS and YS of the parts produced by WAAM are higher by 27.17% and 37.8%, respectively, than the aluminium alloy as cast. As seen in Figs. 3.19 to 3.21, the longitudinal and transverse tensile properties exhibit clear isotropic characteristics. There is minimal strength variation between the top, middle, and bottom regions of the wall, making it simple to demonstrate isotropy. This is because the 5356 aluminium alloy does not require heat treatment, and the thermal cycle from the reheating of the higher layers almost cannot bring reinforcement to the lower layers. As of right now, the yield and tensile strengths of the obtained 5356 aluminium alloys are higher than those of the earlier research.

3.9 Fracture Morphology Analysis of Tensile Sample

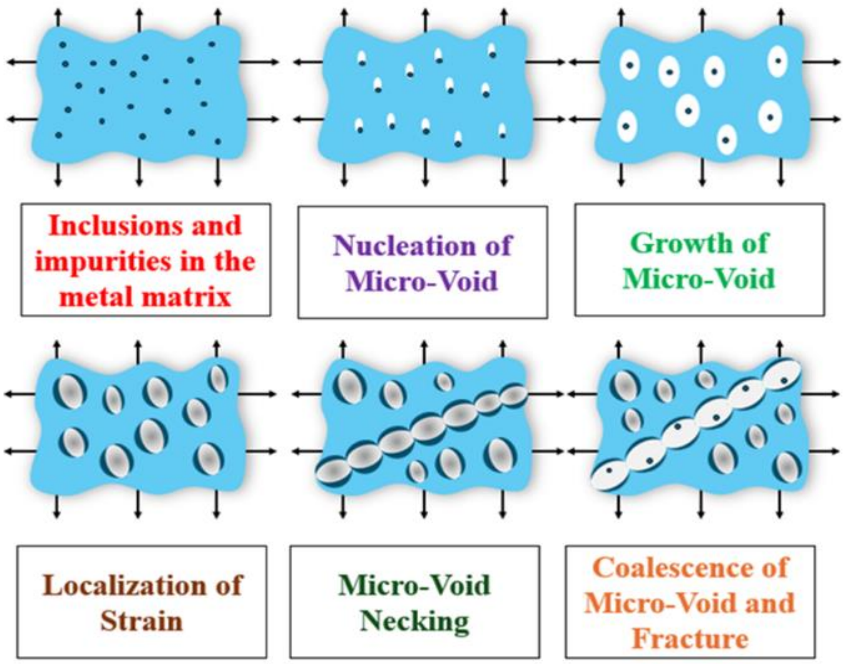

Fig. 3.22: Dimple Fracture Mechanism

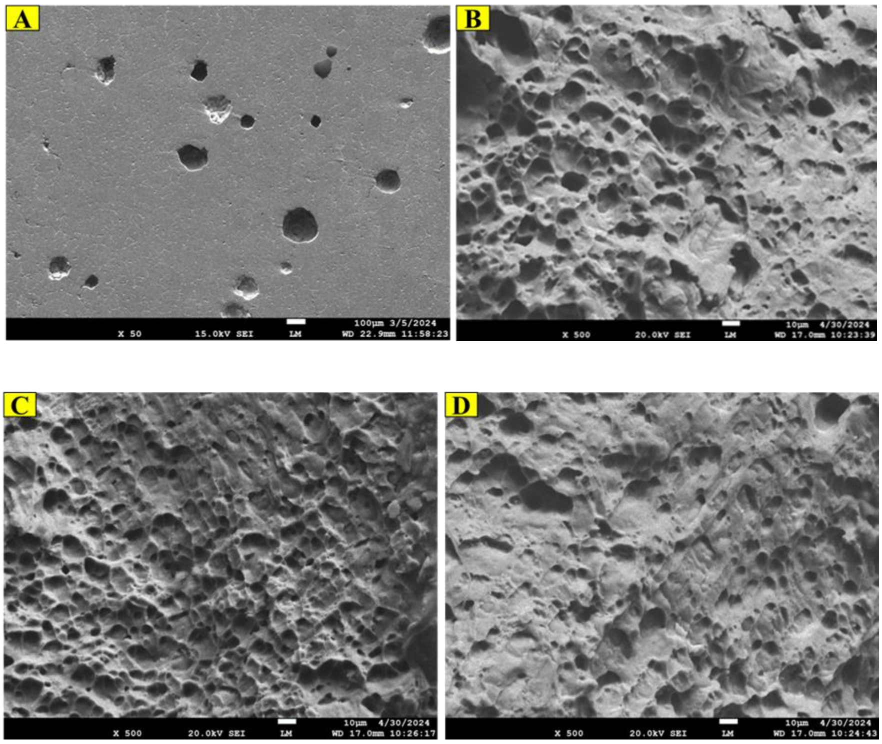

Fig. 3.23: Fractography of the tensile sample

As shown in the Fig. 3.22 & Fig. 3.23 it can be understood that the fracture morphology of the WAAM sample is a typical dimple fracture. The presence of micro-voids as shown in the Fig. 3.23 (A) in the WAAM deposited sample is mainly by uneven heat accumulation and uneven and scattered heat dissipation in different regions. The primary mechanism of ductile dimple fracture in metallic materials is the nucleation, growth, and coalescence of micro-voids [55]. A void is created when localised plastic strain develops under the influence of tensile hydrostatic stresses. It can originate from an inclusion or second phase particle by decohesion or cracking. When two adjacent voids are too close together, the voids start to merge, which causes the material to crack and fracture further [56]. Dimples develop as a result of micro-void coalescence during yielding, which occurs when micro-voids are formed close to certain impurities like inclusions and second phase particles [56]. In the fibrous zone, equiaxed dimples are found as shown in the Fig. 3.23 (C), however in the shear lip zone the elongated dimples are found as shown in the Fig. 3.23 (D). The figures also suggest that the voids nucleate at larger particles first, growth of these voids occurs due to the strain localization between the voids. The secondary voids, which are more strongly bonded particles requiring higher strains for void nucleation, can nucleate between these primary voids.

3.10 Fretting Wear and Co-efficient of friction Analysis at Optimal Condition

The analysis on fretting wear and co-efficient of friction (COF) of WAAM deposited Al alloy parts produced at optimal parametric settings has been performed and discussed in the subsequent sections.

3.10.1 Fretting COF analysis

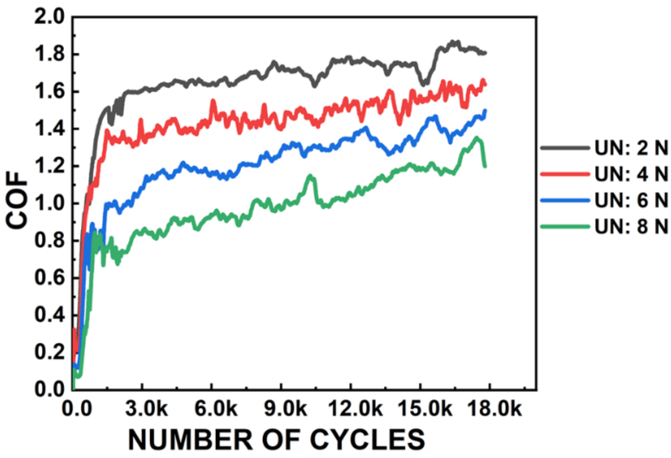

Fig. 3.24: Fretting COF vs No. of cycles at different loads

The Fig. 3.24 represents the change of the COF of the additively manufactured Al alloy under different loads. The thin contaminant film that was present at the surface during the initial stages of the test is observed to have self-absorbed and inevitably polluted, resulting in low COF values. The removal of the thin oxide layer and the creation and buildup of a large amount of debris in the contact area during the truncation of surface asperities may be the causes of the variations in the COF [35]. Then, because of the real metal-to-metal contact during the run-in stage, the COF increases significantly. Additionally, as the number of cycles increased, the contact between the mating parts changed from being between the asperity to being on the surface, which raised the COF [33]. It is also noted that with an increase in the load from 2 N to 8 N, there was a steady decrease in COF. As the load increases, the contact condition between the surfaces gradually shifts from gross slip to partial slip and eventually near stick slip [33], [35], [37]. Initially, at lower loads, there is significant relative motion between the surfaces, leading to a gross slip condition. As the load increases, the contact becomes more complex, resulting in partial slip where some areas of the surfaces are in contact while others experience slip. At higher loads, heat is generated at the contact points due to increased friction. This heat promotes the formation of a tribolayer, which is a layer of material that forms on the surface due to frictional interaction [33]. This tribolayer, associated with dry wear, provides lubrication and protection against wear. Initially, under low normal loads, the tribolayer coverage area is weak. However, as the load increases, the formation and coverage of the tribolayer improve. This enhanced tribolayer formation results in lower COF values and reduced wear rates because it provides better lubrication and protection against surface damage [57]. It was demonstrated by R.D. Mindlin that the friction coefficient and normal load have a proportionate relationship with the transition from gross slip to stick-slip [58].

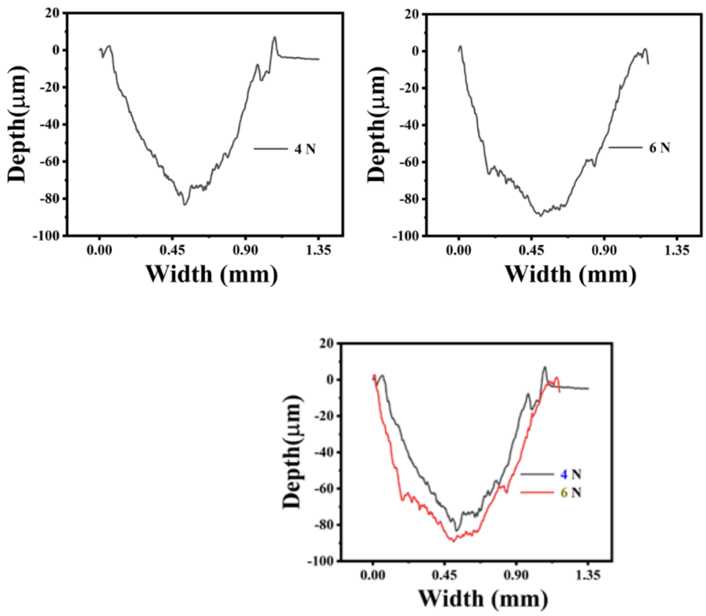

Fig. 3.25: Wear Track Profile at different loads

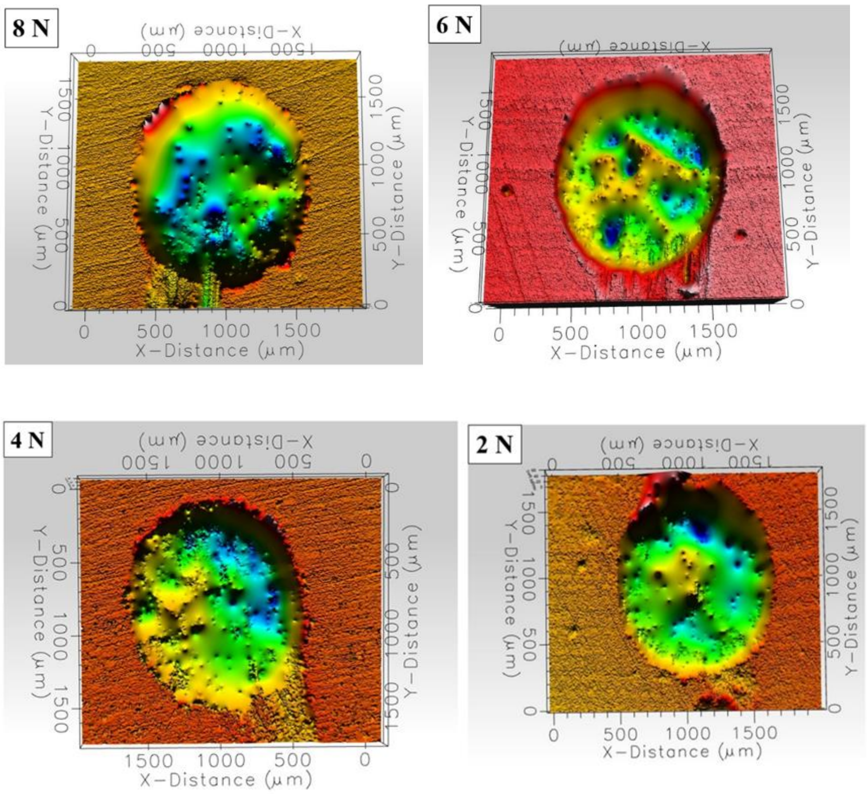

Fig. 3.26: Optical Profilometry of the wear scar at different loads

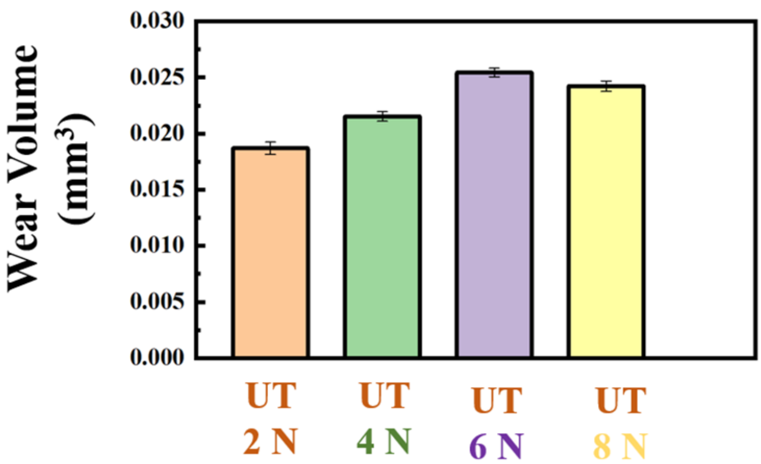

Fig. 3.27: Wear Volume at different loads

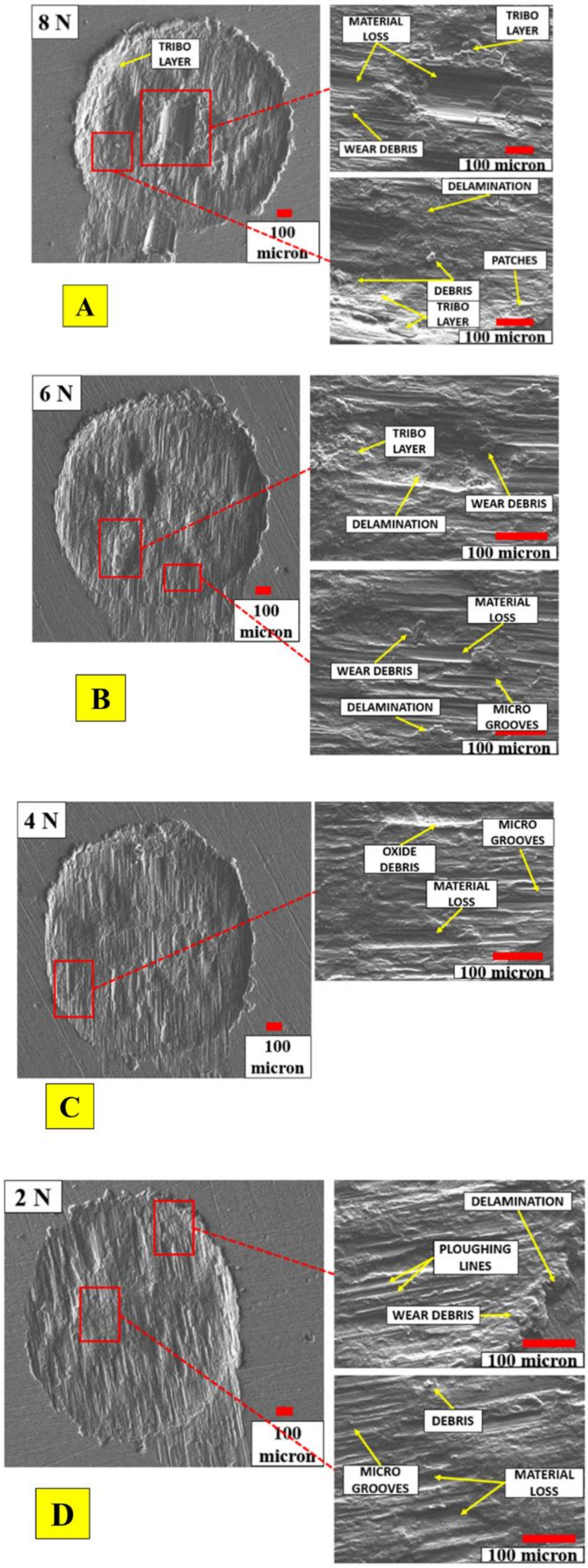

Fig. 3.28: SEM images of the wear scar at different loads

(A, B, C, D)

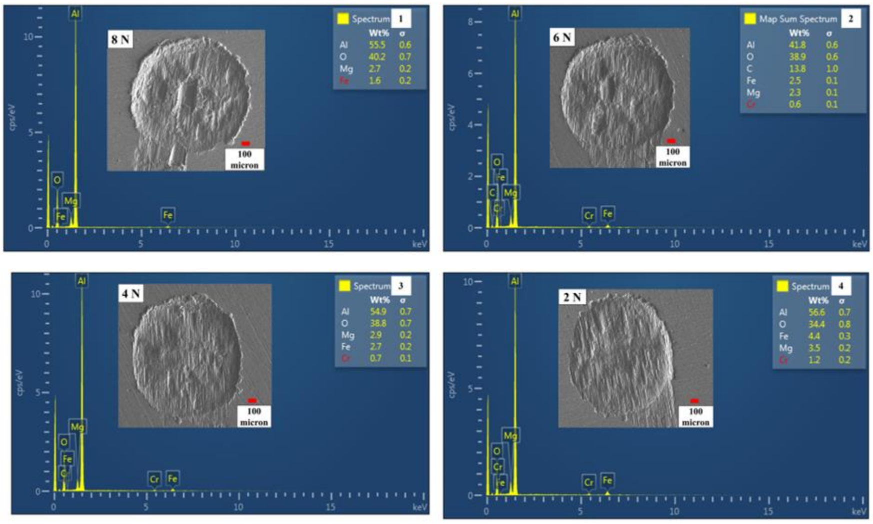

Fig. 3.29: EDS of the wear scar at different loads

3.10.2 Fretting wear volume analysis

The wear track profile of the wear scar at 4 N and 6 N is shown in the Fig. 3.25. It is observed that these two profiles represent the "V" which suggests severe damage at the central point that was also confirmed due to the presence of micro grooves, micro-cavities and pits as observed in the Fig. 3.23 (A). It is also observed that the with increase in load the wear track depth increases which is also attributed with the increase in wear volume with increase in load. The variation of the fretting volume with respect to the normal load is shown in the Fig 3.27. It is observed that the wear volume is increased with increase in load from 2 N to 6 N. This behavior is expected, as higher loads typically result in more severe wear due to increased contact pressure and energy dissipation. However, with increase in load beyond the threshold value of 6 N there is a decrease in the wear volume and this unexpected behavior is attributed to discrepancies in the actual area of contact during the test cycle. The area of contact between the surfaces is directly proportional to the applied normal force up to the threshold load value. Therefore, up to this point, the increase in wear volume is consistent with the increase in contact area. Beyond the threshold load value, the transition from gross slip to partial or stick-slip occurs at the fretting contact area. This transition alters the fretting area and leads to changes in wear behavior. A similar kind of trend is observed by Gaspar et al. on galvanized steel for fretting wear volume with constant slip amplitude with varying the normal loads [59]. Rasshmi et al. also observed the decreasing trend of wear volume with increase in normal load for the fretting wear volume of LPBF processed AlSi10Mg alloy for different heat treatment conditions. Therefore, the results obtained from the current study are further justified [60]. As shown in the Fig. 3.28 the wear formation mechanism is primarily a mixture of adhesive, abrasive and oxidative wear. The wear scar morphology as shown in the Fig. 3.28 (B, C, D) is covered with grooves, ploughing lines along the fretting direction as well as wear debris, material loss and delamination. The micro groves and the ploughing lines that were appeared is mainly due to abrasion caused by the wear debris that was generated during the test cycle. Fig. 3.28 (C, D) shows the appearance of large grooves along the fretting direction. It demonstrates that the specimen surface got abraded by the debris particles that were generated during the test cycle, and this also explains the mechanism of third body abrasion. As shown in the Fig. 3.28, the wear debris are squeezed and oxidized during the fretting operation and large amount of abrasive debris accumulate at the edges. From the EDS result as shown in Fig. 3.29, it is understood that the materials (Fe, Cr,) removed from the counterface got adhered to the specimen because of the frictional heat generated during the test cycle. This denotes the features of adhesive wear. It also explains the phenomenon of the transition between gross slip and mixed fretting regime. The elemental composition of worn sample at higher load (8 N) as shown in the Fig. 3.29, it shows the presence of higher concentration of O on the worn surface which indicates the severe oxidation of the specimen. Due to the oxidation, there is a formation of a stable, hard, adherent oxide layer which is also shown in the Fig. 3.29. Due to this stable hard oxide layer there is reduction in the wear volume as shown in the Fig. 3.27. The composition of the oxide layer would be primarily Al and O, as confirmed through the elemental map. The oxide layer should be Al_2O_3.

3.11 Summary

The parametric investigation of the process variables on WAAM of aluminium alloy reveals that the process variables such as standoff distance, power voltage, cooling time and feed rate had a significant effect on wall width and microhardness. Moreover, the mathematical model developed also provides fruitful results. The outcomes of the present research are highlighted as follows:

i) Increase in standoff distance and voltage increases the oxidation at the surface of deposited aluminium alloys.

ii) Increase in cooling time and feed rate provide uniformity of the deposited aluminium alloys with corresponding increase in wall width and micro hardness.

iii) Based on one factor at a time (OFAT) experimentation, it is observed that feed rate of 5 m/min, voltage of 14 V, cooling time of 15 sec, and standoff distance of 14 mm provide better results in terms of wall width, micro hardness and uniformity over the entire deposited aluminium alloys.

iv) From the optimization analysis on the wall width, it is predicted that feed rate of 4 m/min, power voltage of 13 V, and cooling time of 25 sec provide minimum wall width.

v) From the optimization analysis of the micro-hardness it is predicted that feed rate of 6 m/min, power voltage of 13 V, and cooling time of 25 s provide maximum micro-hardness.

vi) The multiple objective optimizations result of the responses shows that feed rate of 4.5 m/min, power voltage of 13 V, cooling time of 25 s provide optimum results.

vii) Microstructural analysis of the WAAM deposited sample shows that there is a transition of finer grains to courser grains from the bottom region to top region as the rate of heat dissipation is faster in the bottom region and the rate of heat dissipation is lower in the middle region as the middle region is sandwiched between the top and bottom layers.

viii) The WAAM deposited sample results into higher hardness than the substrate due to from rapid solidification, multiple thermal cycles and induced residual stresses, with the bottom region showing the highest hardness due to finer grains and better heat dissipation.

ix) The tensile properties of the Wire arc additively manufactured 5356 aluminium alloy varies across the section, with the bottom transverse section exhibiting higher ultimate tensile stress (UTS) and yield stress (YS) compared to the top and middle sections due to variations in heat dissipation conditions among layers.

x) Longitudinal tensile samples demonstrate lower strength than transverse samples, potentially attributed to the presence of pores, cracks, and insufficient penetration between layers, impacting the tensile properties negatively.

xi) Compared to the as cast aluminium alloy, the average UTS and YS of the parts made by the WAAM are increased by 27.17% and 37.8%, respectively.

xii) Fractography of the tensile sample shows that the fracture mechanism is dimple fracture. In the fibrous zone equiaxed dimples are found but in slip zone the elongated dimples are found.

xiii) Tribological studies on WAAM deposited sample reveals that with increase in load the COF decreases and with increase in load the fretting wear volume increases, however after a threshold limit of 6 N, fretting wear volume decreases due to formation of stable, hard, adherent oxide tribofilm which enhances the wear resistance. The study of wear scar indicates that the wear mechanism is a combination of oxidative, adhesive and abrasive wear. The wear track profile resembles “V” shape which indicated that the wear is predominant at the centre.

Chapter 4

Experimental Investigation into Laser Nitriding of Wire Arc Additively Manufactured Part of Aluminium Alloy for Enhancing the Mechanical and Tribological Properties.

In this chapter the parametric optimization of the laser nitriding process parameters has been included and it's effects on the output responses like Micro-Hardness of the laser nitrided WAAM deposited Al alloy have been analysed. The mechanical and tribological performance of the laser nitrided WAAM deposited Al part at the optimal parametric condition have been discussed and also the effects of laser nitriding process on the contact angle of the produced surface have been included

4.1 Experimental plan of the laser nitriding process

Based on the literature [37], [39], [40], [41], [61], it was found that the main process parameters of the laser nitriding were N_2 gas flow rate, laser fluence, overlapping percentage and laser wavelength etc. However, the study of combined effects of all the process parameters on the output responses are lacking in the literature. In this present study the combined effects of the laser nitriding process parameters are studied on output response like Micro-Hardness with the help of Box Behnken design of experiments. The process variables and their levels which are selected for the experiments are represented by the Table 4.1.

Table 4.1: Laser Nitriding Process variables and their levels

Process Variables	Units	Levels		
N_2 Gas Flow Rate	l/min	6	15	24
Laser Fluence	J/cm^2	60	120	180
Overlapping Percentage	%	80	85	90

Nd^{3+}:YAG laser is used with 532 nm wavelength , 9ns pulse duration, 18cm stand of distance and 10Hz pulse frequency. The reason of choosing the 532 nm wavelength is due to low reflectivity and high absorptivity of the material as shown in the Fig. 4.1.

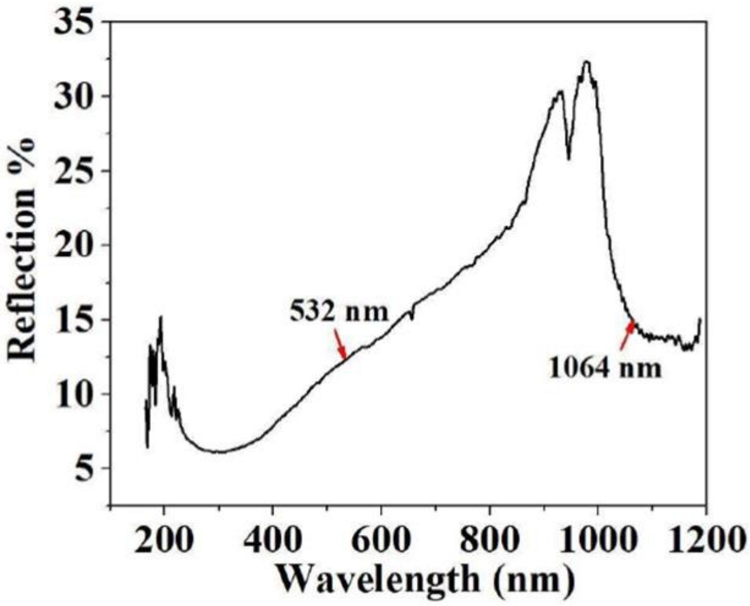

Fig. 4.1: UV VI Spectrum of the base material [37]

The overlapping percentage was calculated with the help of the following formulae.

% Overlapping = $(1 - s/f) \times 100$ **Eq. (4.1)**

Where, s= scanning speed (mm/sec) and f= frequency

The experimental plan is based on the Box Behnken design of experiments which is represented by the Table 4.2.

Table 4.2 Experimental plan based on Box Behnken design of experiments

Sl. No.	N_2 Gas Flow Rate (l/min)	Laser Fluence (J/cm^2)	Overlapping Percentage (%)	Average Micro-Hardness (HV)
1	6	60	85	111.6671
2	24	60	85	119.5321
3	6	180	85	116.3846
4	24	180	85	107.3729
5	6	120	80	110.9396
6	24	120	80	102.6412
7	6	120	90	103.5421
8	24	120	90	110.5238
9	15	60	80	113.4767
10	15	180	80	104.3725
11	15	60	90	108.9508
12	15	180	90	110.5433
13	15	120	85	113.3583
14	15	120	85	113.6783
15	15	120	85	113.7683

4.2 Development of Mathematical Modelling of the Responses based on Box Behnken Design

The experiments thus carried based on the Box Behnken design of experiments also provide the relation between process variables and the responses undertaken.

$$\boldsymbol{Micro-Hardness}\ (\boldsymbol{HV}) = 113.602 - 0.3079x - 1.8692y + 0.2662z - 1.143x^2 + 1.281y^2 - 5.547z^2 - 4.219xy + 3.820xz + 2.674yz \quad \textbf{Eq. (4.2)}$$

where,

x= N_2 Gas Flow Rate (l/min), y= Laser Fluence (J/cm^2),

z= Overlapping Percentage (%)

The above empirical relations thus obtained using MINITAB software were further checked based on F-ratio and p value for the accuracy of the developed mathematical models for wall width and micro hardness. The ANOVA results of micro-hardness are shown in Table 4.3.

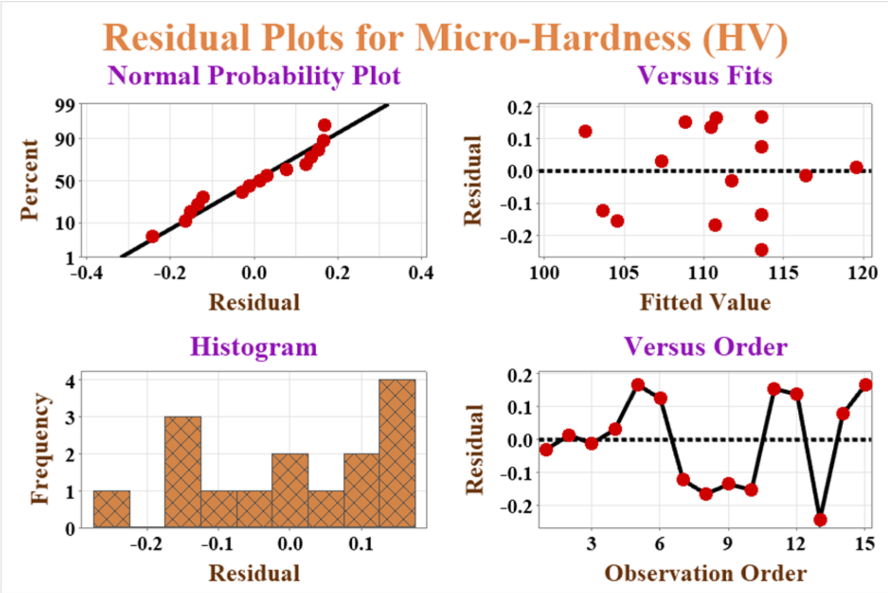

Fig. 4.2: Residual Plots for Micro Hardness

Table 4.3: Analysis of Variance of Micro-Hardness

Source	DF	Adj SS	Adj MS	F-Value	P-Value
Model	9	314.506	34.945	658.62	0.000
Linear	3	29.276	9.759	183.92	0.000
Square	3	127.051	42.350	798.18	0.000
2-Way Interaction	3	158.180	52.727	993.75	0.000
Error	5	0.265	0.053		
Lack-of-Fit	3	0.172	0.057	1.24	0.476
Pure Error	2	0.093	0.046		
Total	14	314.772			

As per Table 4.3, it is seen that p-value for Linear, Square and 2 Way interaction of the process variables of regression model are lower than 0.05 which means that these are significant. The Lack of Fit computed F value for wall width was found to be 1.24 and its p value is 0.476 which is higher than 0.05. Thus, the lack of fit is insignificant and the fit can be considered significant. The calculated value of R-Sq = 99.92 %, R-Sq (adj) =99.76 %, and R- sq (pred) = 99.06 % which is sufficiently high. As a result, the created models fit the observed data well. Fig. 4.2 show the residual plots for microhardness. The discrepancies between the response values predicted by the model and the observed response values at each factorial value combination are known as residuals. They support the assessment of the model's suitability for the response that is currently being chosen. The data is well-fit for the model, as indicated by the residual probability plot of Figure 4.2, which displays all of the points falling on the line with minimal scatter. This suggests that the residuals follow a normal distribution. The residuals are plotted against the fitted, or predicted, values of the chosen response in the Residual vs. Fitted plot of Figure 4.2. A good fit of the model is indicated by the fact that the number of points with positive residuals above the dotted line equals the number of points with negative residuals below the dotted line, indicating equality in variance between the data. The data is shown to follow a normal distribution in Fig. 4.2's Residual Histogram plot. The residuals are plotted against the order of runs that were used in the design in the Residual vs. Order plots of Figure 4.2. The experiment's test sequence has no effect and the data points are independent of one another because the points are dispersed randomly throughout the plot and no specific pattern is visible.

4.3 Parametric influences of N_2 Gas Flow Rate, Laser Fluence, Overlapping Percentage on Micro-Hardness

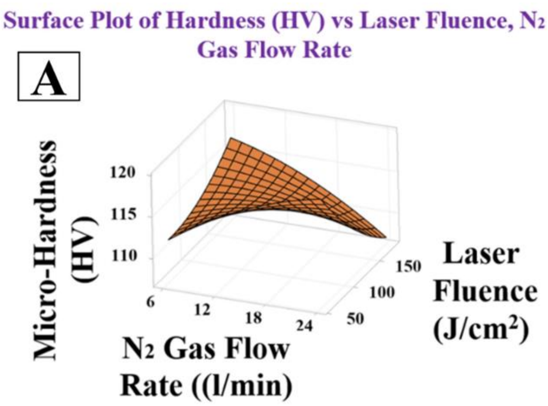

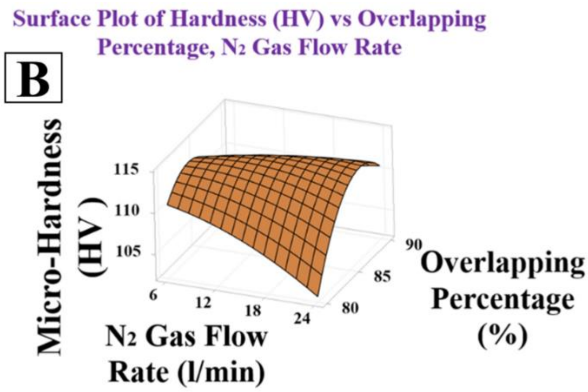

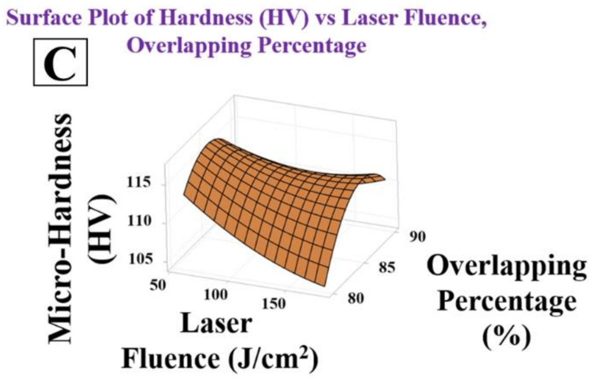

Fig. 4.3: Surface plots of Micro Hardness with respect to (A) Laser Fluence and N_2 gas flow rate, (B) Overlapping Percentage and N_2 gas flow rate and (C) Laser Fluence and Overlapping Percentage

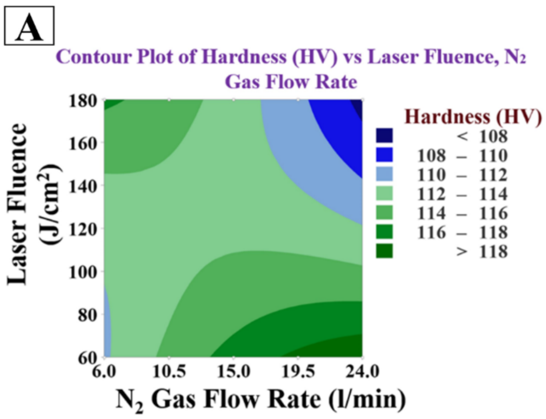

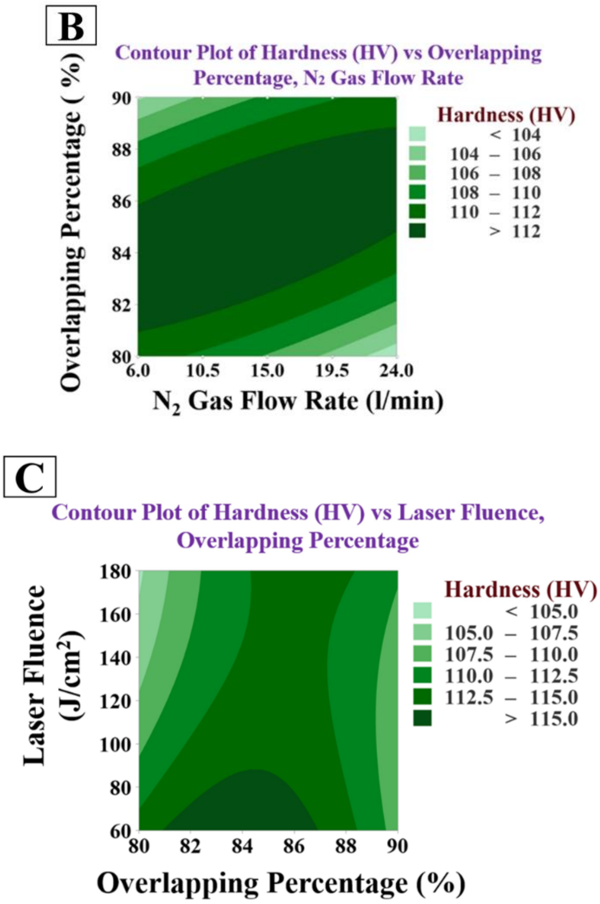

Fig. 4.4: Contour plots of Micro Hardness with respect to (A) Laser Fluence and N_2 gas flow rate, (B) Overlapping Percentage and N_2 gas flow rate and (C) Laser Fluence and Overlapping Percentage

Fig. 4.3 (A) and Fig. 4.4 (A) show the effects of Laser Fluence and N_2 gas flow rate on micro hardness when overlapping percentage was held constant. It was observed that as the N_2 gas flow rate increases there is an increase in the micro-hardness. However, with increase in the laser fluence the micro-hardness is decreasing. This is mainly because as the N_2 gas flow rate increases, more nitrogen is available for diffusion into the aluminium surface. This leads to the formation of a thicker and more continuous layer of aluminium nitride (AlN), which is a hard compound, thereby increasing the micro-hardness. At lower laser fluence levels, the energy provided by the laser is sufficient to enhance the diffusion of nitrogen into the aluminium surface and promote the formation of a hard nitride layer without causing excessive melting or thermal damage. As the laser fluence continues to increase beyond an optimal point, the excessive energy can cause overheating, leading to the formation of defects such as cracks, voids, or even re-melting and re-solidification of the nitride layer. These defects can weaken the nitrided layer, reducing its hardness which is also observed as shown in Fig. 4.3 (C) and Fig. 4.4 (C). Fig. 4.3 (B) and Fig. 4.4 (B) show the effects of overlapping percentage and N_2 gas flow rate on micro hardness when laser fluence was held constant. At moderate levels of overlapping percentage, the laser coverage is more uniform, ensuring that each area receives sufficient laser exposure to form a consistent and well-distributed nitride layer. This improves the overall hardness of the surface. Fig. 4.3 (C) and Fig. 4.4 (C) show the effect of laser fluence and overlapping percentage on micro hardness when N_2 gas flow rate was held constant. It was observed that with increase in laser fluence there was a decrease in micro-hardness but micro-hardness increases with the overlapping percentage because as the overlapping percentage continues to increase beyond an optimal point, the material experiences excessive heating due to repeated laser passes. This can cause re-melting and dilution of the nitride layer, reducing its micro-hardness.

4.4 Optimization based on the Box Behnken Design of Experiments

Based on the proposed mathematical models, the analysis of every individual response has been done in order to achieve the maximum micro hardness. The upper limit of desirability function (D) is supposed to have a weight value of 1 for optimum value of the responses. For laser nitriding of WAAM deposited aluminium alloy part, the software MINITAB was used to optimize the responses using desirability function analysis. Each column of the optimization graph that is subsequently obtained corresponds to a factor. The graph's rows each represent a response. While all other parameters are fixed, each graph cell illustrates how one response varies as a function of one of the process variables. The experimental design's high and low settings are shown by numbers at the top of each column, while the row coloured in red denotes the present values of the process variables that should be used to achieve the goals. Response goal, desired value, current y factor, and desirability value are provided to the left of each row.

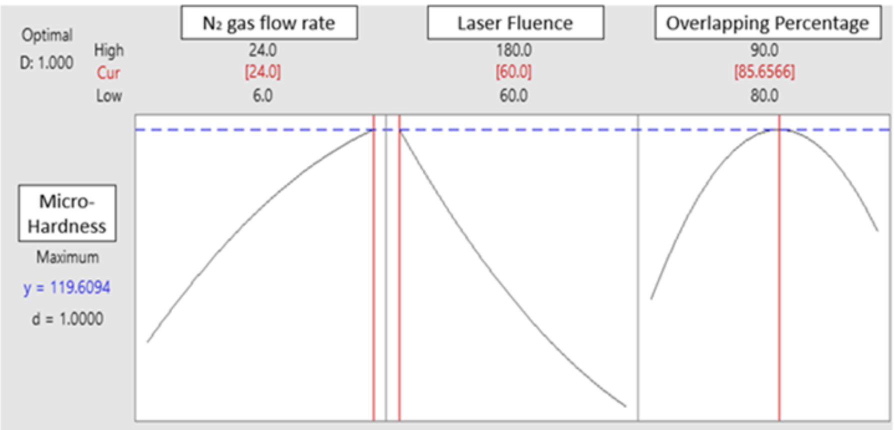

Fig. 4.5: Optimization plot for micro hardness

Fig. 4.5 show the findings of single-objective optimization of the responses. It was observed from Fig. 4.5 that the optimal process variables settings required for achieving maximum micro hardness, N_2 gas flow rate of 24 l/min, laser fluence of 60 J/cm^2, and 85 % overlapping percentage should be used. Experiments are performed at optimal parametric settings in order to observe the error produced while performing experiment.

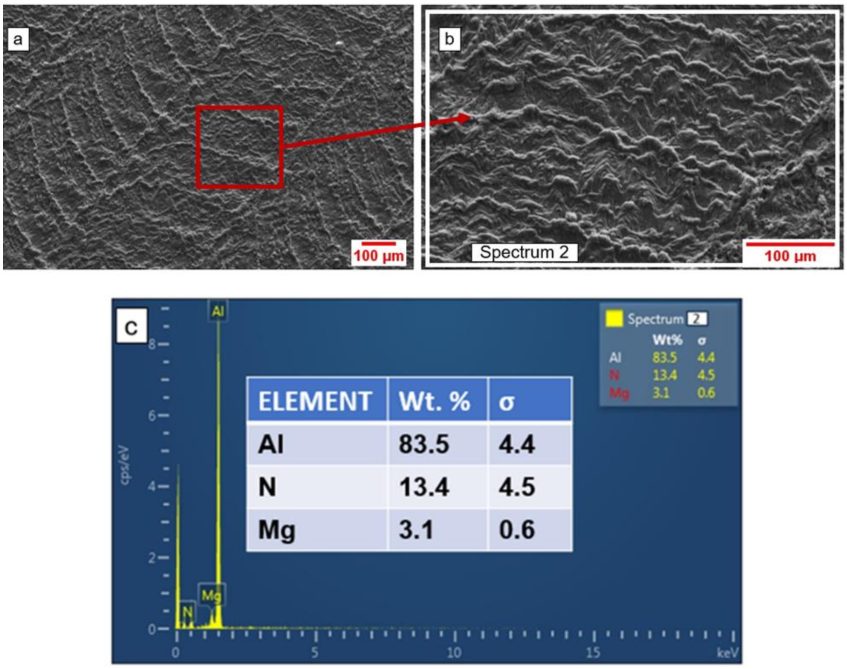

Fig. 4.6: (a), (b) SEM images of laser nitride surface and (c) EDS of laser nitride surface

After carrying out experiment at optimal process variables settings, it was observed that actual value of micro-hardness was obtained as 114.89 HV. The average micro-hardness obtained of the WAAM sample is 73.2 HV. Hence after laser nitriding there is an increase of 56.95 % of micro-hardness. The results were further utilized to predict the error in percentage using equation 4.3.

$$\text{Error (\%)} = \frac{\text{Predicted Value - Actual Value}}{\text{Predicted Value}} \times 100 \qquad \textbf{Eq. (4.3)}$$

Upon analysis, it was observed that the percentage of prediction error of micro-hardness was 3.94 % which is less than 5 %. Thus, above designed mathematical modelling is suitable for laser nitriding. The SEM images of laser nitride surface are shown in Fig.4.6 (a) and (b). The presence of nitrogen over the surface was confirmed by the EDS analysis as shown in the Fig. 4.6 (c). The average micro-hardness obtained of the WAAM deposited sample is 73.2 HV. Hence after laser nitriding there is an increase of 56.95 % of micro-hardness. Based on the optimal parametric setting, further laser nitriding was carried and different tribo-mechanical tests like fretting wear, corrosion and contact angle measurement were carried to investigate the effects of laser nitriding.

4.5 Impact of Laser Nitriding over contact angle

As shown in the Fig. 4.7 (a, b, c) and Fig. 4.8 (a,b,c) it can be seen that after laser nitriding, there is an increase in the contact angle from 72.23^0 to 107.86^0 for the left contact angle and from 67.33^0 to 114.64^0 for the right contact angle, making the surface hydrophobic from hydrophilic. Since the laser treated surface consists of micro texture with various heights that can trap air pockets resulting into reduction of the contact area with water droplets and thus making the surface hydrophobic [62]. After laser nitriding, there is a formation of protective nitride layer which acts as a barrier to water penetration, thus making the surface hydrophobic [63]. The contact angle was examined for both the distilled after and the salt water solution (water mixed with NaCl salt). It was

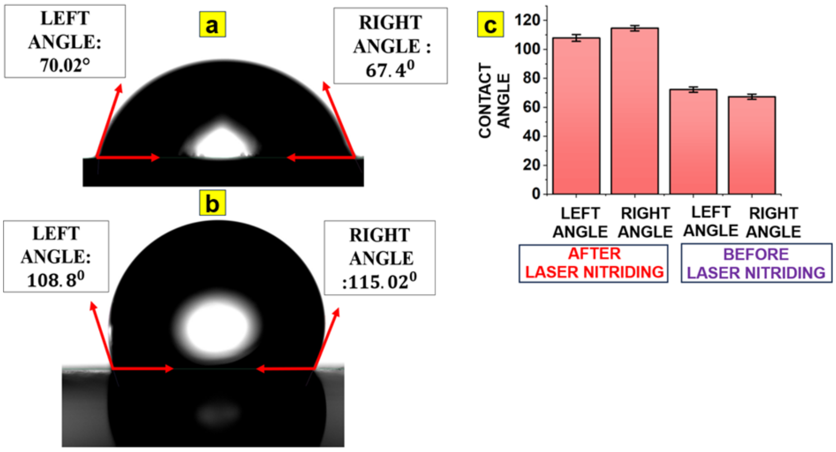

Fig. 4.7: Contact Angle variation of untreated and laser nitride surface using water as the contacting liquid

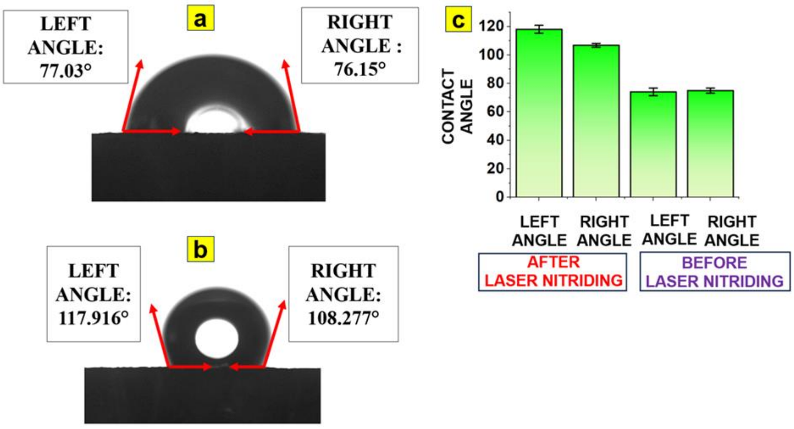

Fig. 4.8: Contact Angle variation of untreated and laser nitride surface using salt water (mixed water and NaCl salt) as the contacting liquid

observed that with salt water solution also the contact angle increases for the laser nitrided surface thus making the surface hydrophobic. However, it was further noticed that in comparison to the distilled water, with the salt water, the contact angle is slightly more as shown in the Fig. 4.8. This is mainly due to the change in the properties of the liquid due to the incorporation of the salt solution. Saltwater typically has a higher surface tension than distilled water due to the presence of dissolved ions which tends to increase the contact angle. Hydrophobic surface will repel water which will reduce the adhesion of the marine organisms like algae, barnacles thus reducing the biofouling. This reduction in fouling can help maintain the efficiency and performance of the marine components like impeller, propeller, hulls and rudders etc. by minimizing drag and maintaining smooth operation.

4.6 Impact of Laser Nitriding over Co-efficient of Friction and Fretting wear

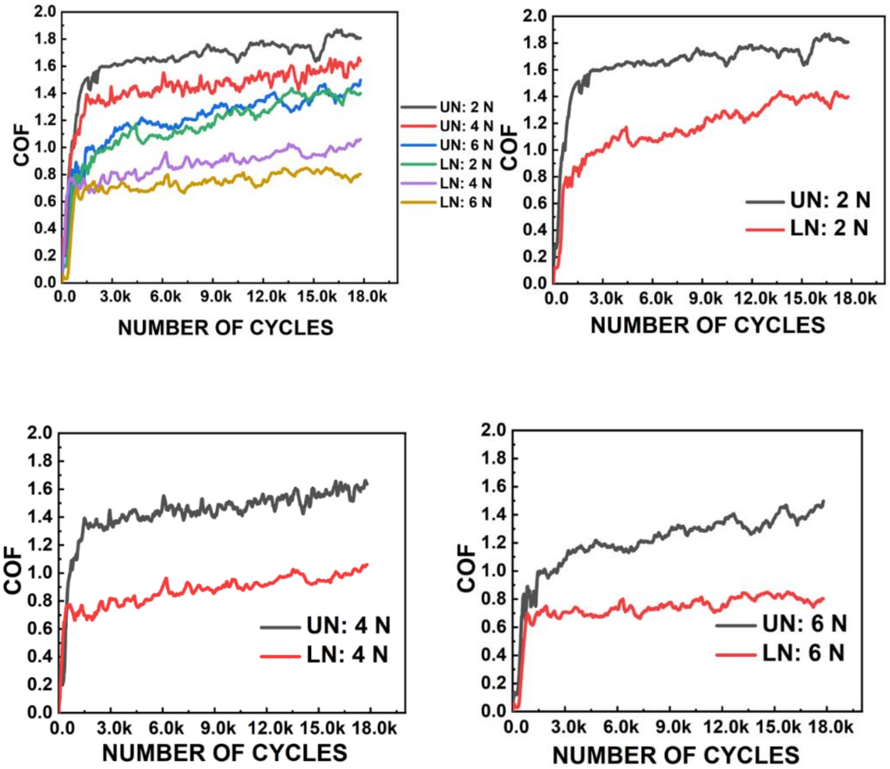

Fig. 4.9: Co-efficient of friction vs No. of Cycles with three different loads 2 N, 4 N, 6 N (UN: Untreated WAAM sample, LN: Laser nitrided WAAM sample)

From the Fig. 4.9 it can be observed that the laser nitrided surface shows lesser co-efficient of friction (COF) values in compare to the untreated WAAM deposited sample. This is mainly due to the formation of self-lubricating AlN over the laser nitride surface which can be confirmed by the presence of nitrogen in the EDS analysis as shown in the Fig. 4.6 (c). The thin contaminant film that was present at the surface during the initial stages of the test is observed to have self-absorbed and inevitably polluted, resulting in low COF values. Then, because of the real metal-to-metal contact during the run-in stage, the COF increases significantly. Furthermore, as the number of cycles increased, the contact between the mating parts changed from being between the asperity to being on the surface, which raised the COF. Because of the debris that was generated and contributed to bearing the contact load, COF decreases after reaching its peak value. It is also noted that with an increase in the load, there was a steady increase in COF as the area of contact is directly proportional to the applied normal load. However, as the load increases, the contact condition between the surfaces gradually shifts from gross slip to partial slip and eventually near stick–slip. Initially, at lower loads, there is significant relative motion between the surfaces, leading to a gross slip condition. As the load increases, the contact becomes more complex, resulting in partial slip where some areas of the surfaces are in contact while others experience slip. As the load increases, the contact becomes more complex, resulting in partial slip where some areas of the surfaces are in contact while others experience slip. At higher loads, heat is generated at the contact points due to increased friction. This heat promotes the formation of a tribolayer, which is a layer of material that forms on the surface due to frictional interaction. This tribolayer, associated with dry wear, provides lubrication and protection against wear. Initially, under low normal loads, the tribolayer coverage area is weak. However, as the load increases, the formation and coverage of the tribolayer improve. This enhanced tribolayer formation results in lower COF values and reduced wear rates because it provides better lubrication and protection against surface damage.

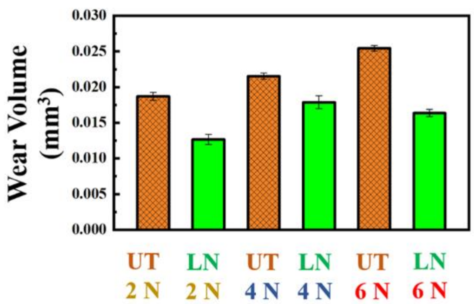

Fig. 4.10: Wear Volume of untreated (UT) and laser nitrided (LN) sample at different loads

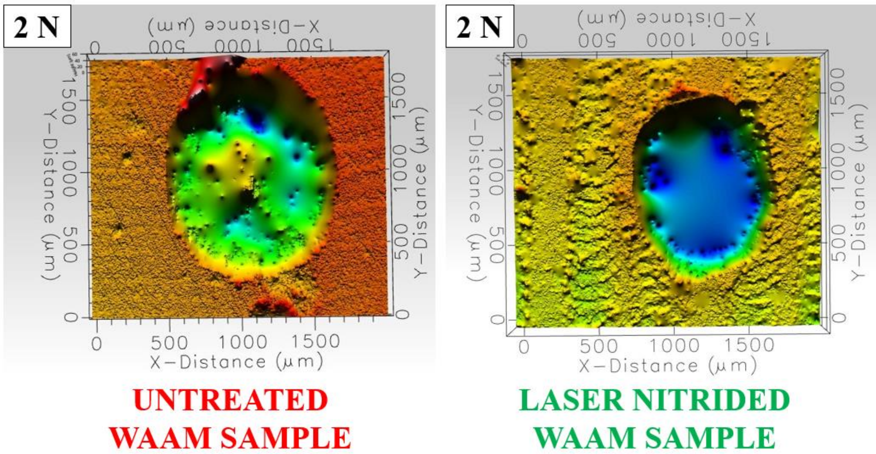

Fig. 4.11: Optical Profilometry of the wear scar of untreated and laser nitrided sample

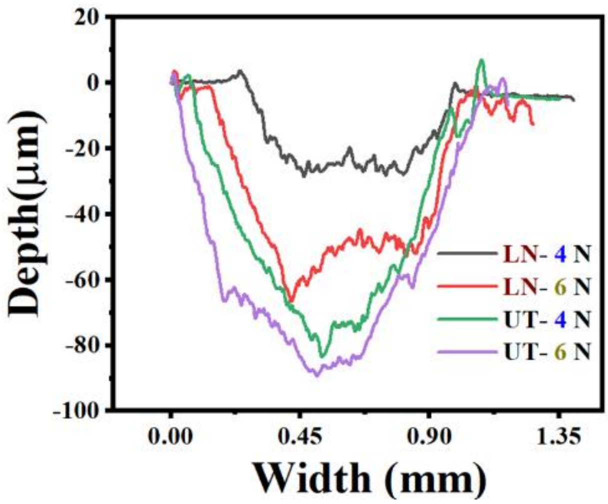

Fig. 4.12: Wear Track Profile of untreated (UT) and laser nitrided (LN) sample at different loads

Fig. 4.11 represents the wear scar of untreated WAAM specimen and the laser nitrided specimen which is used to calculate the wear volume. As shown in Fig. 4.10 the laser nitrided WAAM sample shows less wear volume in compare to the untreated WAAM sample due to the formation of much harder aluminium nitride. With increase in load, as the contact area increases there is an increase in the wear volume. However, after attaining a threshold value, there is a decrease in the wear volume due to the formation of hard, adherent oxide film. In order to analyse the depth of penetration following wear damage and comprehend the wear mechanism during the FW test, 2D contact type profilometry was employed. The wear track profiles for the UT and LN specimens across the fretting direction are shown in Fig. 4.12. It is observed that the laser nitride specimen has lower depth of wear which is also confirmed by the lower wear volume of the laser nitride specimen.

4.7 Summary

The parametric investigation of the process variables on laser nitriding of WAAM deposited aluminium alloy reveals that the process variables such as N_2 gas flow rate, laser fluence, and overlapping percentage had a significant effect on the surface microhardness. Moreover, the mathematical model developed also provides fruitful results. The outcomes of the present research work are highlighted as follows:

i) Increase in N_2 gas flow rate and decrease in laser fluence increase the micro hardness. However, increase in the overlapping percentage increase the micro-hardness but very high overlapping percentage reduces the micro-hardness.

ii) From the optimization analysis of the micro-hardness it is predicted that N_2 gas flow rate of 24 l/min, laser fluence of 60 J/cm^2, and 85 % overlapping percentage provide maximum micro-hardness.

iii) After carrying out experiment at optimal process variables settings, it is observed that actual value of micro-hardness is obtained as 114.89 HV and the average micro-hardness obtained of the WAAM deposited sample is 73.2 HV. Hence after laser nitriding there is an increase of 56.95 % of micro-hardness.

iv) It is observed that the laser nitriding increases the contact angle with distilled water from 72.23^0 to 107.86^0 for the left contact angle and from 67.33^0 to 114.64^0 for the right contact angle, making the surface hydrophobic from hydrophilic due to the formation of micro-textures and cavities and the formation of the AlN layer which acts as a barrier to water penetration. It was observed that with salt water solution also the contact angle increases for the laser nitrided surface.

v) It is observed that due to the formation of self-lubricating AlN reduces the COF of the laser nitride surface. A lower COF is favorable for marine applications due to lower wear, lower drag and increased efficiency of the marine components.

vi) It is observed that the laser nitrided surface has lower depth of wear in compare to the WAAM deposited sample. The wear volume of the laser nitrided surface also drastically reduced due to the formation of the hard aluminium nitride over the surface.

Chapter 5

Conclusions and Future scope of work

5.1 Conclusions

Based on the experimental results, parametric analysis and mechanical and tribological studies on WAAM of Aluminium 5356 alloy part and it's post processing by Laser Nitriding, the following conclusions are drawn:

i) Based on one factor at a time (OFAT) experimentation, it is observed that the process variables such as standoff distance, power voltage, cooling time and feed rate have a significant effect on wall width and micro-hardness of aluminium alloy deposition layer by WAAM process.

ii) Increase in SOD results in the increase of oxidation and provides unevenness at the surface of the workpiece and also the chance of soot formation is increased on the surface of the deposited layer as higher distance provides greater exposure for the oxidation at the surface of workpiece which makes the surface quality poor. Upon experimentation, it is found that at 14 mm SOD, the track of deposition layer is better.

iii) Argon gas flow rate has a significant impact on shielding of the WAAM deposited Al part in order to avoid any unwanted contamination and oxidation. A very low argon gas flow rate enhances the chance of oxidation, however at high argon gas flow rate there is spatter deposition due to high pressure of the gas. Upon experimentation, it is found that at 18 l/min Argon gas flow rate the deposition is uniform and free from any oxidation.

iv) Increase in cooling time and feed rate provides uniformity of the deposited aluminium alloys with corresponding increase in wall width and micro hardness. Increase in voltage results in increase of micro-hardness and wall width of additively manufactured parts.

v) From the optimization analysis on the wall width, it is predicted that feed rate of 4 m/min, power voltage of 13 V, and cooling time of 25 sec provide minimum wall width. From the optimization analysis of the micro-hardness, it is predicted that feed rate of 6 m/min, power voltage of 13 V, and cooling time of 25 s provide maximum micro-hardness. The multiple objective optimizations result of the responses shows that feed rate of 4.5 m/min, power voltage of 13 V, cooling time of 25 s provide optimum results. The percentage of prediction error of the model for wall width is 2.805 % and that of micro-hardness is 3.737 % which is less than 5 %. Thus, developed mathematical modelling is suitable for WAAM of aluminium alloys.

vi) Microstructural analysis of the WAAM deposited sample shows that there is a transition of finer grains to courser grains from the bottom region to top region as the rate of heat dissipation is faster in the bottom region and the rate of heat dissipation is lower in the middle region as the middle region is sandwiched between the top and bottom layers. The WAAM deposited sample results into higher hardness than the substrate due to from rapid solidification, multiple thermal cycles and induced residual stresses, with the bottom region showing the highest hardness due to finer grains and better heat dissipation.

vii)The tensile properties of the Wire arc additively manufactured 5356 aluminium alloy varies across the section, with the bottom transverse section exhibiting higher ultimate tensile stress (UTS) and yield stress (YS) compared to the top and middle sections due to variations in heat dissipation conditions among layers. Longitudinal tensile samples demonstrate lower strength than transverse samples, potentially attributed to the presence of pores, cracks, and insufficient penetration between layers, impacting the tensile properties negatively. Compared to the as cast aluminium alloy, the average UTS and YS of the parts made by the WAAM are increased by 27.17% and 37.8%, respectively. Fractography of the tensile sample shows that the fracture mechanism is dimple fracture. In the fibrous zone equiaxed dimples are found but in slip zone the elongated dimples are found.

viii) Tribological studies on WAAM deposited sample reveals that with increase in load the COF decreases and with increase in load the fretting wear volume increases, however after a threshold limit of 6 N, fretting wear volume decreases due to formation of stable, hard, adherent oxide tribofilm which enhances the wear resistance. It is observed that during the initial stages of the test, the COF values are low, because of self-absorbed and inevitably polluted thin contaminant film that is present at the surface. The study of wear scar indicates that the wear mechanism is a combination of oxidative, adhesive and abrasive wear.

ix) The parametric investigation of the process variables on laser nitriding of WAAM deposited aluminium alloy reveals that the process variables such as N_2 gas flow rate, laser fluence, and overlapping percentage have a significant effect on the surface microhardness. Moreover, the mathematical model developed based on the Box Behnken design also provides useful results.

x) Increasing the N_2 gas flow rate and decreasing the laser fluence both lead to higher microhardness. While increasing the overlapping percentage it also boosts micro hardness, excessively high overlapping percentage can reduce it.

xi) From the optimization analysis of the micro-hardness it is predicted that N_2 gas flow rate of 24 l/min, laser fluence of 60 J/cm^2, and 85 % overlapping percentage provide maximum micro-hardness. Upon experimental validation of the optimization analysis, it is observed that the percentage of prediction error of micro-hardness is 3.94 % which is less than 5 %. Thus, above designed mathematical modelling is suitable for laser nitriding.

xii) After carrying out experiment at optimal process variables settings, it is observed that actual value of micro-hardness is obtained as 114.89

HV and the average micro-hardness obtained of the WAAM deposited sample is 73.2 HV. Hence after laser nitriding there is an increase of 56.95 % of micro-hardness.

xiii) It is observed that the laser nitriding increases the contact angle with distilled water from 72.230 to 107.860 for the left contact angle and from 67.330 to 114.640 for the right contact angle, making the surface hydrophobic from hydrophilic due to the formation of micro-textures and cavities and the formation of the AlN layer which acts as a barrier to water penetration. It is observed that with salt water solution also the contact angle increases for the laser nitrided surface.

xiv) It is observed that due to the formation of self-lubricating AlN, the COF of the laser nitride surface is reduced. A lower COF is favourable for marine applications due to lower wear, lower drag and it increases the efficiency of the marine components.

xv) It is observed that the wear volume of the laser nitrided surface also drastically reduces due to the formation of the hard aluminium nitride over the surface. It is also found that the laser nitrided surface has lower depth of wear in compared to the WAAM deposited sample.

The present research work on fabrication, mechanical and tribological analysis of parts of aluminium 5356 alloy by WAAM process is very much effective for industrial applications. The method of enhancement of hardness and tribological characteristics of additively manufactured parts by laser nitriding process has immense potential for marine applications.

5.2 Future scope of work

Based on the present study, further research can delve into broader aspects of laser nitriding combined with WAAM. The future scope of this work includes:

(i) **In-situ Monitoring and Data Analytics:** Implementing real-time monitoring of additive manufacturing process parameters and developing a closed-loop feedback system based on data analytics. This approach aims to achieve better deposition with enhanced geometric and mechanical properties.

(ii) **Simulation and Validation:** Conducting simulations of laser nitriding process parameters and validating the results with experimental data. This will help in understanding the process better and optimizing the parameters for improved outcomes.

(iii) **Hybrid WAAM Setup Development:** Creating a hybrid WAAM setup that integrates laser nitriding as a post-processing technique. This development aims to produce ready-to-use parts, thereby reducing cycle time and enhancing quality.

(iv) **Nano Indentation Test Analysis:** Performing nano indentation test analysis along the thickness of the nitride layer to examine the mechanical properties in detail across the layer's thickness. This will provide insights into the uniformity and effectiveness of the nitriding process.

References

[1] D. Godec *et al.*, “Introduction to Additive Manufacturing,” in *A Guide to Additive Manufacturing*, D. Godec, J. Gonzalez-Gutierrez, A. Nordin, E. Pei, and J. Ureña Alcázar, Eds., Cham: Springer International Publishing, 2022, pp. 1–44. doi: 10.1007/978-3-031-05863-9_1.

[2] A. Al Rashid, S. A. Khan, S. G. Al-Ghamdi, and M. Koç, “Additive manufacturing: Technology, applications, markets, and opportunities for the built environment,” *Autom. Constr.*, vol. 118, p. 103268, Oct. 2020, doi: 10.1016/j.autcon.2020.103268.

[3] “Classification of additive manufacturing processes from different contexts. Download Scientific Diagram.” Accessed: May 17, 2024. [Online]. Available: https://www.researchgate.net/figure/Classification-of-additive-manufacturing-processes-from-different-contexts_fig1_349868862

[4] “Figure 3. Classification of additive manufacturing processes from...,” ResearchGate. Accessed: May 17, 2024. [Online]. Available: https://www.researchgate.net/figure/Classification-of-additive-manufacturing-processes-from-different-contexts_fig1_349868862

[5] J. P. M. Pragana, R. F. V. Sampaio, I. M. F. Bragança, C. M. A. Silva, and P. A. F. Martins, “Hybrid metal additive manufacturing: A state–of–the-art review,” *Adv. Ind. Manuf. Eng.*, vol. 2, p. 100032, May 2021, doi: 10.1016/j.aime.2021.100032.

[6] “Types of WAAM processes. (a) GTAW; (b) PAW; (c) GMAW. | Download Scientific Diagram.” Accessed: May 17, 2024. [Online]. Available: https://www.researchgate.net/figure/Types-of-WAAM-processes-a-GTAW-b-PAW-c-GMAW_fig3_370786517

[7] S. Nesli and O. Yilmaz, “Surface characteristics of laser polished Ti-6Al-4V parts produced by electron beam melting additive manufacturing process,” *Int. J. Adv. Manuf. Technol.*, vol. 114, May 2021, doi: 10.1007/s00170-021-06861-6.

[8] J. dos Santos Solheid, H. Jürgen Seifert, and W. Pfleging, “Laser surface modification and polishing of additive manufactured metallic parts,” *Procedia CIRP*, vol. 74, pp. 280–284, Jan. 2018, doi: 10.1016/j.procir.2018.08.111.

[9] R. T. Mushtaq, Y. Wang, A. M. Khan, M. Rehman, X. Li, and S. Sharma, “A post-processing laser polishing method to improve process performance of 3D printed new Industrial Nylon-6 polymer,” *J. Manuf. Process.*, vol. 101, pp. 546–560, Sep. 2023, doi: 10.1016/j.jmapro.2023.06.019.

[10] S. R *et al.*, “Laser Shock Peening and its Applications: A Review,” *Lasers Manuf. Mater. Process.*, vol. 6, no. 4, pp. 424–463, Dec. 2019, doi: 10.1007/s40516-019-00098-8.

[11] X. Luo, N. Dang, and X. Wang, “The effect of laser shock peening, shot peening and their combination on the microstructure and fatigue properties of Ti-6Al-4V titanium alloy,” *Int. J. Fatigue*, vol. 153, p. 106465, Dec. 2021, doi: 10.1016/j.ijfatigue.2021.106465.

[12] M. Munther, T. Martin, A. Tajyar, L. Hackel, A. Beheshti, and K. Davami, “Laser shock peening and its effects on microstructure and properties of additively manufactured metal alloys: a review,” *Eng. Res. Express*, vol. 2, no. 2, p. 022001, Jun. 2020, doi: 10.1088/2631-8695/ab9b16.

[13] “Nitriding - an overview | ScienceDirect Topics.” Accessed: May 17, 2024. [Online]. Available: https://www.sciencedirect.com/topics/materials-science/nitriding

[14] W. T. Zheng and C. Q. Sun, “Electronic process of nitriding: Mechanism and applications,” *Prog. Solid State Chem.*, vol. 34, no. 1, pp. 1–20, Jun. 2006, doi: 10.1016/j.progsolidstchem.2005.12.001.

[15] “The Al−N (Aluminium-Nitrogen) system | Journal of Phase Equilibria.” Accessed: May 17, 2024. [Online]. Available: https://link.springer.com/article/10.1007/BF02873001

[16] “Salt Baths - an overview | ScienceDirect Topics.” Accessed: May 17, 2024. [Online]. Available: https://www.sciencedirect.com/topics/engineering/salt-baths

[17] “Plasma Nitriding - an overview | ScienceDirect Topics.” Accessed: May 17, 2024. [Online]. Available: https://www.sciencedirect.com/topics/engineering/plasma-nitriding

[18] “Laser Nitriding - an overview | ScienceDirect Topics.” Accessed: May 17, 2024. [Online]. Available: https://www.sciencedirect.com/topics/engineering/laser-nitriding

[19] K. E. K. Vimal, M. Naveen Srinivas, and S. Rajak, “Wire arc additive manufacturing of aluminium alloys: A review,” *Mater. Today Proc.*, vol. 41, pp. 1139–1145, Jan. 2021, doi: 10.1016/j.matpr.2020.09.153.

[20] B. Wu *et al.*, “A review of the wire arc additive manufacturing of metals: properties, defects and quality improvement,” *J. Manuf. Process.*, vol. 35, pp. 127–139, Oct. 2018, doi: 10.1016/j.jmapro.2018.08.001.

[21] J. Müller and J. Hensel, “WAAM of structural components—building strategies for varying wall thicknesses,” *Weld. World*, vol. 67, no. 4, pp. 833–844, Apr. 2023, doi: 10.1007/s40194-023-01481-y.

[22] C. R. Cunningham, J. M. Flynn, A. Shokrani, V. Dhokia, and S. T. Newman, “Invited review article: Strategies and processes for high quality wire arc additive manufacturing,” *Addit. Manuf.*, vol. 22, pp. 672–686, Aug. 2018, doi: 10.1016/j.addma.2018.06.020.

[23] P. Shukla, B. Dash, D. Kiran, and S. Bukkapatnam, “Arc Behavior in Wire Arc Additive Manufacturing Process,” *Procedia Manuf.*, vol. 48, pp. 725–729, Jan. 2020, doi: 10.1016/j.promfg.2020.05.105.

[24] A. Horgar, H. Fostervoll, B. Nyhus, X. Ren, M. Eriksson, and O. M. Akselsen, “Additive manufacturing using WAAM with AA5183

wire," *J. Mater. Process. Technol.*, vol. 259, pp. 68–74, Sep. 2018, doi: 10.1016/j.jmatprotec.2018.04.014.

[25] G. Langelandsvik, O. M. Akselsen, T. Furu, and H. J. Roven, "Review of Aluminium Alloy Development for Wire Arc Additive Manufacturing," *Materials*, vol. 14, no. 18, Art. no. 18, Jan. 2021, doi: 10.3390/ma14185370.

[26] J. Gu, S. Yang, M. Gao, J. Bai, Y. Zhai, and J. Ding, "Micropore evolution in additively manufactured aluminium alloys under heat treatment and inter-layer rolling," *Mater. Des.*, vol. 186, p. 108288, Jan. 2020, doi: 10.1016/j.matdes.2019.108288.

[27] M. Liberini *et al.*, "Selection of Optimal Process Parameters for Wire Arc Additive Manufacturing," *Procedia CIRP*, vol. 62, pp. 470–474, Jan. 2017, doi: 10.1016/j.procir.2016.06.124.

[28] K. El-Aziz *et al.*, "Development of Al-Mg-Si alloy performance by addition of grain refiner Al-5Ti-1B alloy," *Sci. Prog.*, vol. 104, p. 368504211029469, Jun. 2021, doi: 10.1177/00368504211029469.

[29] J. Ouyang, H. Wang, and R. Kovacevic, "Rapid prototyping of 5356-aluminium alloy based on variable polarity gas tungsten arc welding: Process control and microstructure," *Mater. Manuf. Process. - MATER MANUF PROCESS*, vol. 17, pp. 103–124, May 2002, doi: 10.1081/AMP-120002801.

[30] H. Geng, J. Li, J. Xiong, X. Lin, and F. Zhang, "Geometric Limitation and Tensile Properties of Wire and Arc Additive Manufacturing 5A06 Aluminium Alloy Parts," *J. Mater. Eng. Perform.*, vol. 26, pp. 1–9, Oct. 2016, doi: 10.1007/s11665-016-2480-y.

[31] K. Derekar, J. Lawrence, G. Melton, A. Addison, X. Zhang, and L. Xu, "Influence of Interpass Temperature on Wire Arc Additive Manufacturing (WAAM) of Aluminium Alloy Components," *MATEC Web Conf.*, vol. 269, p. 05001, 2019, doi: 10.1051/matecconf/201926905001.

[32] M. Tawfik, M. Nemat-Alla, and M. Dewidar, “Effect of Travel Speed on the Properties of Al-Mg Aluminium Alloy Fabricated by Wire Arc Additive Manufacturing,” *J. Mater. Eng. Perform.*, vol. 30, Jun. 2021, doi: 10.1007/s11665-021-05959-y.

[33] “Fretting Wear - an overview | ScienceDirect Topics.” Accessed: May 17, 2024. [Online]. Available: https://www.sciencedirect.com/topics/engineering/fretting-wear

[34] S. M. O’Halloran, A. D. Connaire, A. M. Harte, and S. B. Leen, “Modelling of fretting in the pressure armour layer of flexible marine risers,” *Tribol. Int.*, vol. 100, pp. 306–316, Aug. 2016, doi: 10.1016/j.triboint.2016.02.040.

[35] M. P. Szolwinski and T. N. Farris, “Observation, analysis and prediction of fretting fatigue in 2024-T351 aluminium alloy,” *Wear*, vol. 221, no. 1, pp. 24–36, Oct. 1998, doi: 10.1016/S0043-1648(98)00264-6.

[36] “(PDF) Model for fracture mechanics based prediction of the fatigue strength of engineering alloys containing microscopical initial defects.” Accessed: May 17, 2024. [Online]. Available: https://www.researchgate.net/publication/275170878_Model_for_fracture_mechanics_based_prediction_of_the_fatigue_strength_of_engineering_alloys_containing_microscopical_initial_defects

[37] A. Kulkarni *et al.*, “Influence of laser-nitriding on mechanical and elevated temperature fretting wear behavior of A356-alloy,” *Surf. Coat. Technol.*, vol. 413, p. 127072, Mar. 2021, doi: 10.1016/j.surfcoat.2021.127072.

[38] E. Sicard, C. Boulmer-Leborgne, C. Andreazza-Vignolle, and M. Frainais, “Excimer laser surface treatment of aluminium alloy in nitrogen,” *Appl. Phys. Mater. Sci. Process.*, vol. 73, pp. 55–60, Jul. 2001, doi: 10.1007/s003390100742.

[39] C. Zeng *et al.*, “Laser nitriding of titanium surfaces for biomedical applications,” *Surf. Coat. Technol.*, vol. 385, p. 125397, Mar. 2020, doi: 10.1016/j.surfcoat.2020.125397.

[40] R. Singh, A. Kurella, and N. B. Dahotre, “Laser surface modification of Ti--6Al--4V: wear and corrosion characterization in simulated biofluid,” *J. Biomater. Appl.*, vol. 21, no. 1, pp. 49–73, Jul. 2006, doi: 10.1177/0885328206055998.

[41] P. Schaaf, “Laser nitriding of metals,” *Prog. Mater. Sci.*, vol. 47, no. 1, pp. 1–161, Jan. 2002, doi: 10.1016/S0079-6425(00)00003-7.

[42] “JMMP | Free Full-Text | Work Envelope Expansion and Parametric Optimization in WAAM with Relative Density and Surface Aspect as Quality Constraints: The Case of Al5Mg Thin Walls with Active Cooling.” Accessed: May 18, 2024. [Online]. Available: https://www.mdpi.com/2504-4494/5/2/40

[43] V. Jorge, F. Matos Scotti, A. Scotti, and F. Teixeira, “The significance of supplementary shielding in WAAM of aluminium thin walls,” *J. Manuf. Process.*, vol. 106, Oct. 2023, doi: 10.1016/j.jmapro.2023.09.063.

[44] “A shape control strategy for wire arc additive manufacturing of thin-walled aluminium structures with sharp corners - ScienceDirect.” Accessed: May 18, 2024. [Online]. Available: https://www.sciencedirect.com/science/article/pii/S1526612521000487

[45] S. Gudur, V. Nagallapati, S. Pawar, G. Muvvala, and S. Simhambhatla, “A study on the effect of substrate heating and cooling on bead geometry in wire arc additive manufacturing and its correlation with cooling rate,” *Mater. Today Proc.*, vol. 41, pp. 431–436, Jan. 2021, doi: 10.1016/j.matpr.2020.10.071.

[46] M. S. Mohd Mansor *et al.*, “Integrated approach to Wire Arc Additive Manufacturing (WAAM) optimization: Harnessing the synergy of process parameters and deposition strategies,” *J. Mater. Res. Technol.*, vol. 30, pp. 2478–2499, May 2024, doi: 10.1016/j.jmrt.2024.03.170.

[47] H. R. Ghazvinloo and A. Honarbakhsh-Raouf, “Numerical Modeling of Heat-Affected Zone in GMAW Process,” *Mater. Sci.*, vol. 56, pp. 807–813, Nov. 2021, doi: 10.1007/s11003-021-00498-2.

[48] T. Hauser *et al.*, “Oxidation in wire arc additive manufacturing of aluminium alloys,” *Addit. Manuf.*, vol. 41, p. 101958, May 2021, doi: 10.1016/j.addma.2021.101958.

[49] T. Klein, A. Arnoldt, R. Lahnsteiner, and M. Schnall, “Microstructure and mechanical properties of a structurally refined Al–Mg–Si alloy for wire-arc additive manufacturing,” *Mater. Sci. Eng. A*, vol. 830, p. 142318, Jan. 2022, doi: 10.1016/j.msea.2021.142318.

[50] Z. Yu, T. Yuan, M. Xu, H. Zhang, X. Jiang, and S. Chen, “Microstructure and mechanical properties of Al-Zn-Mg-Cu alloy fabricated by wire + arc additive manufacturing,” *J. Manuf. Process.*, vol. 62, pp. 430–439, Feb. 2021, doi: 10.1016/j.jmapro.2020.12.045.

[51] S. Eschelbacher and H.-C. Möhring, “Hardness and Orthogonal Cutting Analyses of a Wire and Arc Additive Manufactured (WAAM) Sample,” *Procedia CIRP*, vol. 101, pp. 26–29, Jan. 2021, doi: 10.1016/j.procir.2021.02.005.

[52] R. Warsi, K. H. Kazmi, and M. Chandra, “Mechanical properties of wire and arc additive manufactured component deposited by a CNC controlled GMAW,” *Mater. Today Proc.*, vol. 56, pp. 2818–2825, Jan. 2022, doi: 10.1016/j.matpr.2021.10.114.

[53] B. Weber, X. Meng, R. Zhang, M. Nitawaki, T. Sagawa, and L. Gardner, “Tensile behaviour of WAAM high strength steel material and members,” *Mater. Des.*, vol. 237, p. 112517, Jan. 2024, doi: 10.1016/j.matdes.2023.112517.

[54] T. Gao, H. Liu, F. Wang, and Y. Chen, “Effect of Ce on the microstructure and mechanical properties of 5356 aluminium alloy,” vol. 24, pp. 34–39, Jun. 2016, doi: 10.11951/j.issn.1005-0299.20160306.

[55] T. Kobayashi, “Strength and fracture of aluminium alloys,” *Mater. Sci. Eng. A*, vol. 280, no. 1, pp. 8–16, Mar. 2000, doi: 10.1016/S0921-5093(99)00649-8.

[56] “Materials | Free Full-Text | Morphological Characteristics of Dimples of Ductile Fracture of VT23M Titanium Alloy and Identification of Dimples on Fractograms of Different Scale.” Accessed: May 18, 2024. [Online]. Available: https://www.mdpi.com/1996-1944/12/13/2051

[57] H. Khanmohammadi, W. Wijanarko, and N. Espallargas, “The role of tribofilm chemical composition on wear of austenitic stainless steel lubricated with water-glycol containing ionic-liquids as additives,” *Wear*, vol. 520–521, p. 204672, May 2023, doi: 10.1016/j.wear.2023.204672.

[58] “Mindlin, R.D. (1949) Compliance of Elastic Bodies in Contact. Transactions of the ASME, Journal of Applied Mechanics, 16, 259-268. - References - Scientific Research Publishing.” Accessed: May 18, 2024. [Online]. Available: https://www.scirp.org/reference/referencespapers?referenceid=2916904

[59] M. C. Gaspar and A. Ramalho, “Fretting behaviour of galvanised steel,” *Wear*, vol. 252, no. 3, pp. 199–209, Feb. 2002, doi: 10.1016/S0043-1648(01)00874-2.

[60] R. Nanjundaiah *et al.*, “Fretting Wear Behavior on LPBF Processed AlSi10Mg Alloy for different Heat Treatment Conditions,” *J. Mater. Res. Technol.*, vol. 30, Apr. 2024, doi: 10.1016/j.jmrt.2024.04.147.

[61] C.-W. Chan, L. Seunghwan, G. Smith, and C. Donaghy, “Fibre laser nitriding of titanium and its alloy in open atmosphere for orthopaedic implant applications: Investigations on surface quality, microstructure and tribological properties,” *Surf. Coat. Technol.*, vol. 309, pp. 628–640, Jan. 2017, doi: 10.1016/j.surfcoat.2016.12.036.

[62] R. Baumann, S. Heilmann, D. Köberlin, U. Füssel, and A. Fabián Lasagni, “Influencing the contact angle during brazing by direct laser interference structured textures on the substrate surface,” *Mater. Lett. X*, vol. 13, p. 100129, Mar. 2022, doi: 10.1016/j.mlblux.2022.100129.

[63] “Table 3 Elemental analysis of laser nitrided Ti-13Nb-13Zr alloy at high...,” ResearchGate. Accessed: May 19, 2024. [Online]. Available: https://www.researchgate.net/figure/Elemental-analysis-of-laser-nitrided-Ti-13Nb-13Zr-alloy-at-high-scanning-speed_tbl2_223650722